Fabrication of Electroluminescent Silicon Diodes by Plasma Ion Implantation

A Thesis Submitted to the
College of Graduate Studies and Research
in Partial Fulfillment of the Requirements
for the degree of Master of Science
in the Department of Physics and Engineering Physics
University of Saskatchewan
Saskatoon

By
Phillip Desautels

Permission to Use

In presenting this thesis in partial fulfilment of the requirements for a Postgraduate degree from the University of Saskatchewan, I agree that the Libraries of this University may make it freely available for inspection. I further agree that permission for copying of this thesis in any manner, in whole or in part, for scholarly purposes may be granted by the professor or professors who supervised my thesis work or, in their absence, by the Head of the Department or the Dean of the College in which my thesis work was done. It is understood that any copying or publication or use of this thesis or parts thereof for financial gain shall not be allowed without my written permission. It is also understood that due recognition shall be given to me and to the University of Saskatchewan in any scholarly use which may be made of any material in my thesis.

Requests for permission to copy or to make other use of material in this thesis in whole or part should be addressed to:

Head of the Department of Physics and Engineering Physics
116 Science Place
University of Saskatchewan
Saskatoon, Saskatchewan
Canada
S7N 5E2

Abstract

This thesis describes the fabrication and testing of electroluminescent diodes made from silicon subjected to plasma ion implantation. A silicon-compatible, electrically driven light source is desired to increase the speed and efficiency of short-range data transfer in the communications and computing industries. As it is an indirect band gap material, ordinary silicon is too inefficient a light source to be useful for these applications. Past experiments have demonstrated that modifying the structural properties of the crystal can enhance its luminescence properties, and that light ion implantation is capable of achieving this effect. This research investigates the relationship between the ion implantation processing parameters, the post-implantation annealing temperature, and the observable electroluminescence from the resulting silicon diodes.

Prior to the creation of electroluminescent devices, much work was done to improve the efficiency and reliability of the fabrication procedure. A numerical algorithm was devised to analyze Langmuir probe data in order to improve estimates of implanted ion fluence. A new sweeping power supply to drive current to the probe was designed, built, and tested. A custom software package was developed to improve the speed and reliability of plasma ion implantation experiments, and another piece of software was made to facilitate the viewing and analysis of spectra measured from the finished silicon LEDs.

Several dozen silicon diodes were produced from wafers implanted with hydrogen, helium, and deuterium, using a variety of implanted ion doses and post-implantation annealing conditions. One additional device was fabricated out of unimplanted, unannealed silicon. Most devices, including the unimplanted device, were electroluminescent at visible wavelengths to some degree. The intensity and spectrum of light emission from each device were measured. The results suggest that the observed luminescence originated from the native oxide layer on the surface of the ion-implanted silicon, but that the intensity of luminescence could be enhanced with a carefully chosen ion implantation and annealing procedure.

Acknowledgements

I would like to extend my gratitude to my supervisor, Dr. Michael P. Bradley, for his steadfast support and encouragement throughout the course of this project. I also wish to thank Dr. Chary Rangacharyulu for useful discussions and comments.

All ion implantation in this work was carried out using a customized Plasmionique ICP600 plasma system, with the high-voltage pulse generator originally designed by J. T. Steenkamp and later refined and maintained by myself and fellow M. Sc. students Darren Hunter and John McLeod. The system was funded by a CFI New Opportunities Fund Grant held by Dr. Michael P. Bradley, titled "Plasma Ion Implantation experiment for new photonic materials." I am also thankful to Dr. Akira Hirose for providing the plasma chamber that originally allowed our lab to pursue this line of research, and to Dr. Chijin Xiao for generously loaning us a spectrometer for use in this research. Thanks also go to former M. Sc. students J. T. Steenkamp and Marcel Risch for their development of sheath modelling and fluence prediction software that improved the quality of this work substantially.

I am indebted to Perry Balon, Ted Toporowski, and Blair Chomyshen at the Physics Machine Shop for their help in machining various pieces of hardware for my project, and to David McColl for general technical support and for a generous policy regarding the use of his tools. I am grateful to Dr. Stephen Urquhart from the Dept. of Chemistry for volunteering the use of his evaporator for this research, and also to Mitra Masnadi Khiabani for her assistance with that equipment.

Financial support for this research was provided by the NSERC Postgraduate Scholarship program and NSERC Discovery Grant 298455-08 ("New methods and ideas in silicon-compatible photonics") and supplemented by the Dept. of Physics and Engineering Physics at the University of Saskatchewan.

Contents

List of Tables

List of Figures

List of Abbreviations

VLSI	Very Large Scale Integration
CMOS	Complementary Metal-Oxide-Semiconductor
VCSEL	Vertical Cavity Surface-Emitting Laser
PII	Plasma Ion Implantation
ICP	Inductively Coupled Plasma
EL	Electroluminescence, or Electroluminescent
PL	Photoluminescence, or Photoluminescent
LED	Light-Emitting Diode
SRH	Shockley-Read-Hall
QCLC	Quantum Confinement Luminescence Centre
TEM	Transmission Electron Microscopy
AFM	Atomic Force Microscopy

List of Symbols (Chapter 2)

Symbol	Meaning	Units	Notes
$\vec{k}$	Crystal momentum vector	m^{-1}	
$E(\vec{k})$	Electron state energy	eV	
τ	Recombination lifetime	s	
τ_{SRH}	Shockley-Read-Hall lifetime		
τ_{rad}	Radiative lifetime		
τ_{Auger}	Auger lifetime		
n or p	Electron/hole concentration	cm^{-3}	
n_i or p_i	Intrinsic concentration		Constant: 1×10^{10} cm^{-3}
n_0 or p_0	Equilibrium concentration		$n_0 p_0 = n_i^2$
Δn	Excess carrier concentration		$\Delta n = \Delta p$ for elec. inject.
R	Bulk recombination rate	$\mathrm{cm}^{-3}\mathrm{s}^{-1}$	$R = \Delta n/\tau$
η	Quantum efficiency	none	
η_i	Internal quantum efficiency		
η_x	External quantum efficiency		$\eta_x < \eta_i$

List of Symbols (Chapter 3)

Symbol	Meaning	Units	Notes
m	Particle mass	kg	
m_i	Ion mass		Average over ion species
m_e	Electron mass		9.11×10^{-31} kg
v	Particle velocity	m/s	
v_i	Ion velocity		
v_e	Electron velocity		
n	Particle density	cm^{-3}	
n_i	Ion density		
n_e	Electron density		
n_0	Bulk plasma density		$n_{i,0} = n_{e,0} = n_0$
n_n	Neutral gas density		
λ_{De}	Plasma Debye length	metres	
T_e	Electron temperature	eV	Boltzmann const. included
I	Electric current	amperes	
I_i	Ion current		
I_e	Electron current		
V	Electric potential	volts	
V_p	Plasma potential		Measured *in situ*
V_s	Sheath edge potential		Analytically determined
V_0	Conductor potential		Chosen by experimenter
r	Co-ord. norm. to conductor	metres	
r_s	Sheath boundary position		
r_0	Conductor surface position		
A	Collecting surface area	m^2	
A_p	Probe surface area		
A_s	Sheath surface area		$A_s > A_p$

Chapter 1

Introduction

As the computational speed of microprocessors increases, more attention has been paid to signal propagation delay in the metal wires linking chips and components together. Although the speed of an electrical signal on a metal wire is, in principle, the speed of light (3×10^8 m/s), in reality it is limited by the electrical characteristics of the wires themselves: the inductance (L) and capacitance (C) per unit length of wire impose delays on signal propagation related to the finite time required to store energy in the wire's magnetic and electric fields, respectively. As processors are made faster and their components are made smaller and more closely packed, signal propagation in the connecting wires tends to be made slower, to the point where the delay between transmission and reception of information can exceed the time available for the processor to complete a single cycle. Connections between chips and between distant components on the same chip are the most problematic, since the lengths of these connections do not scale down as component density is increased. Consequently, there is a communications bottleneck in modern computing: while bit transfer rates between closely spaced on-chip components may become arbitrarily fast because of the short distances involved, the intermediate connections between components within a single computer slow the flow of data substantially [1, 2].

The most promising solution to this dilemma is to replace the troublesome metal wires with optical waveguides or fibres, as has already been done for long-distance communication with fibre-optic cable. Since the speed of an optical signals depends only on the refractive index of the material used to make it, rather than on process-dependent electrical characteristics, optical connections may provide a solution to the problem of increasing propagation delay in Very Large-Scale Integration (VLSI) sili-

con chips. Optical transmission is also free from cross-talk and other electromagnetic interference that can degrade the performance of electrical systems. Furthermore, optical pathways lack the Ohmic (I^2R) power loss that is present in wired connections; since power dissipation density has lately become a leading-order engineering issue in VLSI design, this is yet another advantage to using optical transmission.

Many of the components required for integrated silicon optoelectronics, such as silicon-based or silicon-compatible waveguides [3], modulators [4], and photodetectors [5, 6], have already been developed for use with integrated optoelectronics. However, because silicon is an inefficient light emitter, most optical interconnection schemes currently under development rely on existing VCSEL (vertical cavity surface-emitting laser) units that are made of III-V semiconductors such as GaAs, due to their superior light emission efficiency. Because these materials are not compatible with the crystal structure of silicon, the VCSEL units must be made separately and bonded to the chip's substrate at great expense [7]. For practical as well as economic reasons, a more elegant and cost-effective way of making chip- or board-level optical connections is desired.

The ideal solution to the problem would be to create electroluminescent (EL) silicon that could be integrated seamlessly into existing CMOS (complementary metal-oxide-semiconductor) technology. Unfortunately, the electronic structure of crystalline silicon makes it a very weak light emitter compared to GaAs and other III-V semiconductors. Despite this obstacle, the potential utility of luminescent silicon devices has driven considerable effort toward inducing useful EL from silicon-based materials. To date, appreciable EL at various wavelengths has been reported from chemically etched porous silicon [8], silicon nanoparticles embedded in a silicon dioxide matrix [9], erbium-doped silicon [10], and ion-implanted silicon [11]. These processes improve EL efficiency in silicon by modifying its electronic properties directly (as in porous Si and nanocrystals) or by introducing more efficient radiative mechanisms into a silicon matrix (as in Er doping). The purpose of the present work is to investigate the applicability of plasma ion implantation (PII) to the production of useful electroluminescent silicon devices, with a focus on EL mechanisms that do

not involve bonding or doping the silicon with rare elements.

Plasma ion implantation is an extremely useful tool in many materials processing applications, as it allows large quantities of material to be processed over short times and at low cost. Past work has already demonstrated that silicon implanted with high doses of hydrogen can become electroluminescent under certain processing conditions [12, 13], and preliminary work in our own laboratory has confirmed this [14, 15]. However, there are several parameters that may contribute to the emergence of the observed EL: implant energy, implanted dose, ion mass and chemical properties, post-implant annealing conditions, the forming of oxides on or within the silicon, and the types of metal contacts used to form the EL devices themselves. Consequently, there are several theories regarding the origin of EL in plasma-implanted silicon, and no consensus has yet been reached.

The remainder of this document will discuss the preparation, execution, and results of an attempt to create electroluminescent silicon using ion implantation with hydrogen, helium, and deuterium. Chapter 2 will explain the mechanism behind luminescence in most semiconductors, explain why ordinary silicon is a poor light emitter, and describe some of the light emission mechanisms that have been proposed to explain enhanced EL in silicon devices. Chapter 3 will provide an overview of plasma ion implantation and its role in the present research. Chapter 4 will describe the equipment and procedure used to prepare and characterize the implanted silicon devices. Chapter 5 will discuss and analyze the results of the experiment, and finally Chapter 6 will present the conclusions drawn from this work and some ideas for future experiments in this field.

Chapter 2

Condensed Matter Physics

In order to effectively study electroluminescence in silicon, it is important to understand the reason why an ordinary silicon crystal is an inefficient light emitter. The answer is found in the electronic band structure of the silicon crystal, shown in Figure 2.1.

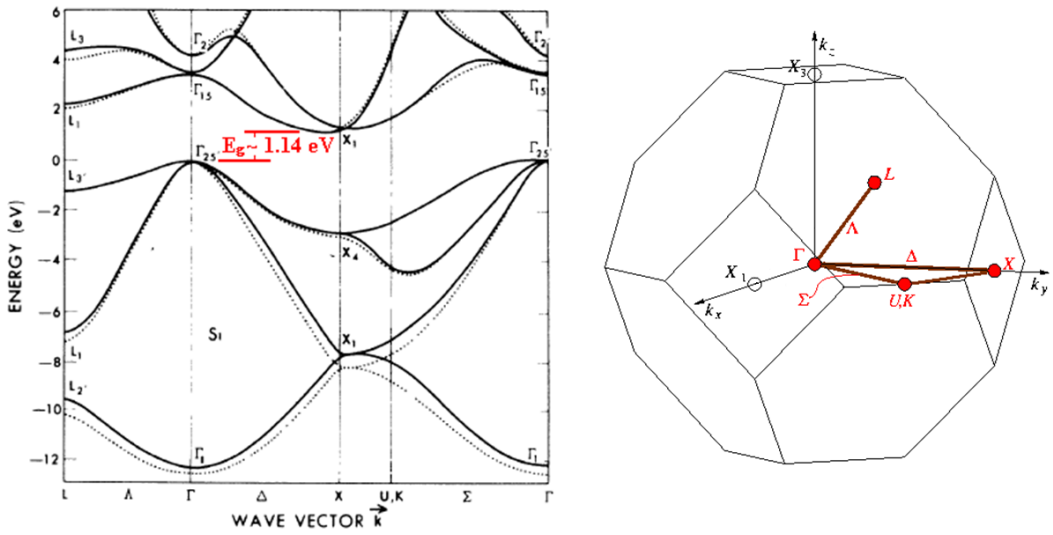

Figure 2.1: The band structure of crystalline silicon, from Chelikowsky and Cohen [16]. Labels on the horizontal axis represent points and paths within the reciprocal lattice of the Silicon-I crystal (diamond structure), which is shown to the right [17]. The Fermi energy is at 0 eV on the vertical axis.

The band structure represents the dispersion relation $E(\vec{k})$ of several electron orbitals inside the crystal lattice, where E is the energy and $\vec{k}$ is the crystal momentum of the electron, respectively. These and other symbols used in this chapter are defined in the List of Symbols on page x. It can be computed (as in Figure 2.1) by

modeling the interaction between wavelike electrons and a potential energy function that depends on the composition and structure of the crystal. The electron wavefunctions used in such a calculation are typically Bloch waves: free electron waves modulated by periodic functions $u_k(\vec{r})$ such that the full electron wavefunctions $\psi_k(\vec{r})$ are

$$\psi_k(\vec{r}) = u_k(\vec{r}) \exp\left(i\vec{k} \cdot \vec{r}\right), \tag{2.1}$$

where $u_k(\vec{r})$ is periodic over the same length interval L as the crystal lattice. Given the complexity of the many-body problem - a periodic arrangement of ion cores and their electron shells - the true potential within the crystal cannot be determined *a priori*. Instead, the ion core potential, including the core electrons (which do not contribute much to the electronic properties of the crystal) are replaced with an artificial pseudopotential to allow for converging solutions [16].

2.1 Luminescence and Carrier Lifetimes

From the information presented in Figure 2.1, it is clear that pure silicon is an insulator: the Fermi energy (the maximum energy an electron may have at absolute zero) lies within a region without any allowed electronic states, called a *band gap*, which makes it impossible to drive electric current through the crystal without applying a very strong electric field and risking damage to the device. However, the band gap also allows for luminescence if energy can be applied to the electrons in the crystal's valence (low energy) band. When electrons are promoted to the conduction (high energy) band, leaving behind empty states (holes) in the valence band, there are three principal ways by which the charge carriers may recombine into their original states: radiative (band-to-band) transitions, which result in photon emission; nonradiative Shockley-Read-Hall (SRH) recombination at impurity or defect centres, which is coupled to lattice vibrations (phonons); and another nonradiative process called Auger recombination. These processes are shown schematically in Figure 2.2. The relative rates at which the three processes occur determine the efficiency of luminescence in

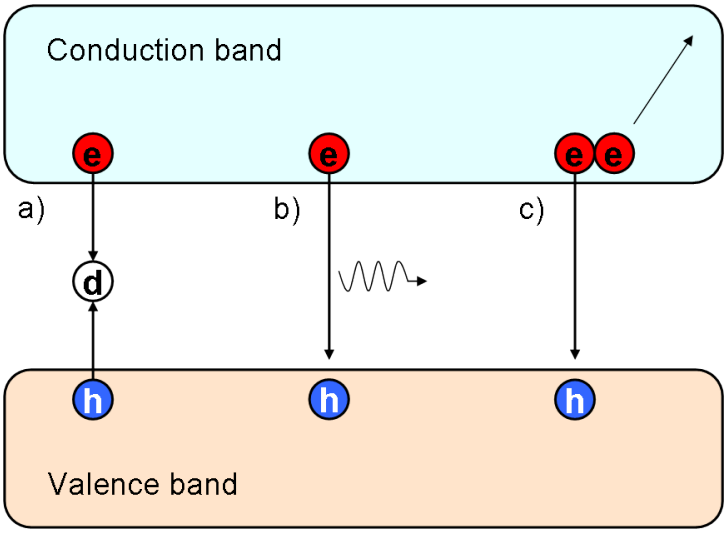

Figure 2.2: Schematic representation of the three main recombination paths for electron-hole pairs in a silicon crystal. In Shockley-Read-Hall recombination (a), electrons and holes are trapped by defects "d" and recombine nonradiatively. Radiative (direct, band-to-band) recombination (b) is the direct transition of a conduction electron into a hole in the valence band, which generates a photon to carry away the released energy. Auger recombination (c) occurs when the energy and momentum difference between electron and hole states is transferred to another charge carrier instead; the process shown is e-e-h Auger recombination, but e-h-h recombination is also possible.

the material. Each process is characterized by a mean lifetime τ, which represents the average time required for an electron-hole pair to recombine via that process. The following is a brief overview of these recombination processes.

2.1.1 Shockley-Read-Hall Recombination

Shockley-Read-Hall (SRH) recombination occurs when conduction band electrons recombine with holes via impurities or defects (called *recombination centres*, or *traps*) with energy states deep within the band gap. The energy liberated by this process is transferred through the impurity or defect to multiple phonons. No photons are created. SRH recombination is dominant when the defect or impurity concentration is comparable to the carrier concentration in the material.

Because this recombination channel operates by trapping carriers in a defect

state, it does not require that both carriers (electron and hole) be at the same place at the same time; the defect may trap one carrier for a time, then attract the opposite carrier at some later time. For this reason, the SRH recombination lifetime does not strongly depend on the carrier concentration [18]:

$$\tau_{SRH} = \frac{\tau_p \left(n_0 + n_1 + \Delta n\right) + \tau_n \left(p_0 + p_1 + \Delta n\right)}{p_0 + n_0 + \Delta n}, \tag{2.2}$$

where n_0 and p_0 represent the equilibrium carrier concentrations, and Δn is the excess carrier concentration being injected into the semiconductor. In the case of an electrically driven semiconductor device, Δn must equal Δp to maintain overall charge neutrality, so the remainder of this discussion will refer only to Δn. The coefficients τ_n and τ_p represent the trapping lifetimes of electrons and holes (respectively) by the defect or impurity centres, and n_1 and p_1 are corrections to the carrier concentrations defined as:

$$n_1 = n_i \exp\left(\frac{E_T - E_f}{T}\right), \quad p_1 = p_i \exp\left(-\frac{E_T - E_f}{T}\right). \tag{2.3}$$

The energy E_T is the effective energy state of the defect or impurity site and must lie within the band gap, and the term E_f is the Fermi energy in the semiconductor.

2.1.2 Radiative Recombination

A radiative transition occurs when an electron in the conduction band makes a direct transition into a hole state in the valence band, releasing the energy difference between the two states by producing a photon. Such transitions are the means by which direct band-gap semiconductors such as GaAs produce light. However, the band gap in silicon is *indirect*: the maximum energy in the valence band occurs at a different value of the wavevector $\vec{k}$ than the minimum in the conduction band. Even though electrons in the crystal are not truly free particles, the quantity $\hbar\,\vec{k}$, called the crystal momentum, must still be conserved in all transitions [19]. Therefore, the transition between bands requires interaction with phonons to account for the difference in crystal momentum, which strongly reduces the rate at which these transitions occur.

Unlike the SRH process, radiative recombination does require the simultaneous presence of two carriers in the same location [20]. Therefore, the radiative recombination lifetime depends on the carrier density as

$$\tau_{rad} = \frac{1}{B\left(n_0 + p_0 + \Delta n\right)}. \tag{2.4}$$

As the coefficient B must reflect the likelihood of radiative recombination, one expects its value in silicon should be lower than its value in a direct-bandgap semiconductor like GaAs. In bulk silicon at 300 K, the coefficient B is 9.5×10^{-15} $\mathrm{cm^3 s^{-1}}$ [21], whereas the value of B in GaAs has been measured to be between 1 and $5 \times 10^{-}10$ $\mathrm{cm^3 s^{-1}}$, depending on the composition of the compound and the conditions of the experiment [22, 23].

2.1.3 Auger Recombination

Auger recombination occurs when an electron-hole pair donates energy and crystal momentum to a third charge carrier; this process can involve either two electrons and one hole or two holes and one electron, with the former process being more common. No photon is generated. The energized carrier releases its extra energy to multiple phonons over time, a process called thermalization. Because the Auger process requires the participation of three carriers at once, the Auger lifetime is related to carrier density as

$$\tau_{Auger} = \frac{1}{C_p\left(p_0^2 + 2p_0\Delta n + \Delta n^2\right) + C_n\left(n_0^2 + 2n_0\Delta n + \Delta n^2\right)}, \tag{2.5}$$

which has been verified experimentally in silicon for a wide range of dopant concentrations [24, 25]. Since electrons may transfer both energy and momentum via the Auger process, the likelihood of Auger recombination is not strongly dependent on whether the band gap is direct or indirect.

The Auger coefficients C_n and C_p have been shown to vary with dopant concentration and injection level. For low-injection conditions ($\Delta n << p_0$) the values of C_n

and C_p at 300 K are given by the formula [25]

$$C_n = C_{n,0}\left[1 + 44\left[1 - \tanh\left(\frac{n_0 + \Delta n}{5 \times 10^{16}\ \mathrm{cm}^{-3}}\right)^{0.34}\right]\right], \tag{2.6}$$

$$C_p = C_{p,0}\left[1 + 44\left[1 - \tanh\left(\frac{p_0 + \Delta n}{5 \times 10^{16}\ \mathrm{cm}^{-3}}\right)^{0.29}\right]\right], \tag{2.7}$$

where $C_{n,0}$ and $C_{p,0}$ are the silicon Auger coefficients measured by Dziewior and Schmid: 2.8×10^{-31} $\mathrm{cm}^6\mathrm{s}^{-1}$ and 0.99×10^{-31} $\mathrm{cm}^6\mathrm{s}^{-1}$, respectively [24]. In the high-injection condition ($\Delta n >> p_0$), the Auger coefficient becomes the so-called ambipolar coefficient $C_a = C_n + C_p$ and is generally larger than the formulae above would predict; a typical measured value for C_a is 1.5×10^{-30} $\mathrm{cm}^6\mathrm{s}^{-1}$ for a highly doped sample. The discrepancy is usually attributed to an enhancement of the Auger process due to Coulomb interactions [26].

2.1.4 Recombination in Silicon Devices

The overall carrier lifetime τ_R may be given in terms of the lifetimes from the Shockley-Read-Hall, radiative, and Auger processes:

$$\tau_R = \left[\frac{1}{\tau_{SRH}} + \frac{1}{\tau_{rad}} + \frac{1}{\tau_{Auger}}\right]^{-1}, \tag{2.8}$$

where the individual terms are defined by Eqs. 2.2, 2.4, and 2.5. One can also define a bulk recombination rate R as the number of excess-carrier recombinations per cm^3 per second; this quantity is related to τ as

$$R = \Delta n/\tau, \tag{2.9}$$

and one finds that in the high-injection limit ($\Delta n >> p_0$) Eq. 2.8 can be written as

$$R = K_{SRH}\Delta n + K_{rad}\Delta n^2 + K_{Auger}\Delta n^3, \tag{2.10}$$

where the constants K can be derived from the formulae for the lifetimes τ.

It is clear that as the injected carrier concentration Δn is made large compared with the dopant and/or defect concentration in the semiconductor, the dominant recombination mechanism shifts from the SRH process to the Auger process. The fraction of radiative recombinations reaches a maximum somewhere in between. Since

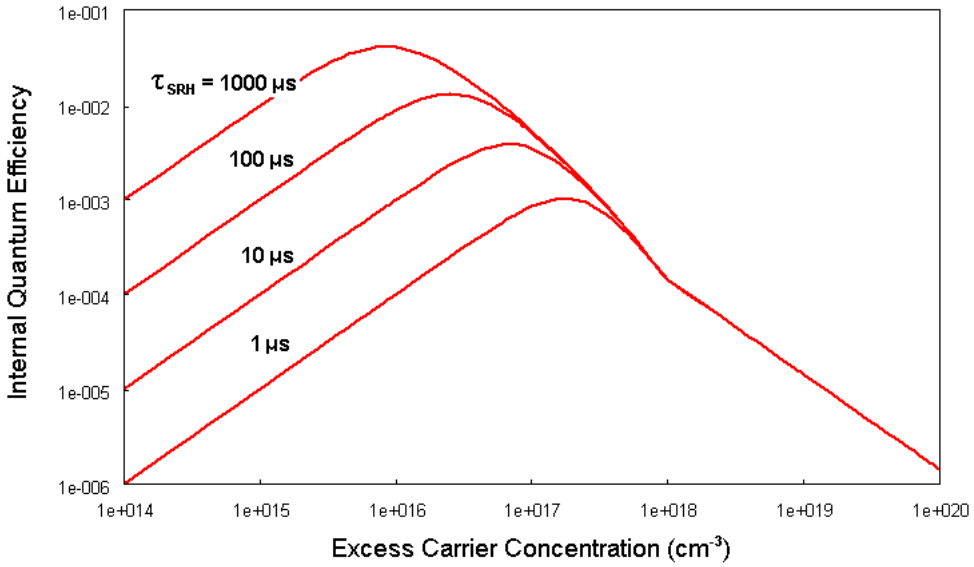

Figure 2.3: An estimate of the internal quantum efficiency in an ordinary silicon device, as characterized by Eq. 2.11. The silicon is p-type with a dopant concentration of 1×10^{15} cm^{-3}. A nearly perfect silicon crystal has an SRH lifetime on the order of 1 ms [29]. The SRH recombination lifetime for moderately doped silicon is typically around 1-20 μs [30].

only radiative recombinations generate photons, the *internal quantum efficiency* η_i of the material is defined as the fraction of the carriers injected into the crystal that undergo radiative recombination:

$$\eta_i = \frac{\tau_R}{\tau_{rad}}. \tag{2.11}$$

The silicon wafers used in the present research are boron-doped (p-type) with a dopant concentration p_0 of approximately 1×10^{15} cm^{-3}, which gives a minority carrier concentration n_0 of 1×10^5 cm^{-3}. Using these values, one can plot the quantum efficiency as a function of injected carrier concentration Δn; such a plot is shown in Figure 2.3. It shows that the maximum possible quantum efficiency of a silicon device is typically on the order of 10^{-2}, confirming that silicon is an inefficient light emitter compared to most III-V semiconductors. Internal quantum efficiencies in excess of 0.8 have been reported for devices made from GaAs [27, 28].

Although the derivation of internal quantum efficiency provides insight regarding

luminescence in different materials, the quantity itself cannot be measured directly; η_i does not take into account the possibility of photons being re-absorbed within the material or otherwise prevented from escaping and being detected in a real experiment. The number of detectable photons per injected charge carrier in a semiconductor device is referred to as the *external quantum efficiency*, η_x, which is always smaller than η_i and depends in part on the design and fabrication of the light-emitting device under test. The calculation of η_x for the present experiments can be found in Appendix A, and measured values of η_x are discussed in Chapter 5.

2.2 Possible EL Mechanisms in Silicon

As Section 2.1 demonstrated, ordinary crystalline silicon at room temperature cannot be an efficient light emitter. Nevertheless, researchers in the field of silicon photonics have succeeded in producing photo- and electroluminescent silicon using a variety of techniques, some of which were briefly listed in Chapter 1. In many cases, and especially in the case of ion-implanted silicon, the origin of the enhanced luminescence is not well understood. This section will describe several mechanisms that have been put forward to explain the phenomenon. A comprehensive discussion of the theoretical models underlying these hypotheses is beyond the scope of this research; the discussion here will be limited to the basic physical principles underlying each mechanism, and references to more thorough treatments of the theory will be given in each of the relevant subsections. The analysis described in Chapter 5 was conducted with these mechanisms in mind.

2.2.1 Quantum Confinement Effects

When charge carriers in a silicon crystal are confined in a potential well of very small dimensions (< 5 nm), their allowed energy states and transitions can be strongly altered, leading to more efficient luminescence, and at higher photon energies, than silicon would normally emit. The effect was first observed in photoluminescence studies of anodically etched porous silicon [31, 32] and has since been confirmed

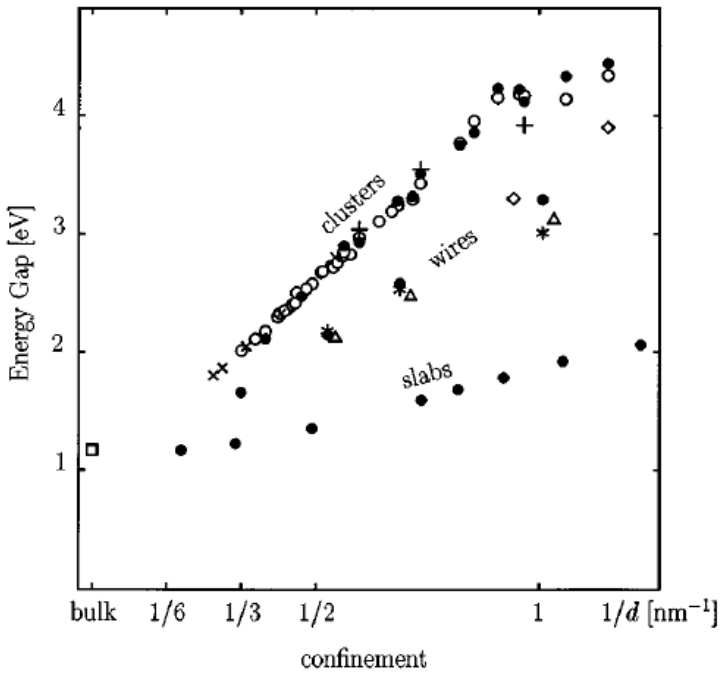

Figure 2.4: Effective energy gaps for various quantum-confined silicon structures. The terms "slab", "wire", and "cluster" refer to one, two, and three-dimensional confinement, respectively. The variable d that appears on the horizontal axis represents the width of the structure in the direction(s) of confinement. Taken from [35].

by the majority of experimental findings on porous silicon and silicon nanocrystals [33]. The increase in luminescence intensity through quantum confinement may be explained by an application of Heisenberg's uncertainty principle: whereas the electrons used to calculate the original bandstructure were essentially free, with well-defined momentum $\hbar\vec{k}$ and uncertain position $\vec{x}$, a strong localization in $\vec{x}$-space forces the electron (and hole) momentum to become uncertain. Consequently, nearly any phonon in the lattice develops a non-negligible likelihood of facilitating radiative transitions, instead of only phonons whose $\vec{k}$-values are equal to that of the band gap. In cases of extreme confinement, pseudodirect transitions may occur without the participation of any phonons [33, 34].

The increase in radiative energy from quantum-scale silicon structures may be explained, qualitatively, as follows. As the size of the silicon structure is reduced,

the allowed energy states of the system become widely separated; this is somewhat analogous to the simple particle-in-an-infinite-well problem, although the dependence of ΔE on d is different. The system can be modeled (using a pseudopotential) as the interaction between many valence electrons and a matrix of silicon nuclei and core electron shells. The construction and application of such a model may be found in the work of Delley and Steigmeier [35], and the results of several groups' calculations are shown in Figure 2.4. The data show that the gap energy grows monotonically with $1/d$, and that higher dimensions of confinement tend to produce wider energy gaps. Therefore, highly confined structures are expected to emit light at shorter wavelengths. Measurements performed by Wolkin et al. on silicon quantum dots (three confined dimensions) are in agreement with the data shown in Figure 2.4, though Wolkin also provides evidence that oxidation of the surface of the silicon nanocrystals changes their EL spectrum, which he attributes to carrier confinement at Si=O bond sites [36].

The increased luminescence intensity, coupled with the potential for spectral tuning by controlling the size of the silicon structures, makes quantum confinement very promising for the development of silicon light sources. Light element plasma ion implantation and subsequent annealing is known to produce small-scale structures beneath the surface of implanted silicon; at lower annealing temperatures (250 to 450°C) these take the form of nanoblisters that can only be detected through measurement of the lattice displacement field [37], whereas higher-temperature anneals coarsen the blisters into larger cavities [12, 13] and large surface blisters [38] that have been observed directly by electron microscopy, as in Figure 2.5. Quantum confinement may occur in the thin separations between adjacent cavities, whose size could be affected by the annealing temperature [37]. Also, the uncontrolled nature of plasma ion implantation must necessarily produce a wide range of cavity sizes and separations, which would explain the broad emission spectra exhibited by all ion-implanted silicon LEDs produced to date.

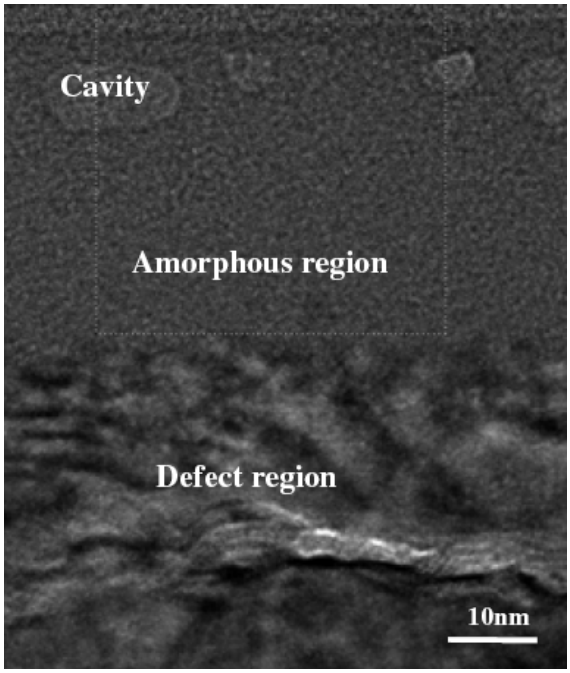

Figure 2.5: A transmission electron microscopy (TEM) image of ion-implanted silicon produced by Liu et al. The silicon was implanted with 1×10^{17} cm^{-2} H^+ ions and exhibited visible, broad-spectrum EL peaked at 578 nm. The top region is the silicon layer closer to the surface, where the high-dose implant amorphized the silicon crystal; the lower region is deeper in the material and was subjected to a lower effective ion dose. Based on secondary ion mass spectroscopy (SIMS) measurements of oxygen content, luminescence from this and similar devices was attributed to oxides present within the larger cavities [13].

2.2.2 Hydrogenated Silicon

Unbonded electrons on the surface of silicon crystallites, also called dangling bonds, can act as nonradiative Shockley-Read-Hall recombination centres. Because the process of ion implantation can significantly disrupt the lattice of a crystal target, ion-implanted silicon may contain a very high concentration of these dangling bonds, which could significantly reduce the luminescent efficiency of the crystal. Dangling bonds can be passivated (made less effective as SRH recombination sites) by the introduction of hydrogen atoms. Experiments conducted by Bisero et al. have shown

that the photoluminescence of silicon implanted with helium ions is strongly dependent on its passivation with hydrogen: samples annealed in a hydrogen atmosphere exhibited luminescence similar to hydrogen-implanted silicon, a broad peak centred around 700 nm, whereas samples annealed in vacuum exhibited no luminescence at all [37]. It should be noted, however, that these observations were made at 77 K, whereas the devices made and tested in the present research were electroluminescent at room temperature.

Delerue et al. have presented a two-stage model of capture-recombination at dangling bond sites. First, an electron or hole is captured by the neutral dangling bond, which becomes charged; the opposite carrier is subsequently captured by the charged bond and recombines with the first carrier. According to the model, this process can be radiative or nonradiative: although it is strongly nonradiative in bulk silicon, the shift in allowed energy states caused by quantum confinement can increase the likelihood of photon emission during recombination at dangling bond sites. The authors suggest that dangling bonds may contribute to luminescence in the infrared ($E < 1.4$ eV) and blue-green ($E > 2.2$ eV) portions of the spectrum, whereas luminescence between 1.4 eV and 2.2 eV, such as that observed by Bisero et al., should be suppressed by nonradiative recombination [39]. If this model is correct, hydrogen passivation of dangling bonds should change the EL spectrum accordingly.

2.2.3 Luminescence from Oxides

Silicon dioxide (SiO_2) is naturally present on any silicon surface exposed to air; this layer of *native oxide* saturates at a thickness of 0.01 nm at room temperature [40], but can grow quickly when the silicon is heated. A native oxide thickness of 1 nm is assumed to exist on all silicon surfaces used in the present research, in accordance with the measurements of Heikkilä et al [41]. SiO_2 can itself be a luminescent material, with visible bands reported at 1.9, 2.2, and 2.7 eV [42, 43]. This has prompted some researchers in the field of silicon photonics to question whether the observed luminescence from modified-silicon devices might originate from the oxide layer rather than from the silicon itself. In 1993, Qin and Jia sug-

gested that while quantum confinement in nanoscale silicon structures can provide a well of high energy electron-hole pairs, radiative recombination predominantly occurs at luminescent centres within the oxide layer surrounding the silicon crystal, not via band-to-band recombinations as was previously believed [44]. The proposed luminescent centres are primarily composed of silicon-oxygen complexes, but silicon hydrides and fluorides were also named as possible contributors. The theory, called the quantum-confinement-luminescent-centre (QCLC) model, was originally proposed to explain photoluminescence in porous silicon; specifically, it predicts that the dominant wavelength emitted by oxidized silicon nanostructures smaller than 8.7 nm should be around 1.8 eV (680 nm) regardless of the structures' size [45], which agrees with the findings reported by Wolkin et al. Since the radiative recombination in this model relies on carrier trapping at luminescence centres, its lifetime τ is not strongly dependent on the injected carrier concentration.

Although the QCLC model is primarily concerned with photoluminescence from nanoscale silicon, it can also be used to make a prediction regarding electroluminescence from silicon devices: namely, if the oxide layer is chiefly responsible for silicon luminescence, then luminescence at roughly the same wavelength should be expected from any metal-oxide-silicon device, regardless of the presence or absence of nanostructures. Several experiments have produced data in support of this hypothesis: Qin et al. observed electroluminescence peaked at 690 nm in Au-SiO_2-Si structures that disappeared when the oxide was removed [46], and Heikkilä et al. observed double-peaked EL at 570 and 660 nm in similar devices [41]. Neither experiment explicitly involved silicon nanostructures of any kind, though Qin et al. suggested that the oxide layer naturally contained silicon nanoparticles whose energy states were favourable for activating luminescent centres in SiO_2. Based on the QCLC model, these researchers proposed that radiative recombination in metal-oxide-silicon devices proceeds as shown in Figure 2.6: electrons injected into the metal contact tunnel into the oxide layer and have some probability of being trapped in defect levels within it. Similarly, holes entering the oxide through the silicon-oxide interface can become trapped in lower-energy defect states. Carriers that are trapped in this

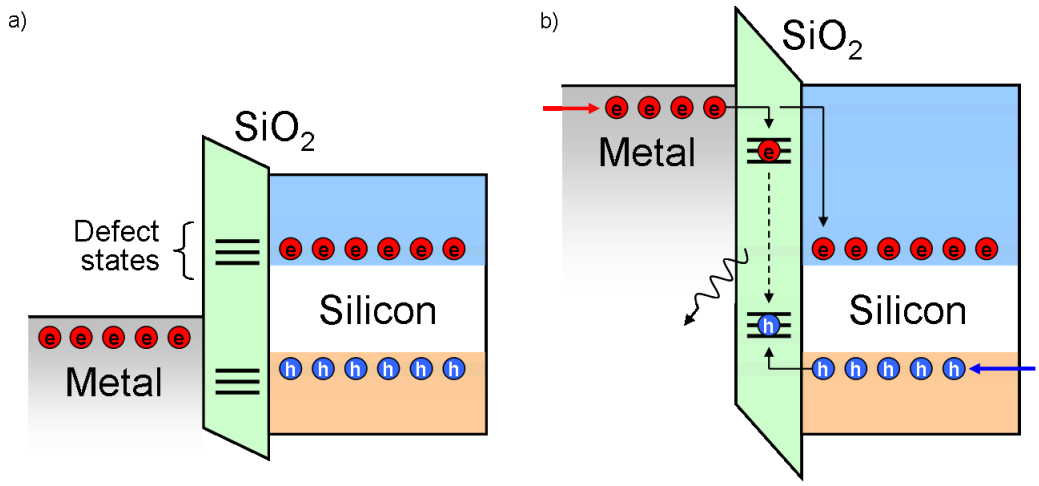

Figure 2.6: The model of oxide-driven electroluminescence in a metal-oxide-silicon device. Panel (a) shows the potential energy levels for electrons and holes for such a device when no external potentials are applied, whereas (b) shows the same device when the metal is biased negatively. Electrons injected into the metal tunnel into the oxide, where there exists a strong electric field; some are trapped in defect states within the oxide, while the remainder continue through to the silicon conduction band. Electrons trapped within the oxide can recombine radiatively with holes that tunnel in from the valence band. After [41].

manner can recombine radiatively within the oxide layer. Although the energy-band-based explanation of oxide EL does not require the quantum confinement aspect of the QCLC model, this theory of enhanced silicon EL will still be called the QCLC model to distinguish it from the purely structural, quantum-confinement-based theory discussed earlier in this Section.

2.3 Preliminary Experiments

Prior to the commencement of the present research, J.T. Steenkamp (a former M. Sc. student) and James Mantyka (a summer student) prepared a small number of electroluminescent, hydrogen-implanted silicon devices with a range of ion implant energies. The device preparation method for these experiments was similar to the procedure described in Chapter 4, except that the annealing was carried out in a

Fisher Scientific muffle furnace under a nitrogen atmosphere. Details of the plasma processing stage are presented in Table 2.1. The furnace was provided by the undergraduate laboratory at the Dept. of Chemistry at the University of Saskatchewan; thanks go to Dr. Pia Wennick for facilitating these experiments. A full account of the experiment and its results is reported in Ref. [15]. Some of the relevant results will be presented here to provide context for the present research and to serve as a point of comparison with the data presented in Chapter 5.

Each device exhibited visible-spectrum luminescence when subjected to an electric current of 1 A/cm^2, driven by an applied potential drop whose value ranged from 20 to 35 V. The EL spectra measured from the devices are shown in Figure 2.7. The data have been binned to reduce noise and adjusted to correct for absorption in the gold electrode; more detail regarding absorption in gold is provided in Section 4.9.2. Each spectrum was also normalized to the same maximum in order to investigate variation in the relative intensities of the peaks as a function of implant energy. Error bars in the data represent the quadrature sum of random error in the binned data and the estimated uncertainty in the thickness of the gold electrode.

The data show an apparent shift in the EL spectrum toward longer wavelengths as the ion implant energy was increased. In contrast, Liu et al., who performed a similar experiment using hydrogen PII, observed no significant correlation between EL spectrum and implant energy [13]. To investigate this relationship, the Gaussian fitting procedure outlined in Section 4.9.2 was performed on each EL spectrum; the

Table 2.1: Plasma parameters for preliminary hydrogen-implanted devices

Parameter	Value
Base pressure	1×10^{-6} Torr
Hydrogen gas pressure	1×10^{-2} Torr
Applied RF power	600 W
Electron Temperature	3 eV
Plasma Density	3×10^{10} cm^{-3}
Total Fluence (approx.)	2×10^{17} cm^{-2}

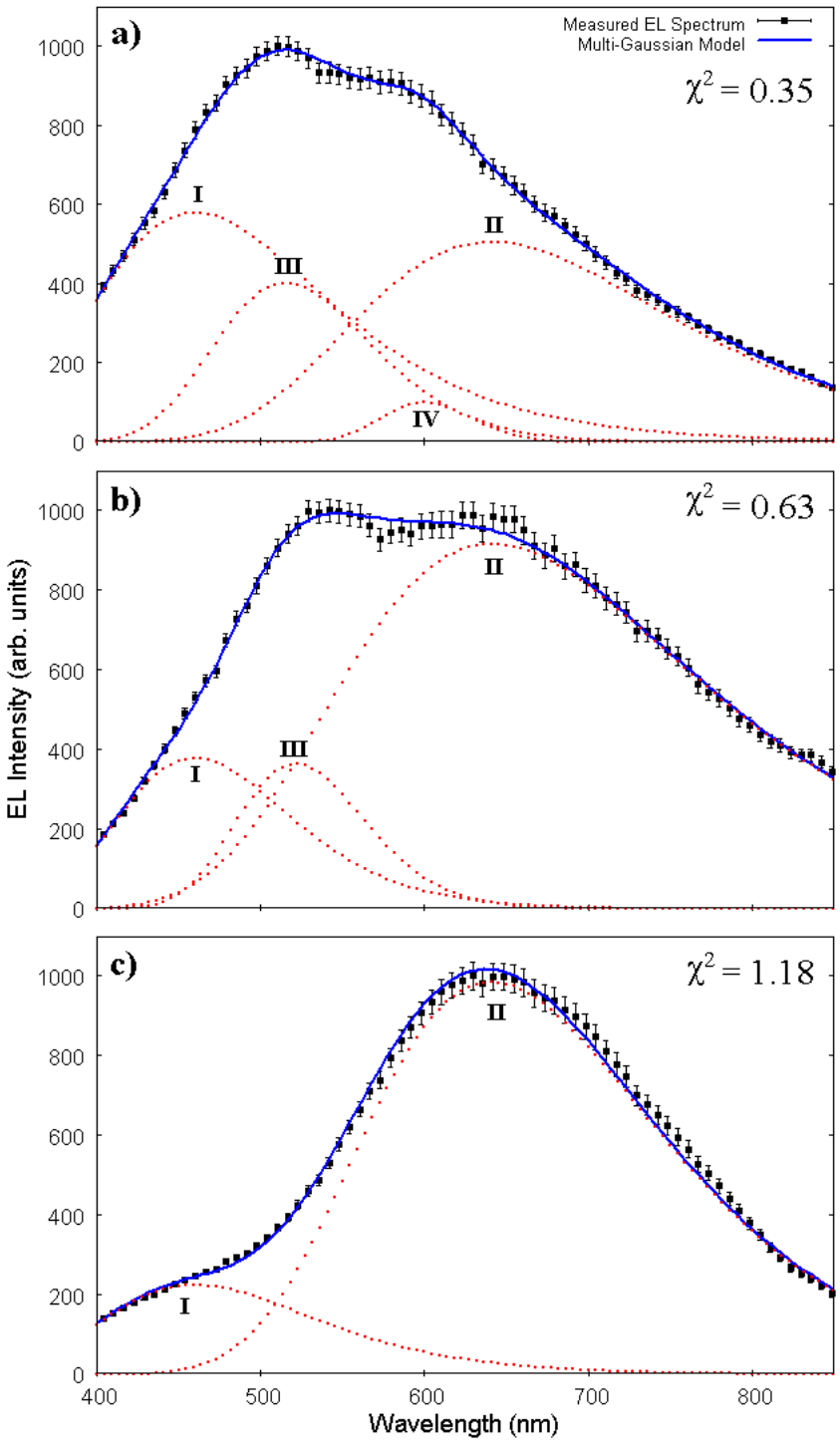

Figure 2.7: Electroluminescence spectra of the preliminary series of hydrogen-implanted silicon devices. Dotted lines represent individual Gaussian functions, the solid line shows the composite fit function, and points represent measured data. Ion implant energies were 7 keV (a), 15 keV (b), and 18 keV (c).

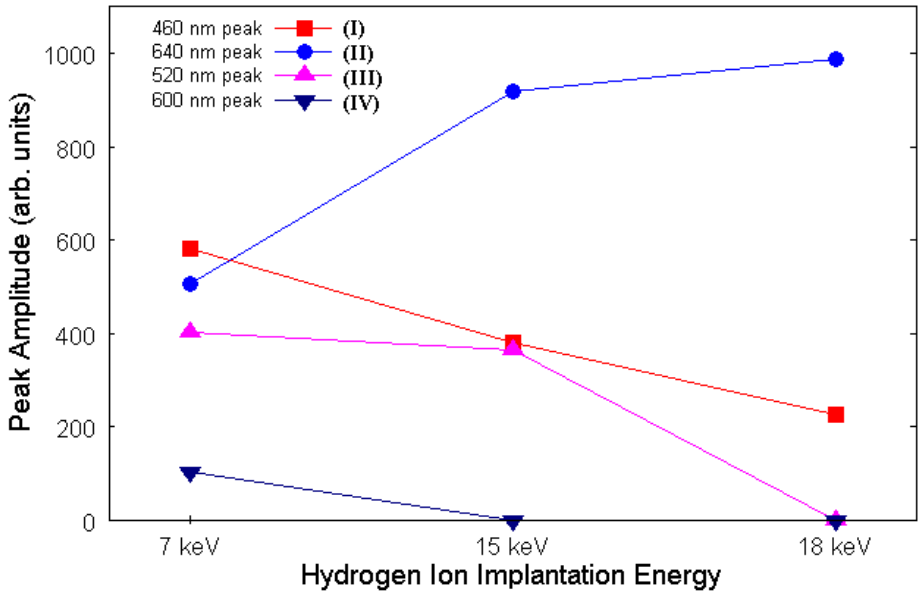

Figure 2.8: The relative intensity of each EL peak from the preliminary hydrogen-implanted devices as a function of the ion implantation energy. Peak labels correspond to those used in Figure 2.7.

resulting functions are shown in Figure 2.7, and the relative intensities of the individual peaks are plotted in Figure 2.8. The value of the reduced χ^2 (a parameter indicating goodness-of-fit) is conspicuously low for the 7 kV and 15 kV implanted samples, suggesting that the model may use too many parameters; specifically, peak IV in the 7 kV implanted sample may not actually exist. Nevertheless, the experiment demonstrated that the ion implant energy can affect the energy distribution of photons emitted from hydrogen-implanted silicon devices. These results served as the inspiration for the present research into light-ion-implanted silicon diodes.

Chapter 3

Plasma Ion Implantation

Ion implantation is a process in which a target material is bombarded with energetic ions in order to change its properties on or near the surface. Applications for this technique include: the controlled implantation of impurities into semiconductors; improving the surface properties of a metal, such as its corrosion resistance or coefficient of friction; and producing buried layers of altered refractive index within optical materials to produce high-efficiency waveguides [47]. The main goal of the present research is to investigate the relationship between the ion implantation process and the luminescent properties of ion-implanted silicon diodes.

Two methods exist for performing ion implantation. The first, ion beam implantation, requires ions to be extracted from a remote source, collimated into a beam, and accelerated toward the target. This presents a number of technical difficulties and limitations. To limit sputtering, the surface of the target must be normal to the direction of the beam, so only planar targets may be implanted in this way. The beam has a limited area, so larger targets must be scanned back and forth, and care must be taken to ensure an even implant. The ion flux out of the source is also limited, so implanting a large quantity of ions requires a long time. The chief advantage of this process is its controllability: ion mass and energy can be precisely selected while directing the beam, ensuring that only the desired particles are delivered to the surface [47].

Plasma ion implantation (PII), first developed in the late 1980's, is an alternative ion implantation technique that offers many advantages over traditional beam implantation. In PII, the target is immersed in the ion source (a plasma) and electrically biased to a negative potential by an external energy source. The resulting

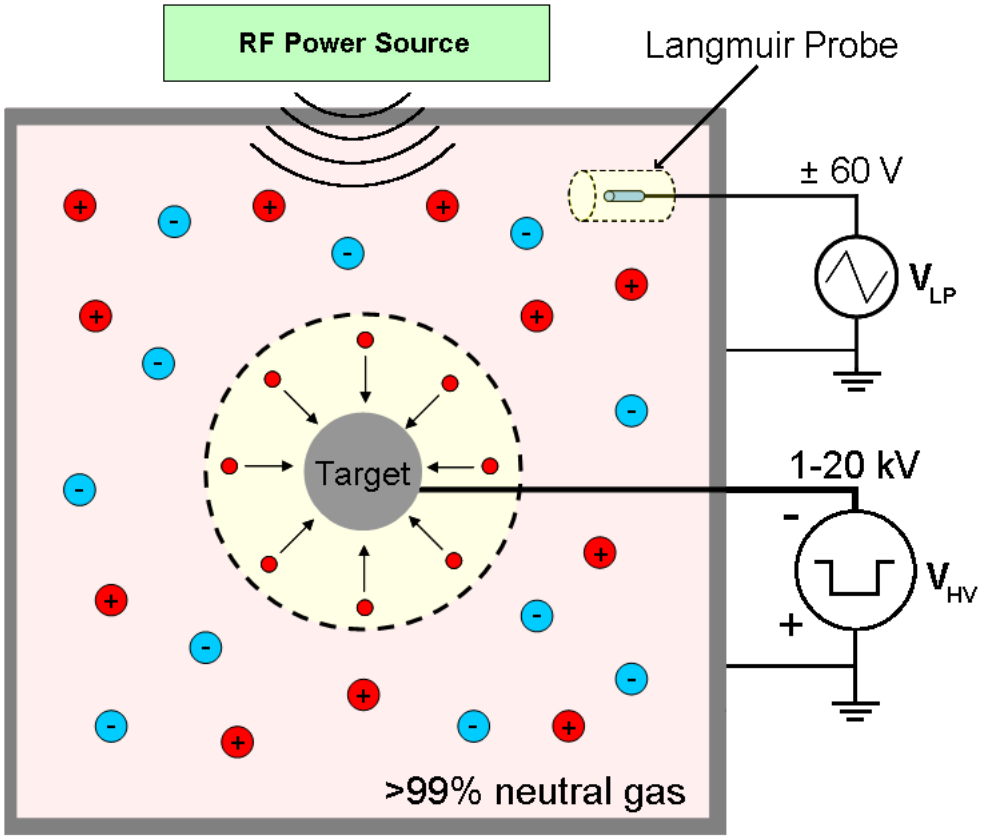

Figure 3.1: Schematic diagram of the plasma ion implantation process. An external RF source delivers power into a vacuum chamber, which is filled with neutral gas to a pressure of approximately 10 mTorr. This ionizes a small fraction of the gas atoms to form a plasma, depicted as an assortment of ions (+) and electrons (-) in the chamber. The silicon target in the center is periodically pulsed to a highly negative potential (V_{HV}), which propels ions toward, and implants them beneath, its surface. Meanwhile, the plasma density and temperature are measured using the Langmuir probe as outlined in Section 3.3. The yellow regions surrounding the two conductors represent *plasma sheaths*, regions of low electron density that will be described in Section 3.2.

electric field attracts ions from the plasma and accelerates them toward the target with energy equal to the applied potential. Because the target is immersed in the ion source, all incident ions are automatically normal to the target surface, and the exposed surface of the target receives a uniform ion dose. The dose delivered to the target is typically much higher than in beam implantation, and can be controlled by varying the density of the plasma, allowing implants to be completed in much less time. Furthermore, the apparatus (described by Figure 3.1) is less complex and can be assembled at a lower cost. The only significant drawback to the PII process is that the implanted ions cannot easily be selected for either mass or energy: all ion species are drawn from the plasma simultaneously, and the biasing pulse must take a finite time to ramp up and ramp down. Nevertheless, PII has found many applications in the fields of semiconductor processing and metallurgical enhancement [48, 49]. PII has already been used on a limited scale in the field of silicon photonics, with promising results [12, 13, 29, 37, 50, 51]. Because the technique allows for the production of many devices on short timescales and at low cost, PII was the method used to perform the present research in silicon photonics.

3.1 Plasma Overview

A plasma is a gaseous mixture in which an appreciable fraction of gas particles have been ionized. The presence of charged particles in the gas makes it responsive to electric and magnetic fields over large distances, which leads to collective action as the particles interact with external fields and with each other. Magnetic fields in PII plasmas are typically very weak, and the analysis presented in this chapter assumes that magnetic effects are negligible. Because the plasma began as a neutral gas, there must be equal quantities of positive and negative charge within it; furthermore, electric forces tend to distribute the charge such that the net charge density, and therefore the net electric field, is zero throughout the plasma. This property is called *quasineutrality* and must hold true in any unperturbed plasma, which will be referred to as *bulk plasma*. Perturbations in the plasma, such as charged conductors, create

local fields that separate charge and violate quasineutrality in the vicinity of the perturbation.

In order to perform a quantitative analysis on a PII plasma, one requires knowledge of three properties: the *plasma density*, the *electron temperature*, and the *plasma potential*. These properties are described below, and can be measured *in situ* using a Langmuir probe. The theory behind the Langmuir probe is explained in Section 3.3, while the design and operation of the probe itself are discussed in Section 4.4.

Plasma Density

The plasma density, n_0, is the density of electrons within the plasma. Since quasineutrality requires that the electron density must equal the positive charge (ion) density, the densities of all other charged particles may (in principle) be determined from n_0.

Electron Temperature

The electron temperature, T_e, describes the width of the electrons' velocity distribution $f(v_e)$, which is typically assumed to be a Maxwellian distribution [52]:

$$f(v_{e,j}) = n_0 \left(\frac{m_e}{2\pi T_e}\right)^{\frac{3}{2}} \exp\left(-\frac{m_e \left|v_e\right|^2}{2T_e}\right), \tag{3.1}$$

where $|v_e|$ represents the magnitude of the electron's velocity in three dimensions. Thus, higher values of T_e correspond to higher average electron speeds. By convention, the electron temperature in processing plasmas is given in units of energy (eV), with the Boltzmann factor k included within T_e.

Plasma Potential

The plasma potential, V_p, is the electric potential of the bulk plasma. In general, V_p may be set to any convenient value, since electric potential is a relative quantity. However, in some cases (such as the Langmuir probe analysis in Section 3.3) there is a body in the system whose potential is referenced to an external ground; in such situations, V_p becomes an unknown parameter that must be measured.

3.2 Plasma Sheaths

Because it is composed of charged particles, a plasma tends to surround any intruding source of electric fields (such as a charged conductor) with a region of heightened charge density; this effect restricts the intruding field to a small region immediately surrounding the source. Nearly all the energy difference between the bulk plasma potential V_p and the potential of the intruding object V_0 is dropped across this region, which is called a *plasma sheath*. The strength of the screening effect depends on the plasma density and temperature: its characteristic length scale, the electron Debye length, is defined as [52]

$$\lambda_{De} = \sqrt{\frac{\epsilon_0 T_e}{n_0 e^2}}, \tag{3.2}$$

where all symbols are defined in the List of Symbols on page *xi*. Depending on the strength of the intruding electric field, a sheath may be tens or hundreds of Debye lengths wide, but the physics governing the sheath region are essentially the same in each case.

Outside the sheath, the plasma is largely unperturbed and the electric field is nearly zero, as in any bulk plasma. Inside the sheath, quasineutrality is broken, and the electric field may be very large. All sheaths discussed in this document are formed around negatively-charged electrodes; that is, the field surrounding the intruding object tends to push electrons away and draw ions in, creating a sheath that is ion-rich and electron-poor.

In the steady-state condition, the sheath acts like the space within a plane-parallel diode, and the ion current follows a relation similar to the Child-Langmuir law for space charge limited current in such a system. This situation will be discussed at length in Section 3.2.2. However, if the conductor's potential V_0 is changed very rapidly, the faster-moving electrons can leave behind a region of uniform ion density behind as they are pushed away; this creates a short-lived configuration called a Matrix sheath that will be discussed in Section 3.2.1. Lastly, there must exist a region between the sheath proper and the bulk plasma, called the transition region

or presheath, that may affect the properties of the sheath in subtle ways. These issues will be briefly discussed in Section 3.2.3.

The behaviour of plasma sheaths is relevant to plasma ion implantation for two reasons: first, the space charge limited flow of ions through the Child-Langmuir sheath can be measured with a simple Langmuir probe, and analysis of the relationship between probe potential and measured current yields information about the density and temperature of the bulk plasma.

Second, the electric field within the sheath surrounding the silicon target shown in Figure 3.1 is what accelerates ions toward its surface. Using information obtained from the Langmuir probe, one can model the behaviour of the sheath region to predict the number of ions that will be implanted by a given voltage pulse, as well as the energy distribution of those ions at the point of impact. Past M. Sc. students M. Risch and J. T. Steenkamp have developed and tested such a model [53, 54] based on the work of M. Lieberman [55], which is employed in the present research to estimate the number of ions delivered to the silicon targets. An overview of the model will be presented in Section 3.4.

3.2.1 Matrix Sheath

If the conductor potential V_0 is sufficiently large compared with T_e, the situation may arise where the more mobile plasma electrons are ejected from the sheath region before the slower, more massive ions have time to react to the electric field. Such a sheath is called a Matrix sheath and is characterized by a uniform ion density $n_{i,s}$ within the sheath region. The Matrix sheath is not self-consistent, and it must eventually evolve into a steady-state Child-Langmuir sheath over a timescale t_m [56]:

$$t_m \cong \frac{\sqrt{2}}{9}\sqrt{\frac{\epsilon_0 m_i}{e^2 n_0}}\left(\frac{2V_0}{T_e}\right)^{\frac{3}{4}} \tag{3.3}$$

which, for a typical hydrogen PII discharge with pulse voltage V_0 of -5 kV, is 740 ns. Although the Matrix sheath is short-lived, its ion density is very high compared with that of the Child-Langmuir sheath, and it can contribute a substantial portion of the total ions implanted by the PII process. The contribution of the Matrix sheath

is taken into consideration in the PII fluence prediction model discussed in Section 3.4.

3.2.2 Child-Langmuir Sheath

When the short-lived Matrix sheath decays, the steady-state arrangement that follows is the space charge limited flow of ions from the plasma (an infinite ion source) to the grounded or negatively biased conductor (an infinite ion sink). This is called a Child-Langmuir sheath, and is depicted graphically in Figure 3.2. Due to the similarity with a plane-parallel diode, the ion current through the sheath should obey a relation similar to the Child law for plane-parallel diodes [57],

$$J_i = \frac{4}{9}\epsilon_0\sqrt{\frac{2e}{m_i}}\frac{(V_0 - V_s)^{\frac{3}{2}}}{(r_0 - r_s)^2}, \tag{3.4}$$

where V_0, V_s, r_0, and r_s are all defined for the sheath region by Figure 3.3. One also expects that a geometric correction to this equation will be necessary if the object under analysis is not planar. Given Eq. 3.4 as a starting point, one must find expressions for V_s and r_s as well as their precise relationship to the ion current density J_i in order to carry out a quantitative analysis of the sheath. The presheath region is somewhat more complex and will be discussed separately in Section 3.2.3.

Simplifying Assumptions

All of the following analysis is based on a few simplifying assumptions:

1. **No collisions occur within the sheath.**

This means that the mean free path of ions in the sheath λ_P must be greater than the width of the sheath, which may be on the order of a hundred Debye lengths λ_{De} as defined in Eq. 3.2. The mean free path is

$$\lambda_P = \frac{1}{N\sigma}, \tag{3.5}$$

where N is the density of scattering centres and σ is the effective cross-section for the scattering process in question. In the weakly ionized plasma used for PII, collisions

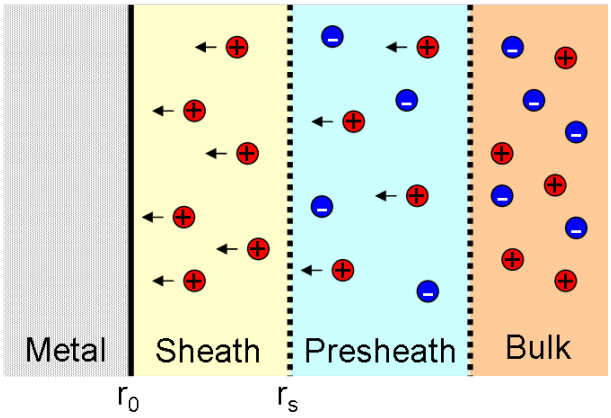

Figure 3.2: A graphical depiction of the steady-state Child-Langmuir sheath. Ions drift into the presheath region from the bulk plasma with near-zero initial velocity. The weak field within the nearly-quasineutral presheath (see Section 3.2.3) accelerates these ions toward the sheath region at r_s, where a much stronger field propels them toward the conductor at r_0.

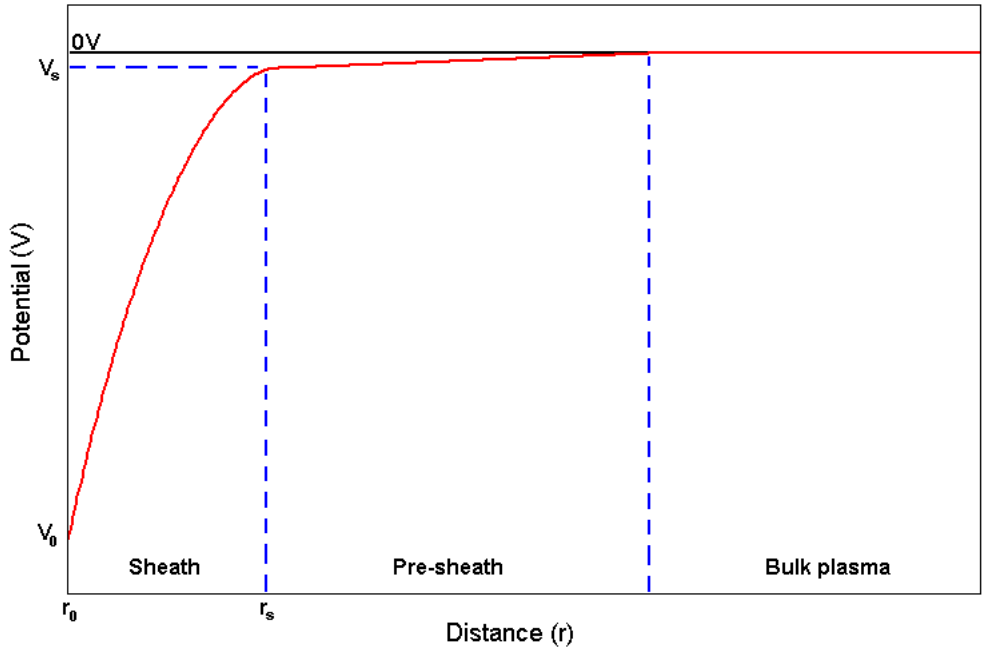

Figure 3.3: Electric potential within the sheath region shown in Figure 3.2. The sheath surrounds a conductor, biased to a potential V_0, whose surface lies at $r = r_0$. r is the co-ordinate normal to the surface of the conductor. The sheath boundary, which separates the sheath region from the presheath and bulk plasma, is shown in blue and marked as (r_s, V_s).

are dominated by charge-exchange scattering between charged particles and neutrals [58], so N becomes the neutral density n_n. The cross-section for the charge-exchange interaction σ_{CX} is only weakly dependent on ion energy in the energy range of 1-20 keV, and will be assumed to be constant. The values of σ_{CX} for the relevant gases are given in Table 3.1; note that deuterium and hydrogen plasmas are assumed to share the same value of σ_{CX} [59]. The remaining quantities used to calculate the mean free paths, given a neutral gas pressure of 10 mTorr, are

$$\begin{aligned} T_e &= 3.00 \text{ eV}, \\ n_0 &= 1.00 \times 10^{16} \text{ m}^{-3}, \\ N &= 3.21 \times 10^{20} \text{ m}^{-3}. \end{aligned} \tag{3.6}$$

Table 3.1: Mean free paths of various ion species

Neutral Particle	Cross Section σ_{CX} (m^2)	Mean Free Path (m)	Ref.
H_2	4×10^{-20}	7.8×10^{-2}	[60]
D_2	4×10^{-20}	7.8×10^{-2}	[60]
He	6×10^{-20}	5.2×10^{-2}	[61]

For the given values of T_e and n_0, the Debye length λ_{De} is equal to 1.29×10^{-4} m. Table 3.1 shows that $\lambda_P > 100\lambda_{De}$ for all the listed ion species, so it is reasonable to assume the sheaths in the present experiments to be collisionless.

2. The electric potential of the bulk plasma is zero.

This is actually a choice, rather than an assumption, since the zero point of electric potential is arbitrary in most situations. The electric potential of a plasma within a grounded chamber tends to float positive due to the presence of the electron-poor Child-Langmuir sheath; if the plasma is used as the zero-point for electric potential, the potential at the chamber wall must be negative. However, this choice will *not* be valid for the analysis of the Langmuir probe in Section 3.3 because the probe potential must be referenced to the grounded wall rather than to the bulk plasma.

3. The number of electrons absorbed by the conductor is negligible.

The first consequence of this assumption is that the conductor potential must be negative with respect to the plasma, since a positively-charged conductor would attract a large electron current. Therefore, given that the bulk plasma is at zero potential, $V(r) < 0$ for all positions r within the sheath. Second, the assumption allows one to find a simple expression for the electron density within the sheath region. To understand this, consider an electron that enters the sheath, traveling normal to the conductor surface, with velocity $v_{e,0}$. At any position r within the sheath, the electron's velocity normal to the surface, $v_{e,r}$, must follow the normal (Gaussian) distribution

$$f(r, v_{e,r}) = n_0 \left(\frac{m_e}{2\pi T_e}\right)^{\frac{1}{2}} \exp\left(\frac{eV(r)}{T_e}\right) \exp\left(-\frac{m_e v_{e,r}^2}{2T_e}\right), \tag{3.7}$$

which can be obtained from Eq. 3.1. This distribution should be symmetric at all points in the sheath. However, the possibility exists that electrons may impact the conductor and be absorbed by it; when this occurs, some electrons are "missing" from one tail of the distribution, so Eq. 3.7 becomes a truncated Gaussian. In this case, the electron density n_e within the sheath is

$$n_e(r) = \frac{1}{2} n_0 \exp\left(\frac{eV(r)}{T_e}\right) \left[1 + \operatorname{erf}\left(\frac{e(V(r) - V_0)}{T_e}\right)\right]. \tag{3.8}$$

To simplify this expression, one must assume that very few electrons possess enough energy to reach the conductor; this is the same as asserting $\operatorname{erf}\left(\frac{e(V(r)-V_0)}{T_e}\right) \cong 1$, or imposing a condition on the electric potential at the point r:

$$e\left(V(r) - V_0\right) \gg T_e. \tag{3.9}$$

Applying this condition to Eq. 3.8, the electron density within the sheath is

$$n_e(r) = n_0 \exp\left(\frac{eV(r)}{T_e}\right), \tag{3.10}$$

but only so long as the conductor potential V_0 is sufficiently negative, and the position r far enough from its surface, to satisfy condition 3.9.

4. The ion temperature T_i is zero.

The PII apparatus employs an RF power source to generate an inductively coupled plasma (ICP). The process is designed to energize free electrons and uses electron-neutral collisions to generate ions. This establishes a gross inequality in electron and ion temperatures: while the electron temperature T_e in an ICP may be as high as 5 eV, the ion temperature T_i is typically no more than 0.1 eV [62]. Because ions are constantly being lost to the chamber wall and replaced within the bulk plasma, the average ion thermal energy cannot rise substantially over time, and thus remains small enough to ignore.

Neglecting the ion temperature allows one to easily determine the ion density in the sheath region. If the ion thermal velocity is zero, the velocity v_i of an ion at position r within the sheath must be

$$v_i(r) = \sqrt{\frac{-2eV(r)}{m_i}}, \tag{3.11}$$

and conservation of ion current I_i (as a function of position) requires that

$$I_i(r) = A(r)en_i(r)v_i(r) = constant \tag{3.12}$$

which defines the ion density, $n_i(r)$, as a function of the sheath surface area, $A(r)$. r is the co-ordinate normal to the surface of the conductor under consideration. The sheath surface area depends on the shape of the conductor; if the conductor is an infinite sheet, then $A(r)$ is a constant, whereas for a long cylindrical conductor of length L, $A(r) = 2\pi rL$. This assumption permits one to ignore the more complex theory of sheath analysis, the orbital-motion-limited (OML) theory [63], on the basis that all ion motion must be perfectly normal to the conductor's surface.

Sheath Potential

The next step in the analysis of the Child-Langmuir sheath is the determination of the electric potential at the sheath boundary, V_s from Figure 3.2. Following the procedure found in *Principles of Plasma Diagnostics* [64], one begins by observing

from Eqs. 3.11 and 3.12 that

$$n_i(r) = n_i(r_s)\sqrt{\frac{V(r_s)}{V(r)}}, \tag{3.13}$$

and if quasineutrality is applied at the sheath boundary ($n_i(r_s) = n_e(r_s)$) and Eq. 3.10 is used to evaluate n_e, one finds

$$\begin{aligned} n_i(r) &= n_e(r_s)\sqrt{\frac{V(r_s)}{V(r)}}, \\ &= n_0 \exp\left(\frac{eV(r_s)}{T_e}\right)\sqrt{\frac{V(r_s)}{V(r)}}. \end{aligned} \tag{3.14}$$

Inserting this result into Poisson's equation, and using the definition $V(r_s) = V_s$, returns

$$\begin{aligned} \nabla^2 V(r) &= -\frac{e}{\epsilon_0}(n_i - n_e), \\ &= -\frac{en_0}{\epsilon_0}\exp\left(\frac{eV_s}{T_e}\right)\left[\sqrt{\frac{V_s}{V(r)}} - \exp\left(\frac{eV - eV_s}{T_e}\right)\right]. \end{aligned} \tag{3.15}$$

A Taylor expansion of Eq. 3.15 about the sheath boundary (that is, about $V(r) = V_s$) returns

$$\nabla^2 V(r) = \frac{en_0}{\epsilon_0}\exp\left(\frac{eV_s}{T_e}\right)\left[\frac{1}{2V_s} + \frac{e}{T_e}\right](V(r) - V_s). \tag{3.16}$$

Only monotonic solutions to this equation are physical; the potential $V(r)$ does not oscillate within the sheath region. Keeping in mind that $(V(r) - V_s) < 0$ within the sheath region, this imposes an upper bound on the sheath potential V_s:

$$V_s \leq \frac{-T_e}{2e}. \tag{3.17}$$

To find the lower bound on V_s, one must return to the original expressions for ion and electron density (Eqs. 3.10 and 3.12), impose quasineutrality, and take the derivative of the result:

$$-\frac{dV}{dr}\left(\frac{1}{2V(r)} + \frac{e}{T_e}\right) = \frac{1}{A(r)}\frac{dA}{dr}. \tag{3.18}$$

By inspection, the right side of this equation must be positive for any physical conductor. When the term containing $V(r)$ is zero, the derivative dV/dr must be infinite,

which indicates that quasineutrality breaks down at the point where $V(r) = -T_e/2e$. Given that the region outside the sheath *must* be quasineutral (by definition), the point where $dV/dr \to \infty$ must lie within the sheath region. Therefore, the sheath boundary cannot be closer to the conductor than this point, which imposes a condition on the sheath potential:

$$V_s \geq \frac{-T_e}{2e}. \tag{3.19}$$

From the boundary conditions in Eqs. 3.17 and 3.19, then, the value of the sheath potential V_s must be

$$V_s = \frac{-T_e}{2e}. \tag{3.20}$$

The value of V_s also determines the speed that ions possess when crossing the sheath boundary, called the Bohm velocity v_B; this is the speed they acquire as they pass through the presheath from Figure 3.2. If one inserts the result from Eq. 3.20 into the expression for ion velocity (Eq. 3.11), the result is [52]

$$v_B = \sqrt{\frac{T_e}{m_i}}. \tag{3.21}$$

The fact that the Bohm velocity is substantially greater than the negligible ion thermal velocity is evidence for the existence of the pre-sheath region between sheath and bulk plasma; this will be discussed further in Section 3.2.3.

Sheath Boundary Position

Determining the location of the sheath boundary r_s is more difficult than finding the sheath potential V_s. To do so, one must consider Poisson's equation in the sheath region, once again making use of Eq. 3.12 for the ion density, and assuming that the electron density is small enough to neglect. The result is

$$\nabla^2 V = -\frac{e}{\epsilon_0}\frac{I_i}{A(r)}\sqrt{\frac{m_i}{-2eV(r)}}, \tag{3.22}$$

where I_i, the ion current, does not depend on the distance r from the conductor surface. However, the change in collecting area $A(r)$ as a function of r may not be negligible.

If the conductor is very large compared with the electron Debye length λ_{De} from Eq. 3.2, the sheath collecting area becomes a simple constant A, and integration of Eq. 3.22 over the sheath region yields

$$\frac{r_s}{\lambda_{De}} = 1.21 \left[\left(\frac{-eV_0}{T_e} \right)^{\frac{1}{2}} - \frac{1}{\sqrt{2}} \right]^{\frac{1}{2}} \left[\left(\frac{-eV_0}{T_e} \right)^{\frac{1}{2}} + \sqrt{2} \right], \tag{3.23}$$

where V_0 is the electric potential at the conductor surface, as always. In the limit where $V_0 \gg V_s$, Eq. 3.23 reduces to

$$r_s = \frac{\sqrt{2}}{3} \exp\left(\frac{1}{4}\right) \lambda_{De} \left(\frac{eV_0}{T_e} \right)^{\frac{3}{4}}. \tag{3.24}$$

This equation is valid for the high-voltage pulses applied to the target in the PII process and is used in the fluence prediction model discussed in Section 3.4.

In the case where the conductor size is comparable to the electron Debye length, one cannot assume that $A(r)$ is constant throughout the sheath region. This means that Eq. 3.22 cannot be solved analytically and a numeric technique must be used instead to find r_s. Such is the case for the Langmuir probe used in the present experiments: it is a cylinder of radius 0.75 mm, which is of the same order as λ_{De} and certainly smaller than the sheath width for typical plasma conditions. For a cylindrical sheath, Eq. 3.22 may be rewritten as

$$\frac{\partial^2 V}{\partial r^2} = -\frac{1}{r}\frac{\partial V}{\partial r} - \frac{1}{r}\left(\frac{e}{\epsilon_0} \frac{I_i}{2\pi L} \sqrt{\frac{m_i}{2e}} \right) (-V)^{-\frac{1}{2}}, \tag{3.25}$$

where L is the length of the cylindrical conductor.

A simple algorithm for solving first-order differential equations, called the fourth-order Runge-Kutta method (RK4), is used to compute the value of r_s in the cylindrical geometry. Before applying RK4 to the problem, Eq. 3.25 must be recast into a system of first-order differential equations:

$$\frac{d}{dr}V' = -\frac{1}{r}V' - \frac{1}{r}\left(\frac{I_i}{2\pi L \epsilon_0} \sqrt{\frac{m_i}{2e}} \right) (-V)^{-\frac{1}{2}}, \tag{3.26}$$

$$\frac{d}{dr}V = V'. \tag{3.27}$$

This system can be solved to find the value of $V(r)$ at all points within the sheath region. However, the RK4 algorithm requires a complete set of values $(r, V(r), V'(r))$

for a single point, from which it computes the value of V at all other points. The only known facts about any particular points in the sheath region are:

$$V'(r_s) = 0,$$
$$V(r_s) = -\frac{T_e}{2e},$$
$$V(r_0) = V_0,$$

where r_0 is the radius of the cylindrical conductor, and V_0 is the bias applied to the conductor, as before. This does not constitute a complete set of information about any point, so the following procedure was developed to find the value of r_s:

1. Begin with a starting value (or guess) for the sheath boundary location r_s.
2. Solve for $V(r)$ using the RK4 algorithm.
3. Compute the value of V at the point $r = r_0$ for this solution; call this V_1.
4. Compare V_1 with the true value for the conductor potential, V_0.
5. Improve the original estimate r_s to find a new estimate r_s^1 using the formula

$$r_s^1 = r_0 + (r_s - r_0)\sqrt{\left|\frac{V_0}{V_1}\right|} \tag{3.28}$$

6. Repeat until the solution converges to within a predefined tolerance.

Both the RK4 algorithm and the procedure given above have been implemented in C++, with satisfactory results. Figure 3.4 shows the calculated relationship between sheath width and ion current for a given electron temperature and conductor potential. The ion current into a conductor is easily measurable and is proportional to the plasma density: denser plasmas deliver more ions to the sheath region. Therefore, as ion current increases, the plasma becomes denser and the sheath becomes narrower. One expects that the sheath width should converge to the planar-sheath value as the sheath becomes small compared with the conductor radius, but the data show that the numerical solution is smaller by a factor of 1.1906 in this limit. The discrepancy persists even if several non-planar elements are removed from Eq. 3.22. It is also

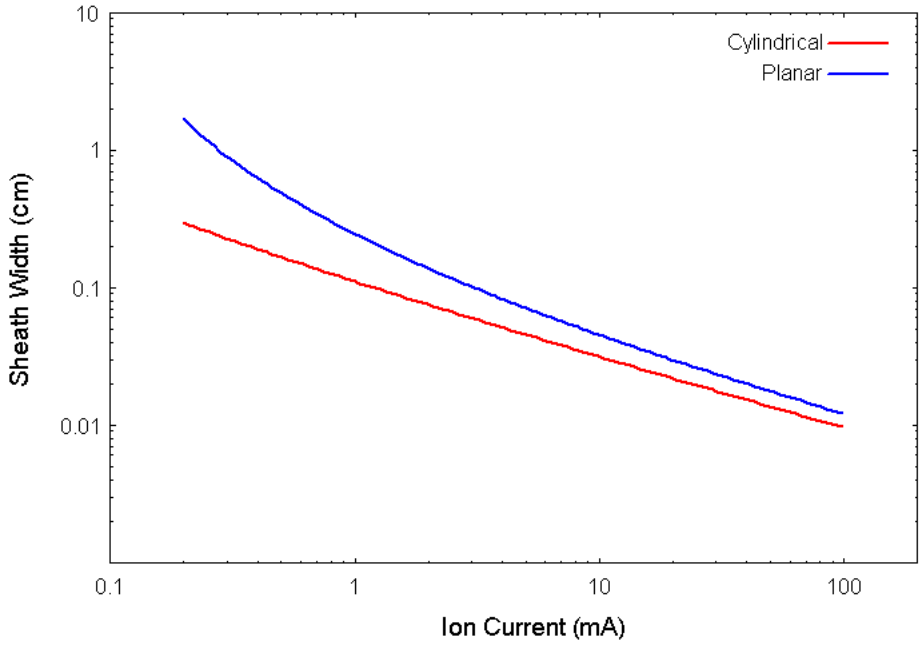

Figure 3.4: The sheath width for a cylindrical conductor, as a function of measured ion current into said conductor. The cylindrical result (red) was calculated via the RK4 method, while the planar sheath width (blue) was found using an analytical solution. The parameters of the calculation were: $T_e = 3$ eV, $V_0 = -50$ V, and a cylinder of radius 0.75 mm and length 8.5 mm. The 19% difference between the widths in the high-density limit is attributed to an inconsistency between the way the planar solution was derived and the way it was used to calculate the sheath width.

unlikely to be the result of accumulated numerical error because the value of the factor remains constant even when the parameters of the calculation are changed by orders of magnitude. The RK4 implementation in C++ has been thoroughly tested on differential equations with known solutions and appears to be sound. Presently the 19.06% discrepancy is attributed to the cylindrical geometry of the problem: when the planar approximation is employed to find the planar sheath width, the formula used for the sheath area must be for the area of a cylindrical object, thus implicitly violating the initial assumptions of the calculation.

3.2.3 Pre-Sheath Region

Since the potential at the sheath boundary V_s is not equal to the potential of the bulk plasma, one is left with an apparent contradiction: there must be an electric field in the quasineutral region beyond the sheath. The solution to this problem is to introduce a presheath region between the sheath and the bulk plasma, in which a smooth transition between the collision-dominated plasma and the collisionless sheath may be found. Numerous analytic solutions to the problem have been put forth: first by Tonks and Langmuir [65], whose work was followed by Lam [66] and Riemann [67], among others. The properties of the presheath likely have some influence over the Langmuir probe measurements: for example, it is known that as the conductor potential V_0 becomes more negative with respect to the plasma, the presheath conditions change so as to enhance the ion current into the conductor [68]. However, these corrections are small compared with the other sources of error in the measurements, and so the effects of the presheath have been ignored in the calculations presented here.

3.3 Langmuir Probe Analysis

With the understanding of the Child-Langmuir sheath potential and sheath edge position from Section 3.2.2, it is possible to probe the plasma with an electric field in order to determine its temperature and density. The simplest such probe, called a Langmuir probe, is a small piece of wire that is inserted in the plasma and biased to a known potential. The wire draws a current from the plasma whose magnitude and polarity depend on the potential applied to the probe. By sweeping the voltage over a wide range, one obtains a relation between current and voltage that contains information about the bulk plasma. This technique, and the analysis that follows, was developed by Mott-Smith and Langmuir in 1926 [63]. The design of the probe and the electronics controlling it will be described in Section 4.4. A typical Langmuir probe curve is shown in Figure 3.5.

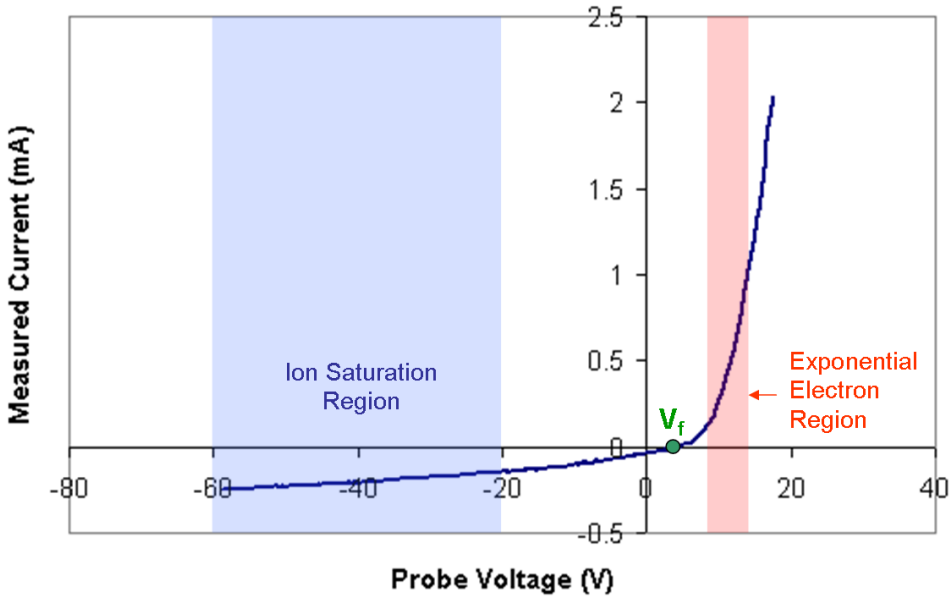

Figure 3.5: Current-voltage relation produced by the single-electrode Langmuir probe. The ion saturation region, shown in blue, is where the probe potential V_0 is sufficiently negative (relative to the bulk plasma) that a steady-state Child-Langmuir sheath forms around it, and only ions flow into the probe surface. As the potential is made more positive, the electron density in the sheath increases to the point where the electron current becomes larger than the ion current; this is called the exponential electron region and is shown in red. The point where the ion and electron current are exactly equal is the floating potential, V_f.

It should be noted at this point that the potential V_0 applied to the probe is very small compared with the magnitude of the PII implant pulses, and the probe sweeping frequency is very slow compared to the pulse frequency. This means that the contribution of the Matrix sheath may be neglected. Also, for the analysis in this section, zero potential is defined as the potential at the chamber wall, not the plasma itself (as it was in Section 3.2.2). Therefore, the potential of the plasma relative to the wall (the plasma potential V_p) is an unknown quantity that must be measured. Any term V that appears in Section 3.2.2 should be replaced with the potential difference $V - V_p$ for the following discussion.

3.3.1 Plasma Potential

The plasma potential V_p can be found using the floating potential V_f shown in Figure 3.5. Asserting the equality of ion and electron currents ($I_i = I_e$) at the floating potential, one finds that [56]

$$V_f - V_p = \frac{T_e}{2e} \ln\left(2\pi \frac{m_e}{m_i}\right), \tag{3.29}$$

which can easily be solved to find V_p if the value of the electron temperature T_e is known.

3.3.2 Electron Temperature

To determine the electron temperature, one must examine the electron exponential region, marked in red in Figure 3.5. So long as the difference $V_0 - V_p$ is sufficiently negative with respect to T_e/e, the form of the electron density from Eq. 3.10 remains valid. The mean electron speed is taken to be the mean of the Maxwellian distribution:

$$v_e \approx \overline{v}_{Maxwellian} = 2\sqrt{\frac{2T_e}{\pi m_e}}, \tag{3.30}$$

which gives an expression for the electron current in terms of a collecting area A_e and the plasma parameters n_0 and T_e:

$$I_e = A_e e n_0 \sqrt{\frac{T_e}{2\pi m_e}} \exp\left(\frac{e(V_0 - V_p)}{T_e}\right). \tag{3.31}$$

With some manipulation, one finds that in the region between the floating potential and the plasma potential,

$$\frac{d}{dV_0}\left[\ln(I_{total} - I_i)\right] = \frac{e}{T_e}, \tag{3.32}$$

where I_{total} is the total current measured in the electron exponential region and I_i is the current measured in the ion saturation region. Eq. 3.32 can be solved to find the electron temperature T_e without knowledge of A_e or n_0.

3.3.3 Plasma Density

Given the value of the electron temperature, the plasma density n_0 can be extracted from the measured ion saturation current, marked in blue in Figure 3.5. In this region, one assumes the electron current to be negligible ($I_e = 0$). Evaluating Eq. 3.12 at the sheath boundary returns

$$n_0 = -\exp\left(\frac{1}{2}\right)\frac{I_i}{eA_s}\sqrt{\frac{m_i}{T_e}}, \tag{3.33}$$

where A_s is the area of the sheath boundary and the ion mass m_i becomes a weighted average M in plasmas with multiple ion species according to the formula [69]

$$\sqrt{M} = \sum_j k_j \sqrt{m_{i,j}}, \tag{3.34}$$

where $m_{i,j}$ is the mass of ion species j and k_j is the fraction of the plasma represented by that species. It is further assumed that all ions crossing the sheath boundary must ultimately be absorbed by the probe. Depending on the shape and size of the probe, it may be necessary to use the method described at the end of Section 3.2.2 to find the sheath collecting area A_s. The results of such a calculation are shown in Figure 3.6.

3.4 Fluence Prediction

Marcel Risch, a former M. Sc. student working with the PII apparatus, developed a computer program in ANSI C capable of modeling various aspects of the PII process, such as the fluence into the target, the ion energy distribution at the target surface, and the position of the plasma sheath surrounding the implantation target as a function of time. The program (called p2i) is based on the Lieberman model [55, 56] and is a refinement on earlier work by J. T. Steenkamp [70]. Presented below is a very brief overview of the model; more details concerning its implementation may be found in Marcel Risch's M. Sc. thesis [54].

The Lieberman model assumes that the current into the target is composed of two parts: the Bohm current due to ions entering the sheath with speed v_B, as

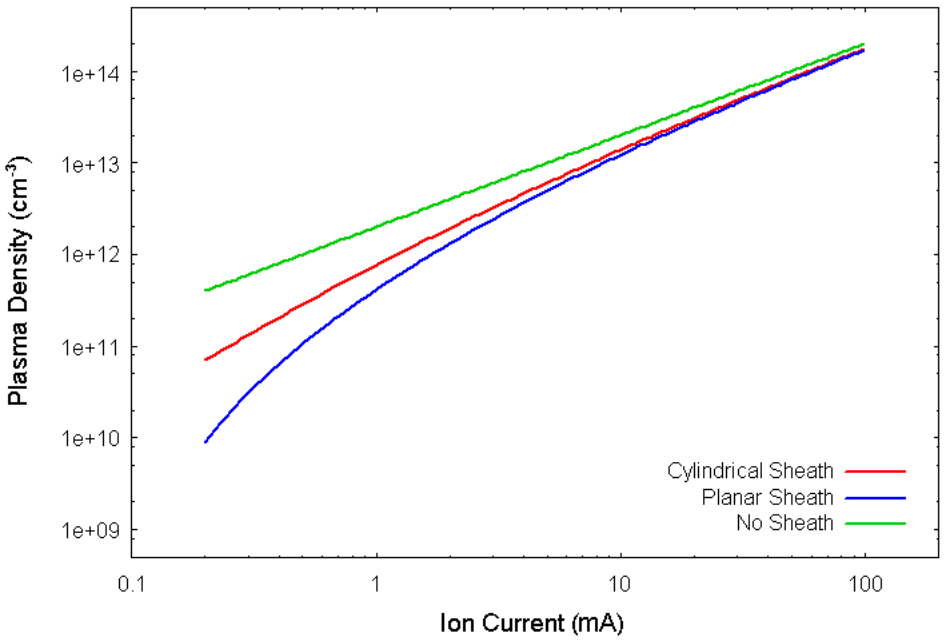

Figure 3.6: The density of a hydrogen plasma as determined from the measured ion current and computed electron temperature. The cylindrical result (red) was calculated via the RK4 method, while the planar-approximated density (blue) was found using an analytical solution. The density was also calculated assuming a sheath width of zero, for comparison (green). The parameters of the calculation were: $T_e = 3$ eV, $V_0 = -50$ V, and a cylindrical probe of radius 0.75 mm and length 8.5 mm.

defined by Eq. 3.21; and the motion of the sheath edge r_s, which uncovers new ions as it passes and sends them toward the target. The combined equation is

$$J = en_i(V_0, t)\left(v_B + \frac{d}{dt}r_s(V_0, t)\right), \tag{3.35}$$

where V_0 is the highly negative pulsed potential being applied to the target. The model further assumes that the current can be described by the Child-Langmuir law from Eq. 3.4 at all times; equating the two expressions returns

$$\frac{d}{dt}r_s(V_0, t) = \frac{-4}{9}\frac{\epsilon_0}{en_i(V_0, t)}\sqrt{\frac{2e}{m_i}}\frac{V_0^{\frac{3}{2}}}{r_s(V_0, t)^2}. \tag{3.36}$$

This differential equation is solved using the RK4 method to find the sheath width as a function of time, which can be inserted back into Eq. 3.4 to calculate the ion current.

3.5 Depth and Damage Profiles

In any ion implantation process, the ions entering the target lose their energy through collisions with electrons and atomic nuclei in the target. This process leaves a depth distribution (hereafter called the *depth profile*) that is roughly Gaussian in nature. By convention, the mean of the distribution is called the *range*, and its deviation is the *straggle*. These quantities depend on the mass of the implanted ion and the energy imparted to it by the high-voltage pulse. Heat-activated diffusion during and after implantation likely changes the profile as well. The depth profile reflects the amount of material in the target crystal that can be chemically affected by the implanted element; therefore, if effects such as hydrogen passivation are relevant to the observed luminescence, one would expect a correlation between the depth profile and the measured EL.

As the implanted particles pass through the crystal target and collide with atoms in the lattice, they create a distribution of vacancies and dislocations, hereafter called the *damage profile*. One expects that crystals with more vacancies and dislocations should be more likely to form voids of the type that may cause confinement-related luminescence; if this is the case, a correlation should be observed between the damage profile and the observed EL. For a detailed treatment of ion-solid interactions, the reader is directed to the *Handbook of Plasma Immersion Ion Implantation and Deposition* [62].

TRIM (Transport of Ions in Matter) is a computer model originally developed by J. F. Ziegler and J. P. Biersack that simulates the stopping of energetic ions within crystalline targets. The TRIM model is included in the SRIM (Stopping and Range of Ions in Matter) package available at www.srim.org. Details of the physical model used by Ziegler et al. to implement TRIM can be found in Ref. [71]. TRIM can be used to calculate the depth and damage profiles for hydrogen, helium, and deuterium implantation into silicon targets. However, TRIM assumes the target is at absolute zero, so neither diffusion nor self-annealing effects are included in the results. To account for self-annealing of the crystal during implantation at or near room

temperature, the authors of TRIM suggest that the final displacement concentration should be taken as 1% of the calculated value. One expects that diffusion during and after implantation should broaden the depth profile considerably, and desorption from the body of the target is expected to substantially reduce the concentration of implanted element within the crystal.

Chapter 4

Device Fabrication

The method of fabricating electroluminescent silicon diodes used in this work requires several pieces of equipment: a vacuum chamber with attached gas flow controllers, an inductively coupled plasma (ICP) generator, a Langmuir probe, a high-voltage pulse modulator, and an annealing furnace. The light emitted from each finished device was measured with a spectrometer. This section describes of each of these items and provides an overview of the whole device fabrication procedure, as summarized in Table 4.1. A schematic representation of a finished ion implanted silicon device is shown in Figure 4.1.

Table 4.1: Device fabrication procedure

Procedure Step	Equipment	Section
1. Load silicon into vacuum chamber	Vacuum system	4.2
2. Pump down to base pressure		
3. Flow in feedstock gas		
4. Initiate the plasma discharge	ICP Plasma Source	4.3
5. Measure n_0 and T_e from plasma	Langmuir Probe	4.4
6. Implant ions into silicon	Marx generator	4.5
7. Anneal silicon sample(s)	Tube furnace	4.7
8. Apply metal contacts	Evaporator	4.8
9. Anneal at 400°C	Tube furnace	4.7
10. Perform spectroscopic analysis	Spectrometer	4.9

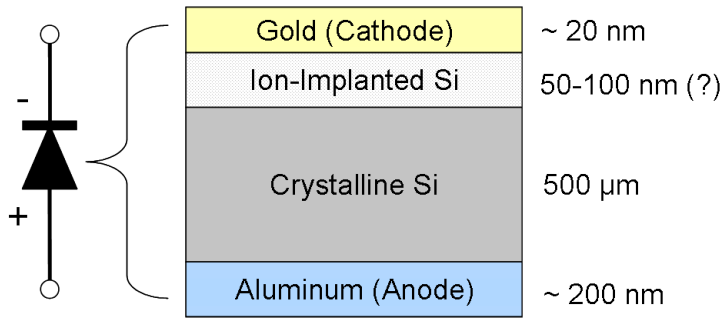

Figure 4.1: The internal structure of a finished ion-implanted silicon diode. There is a thin layer of silicon oxide (SiO_2) between the implanted silicon and gold layers that is not shown in this schematic. The thickness of the ion-implanted layer depends on the ion mass and implantation energy used. TRIM calculations suggest that a typical penetration depth for 5 keV hydrogen or helium ions is 50 to 100 nm; the final depth profile must also depend on annealing and diffusion effects.

4.1 Silicon Wafers

The silicon wafers used in this research were purchased from NOVA Electronic Materials, Inc. They are 500 μm thick, boron-doped, p-type, CZ-grown wafers whose resistivity is in the range of 5 to 25 Ω·cm. The dopant concentration is in the range of 5 to 20 $\times 10^{14}$ cm^{-3}.

4.2 Vacuum System

Figures 4.2 and 4.3 show the vacuum system used in the present plasma ion implantation experiments. The plasma implantation chamber itself is a cylinder with an interior volume of approximately 42 L that is connected to two pumps. The turbomolecular pump, used to pump the chamber down to a base pressure around 1 μTorr, is a 300 L/s Varian TV301 Navigator equipped with water cooling tubes to maintain optimal working temperature. The mechanical forepump backing the turbo is an Adixen Pascal 2010 SD series rotary vane pump that works at 2.5 L/s and can maintain gas pressure as low as 1 mTorr. The mechanical pump is lubricated

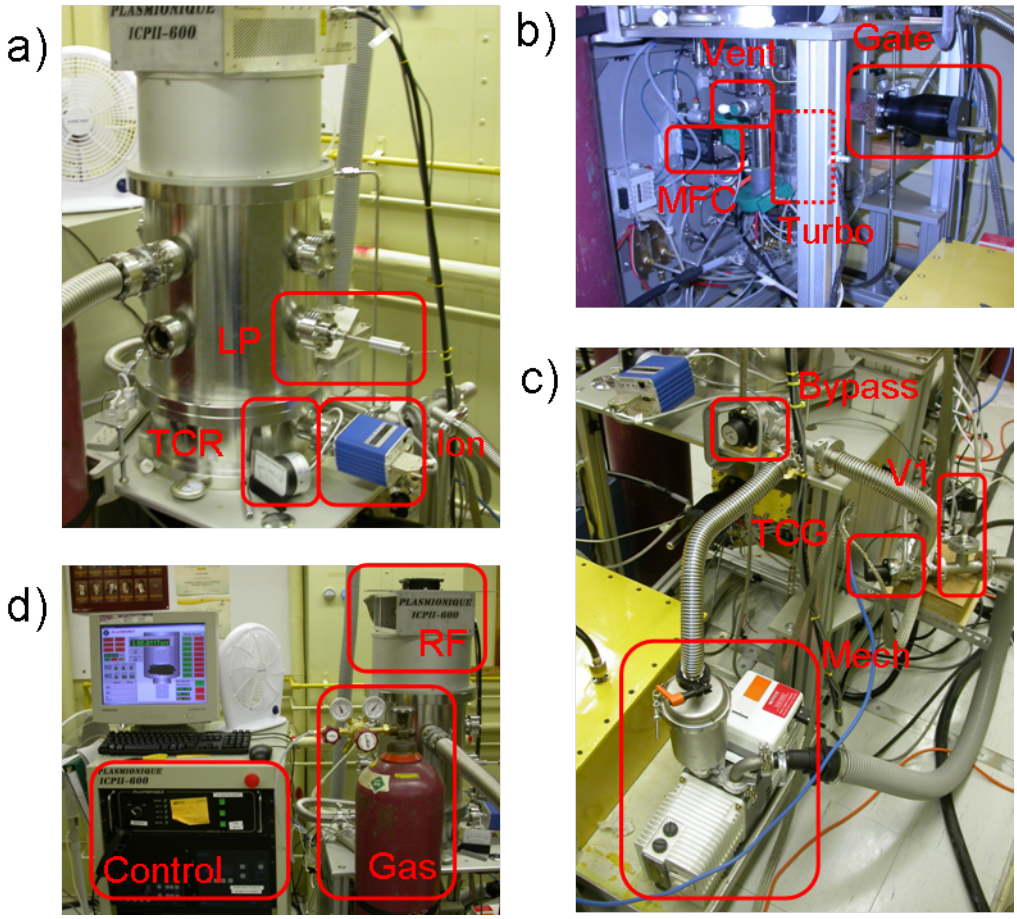

Figure 4.2: The vacuum system used for the present plasma ion implantation research. Frame (a) shows the vacuum chamber itself, along with the Langmuir probe (LP), thermocouple gauge readout (TCR), and Micro-Ion Plus combination gauge (Ion). Frame (b) shows the underside of the chamber, including the vent valve (Vent), mass flow controller (MFC), manual gate valve (Gate), and turbomolecular pump (Turbo, obscured). Frame (c) shows the pumping system in the rear of the chamber, including the bypass valve (Bypass), pneumatic valve (V1), thermocouple gauge (TCG), and mechanical roughing pump (Mech). Finally, frame (d) shows the control system for the chamber and pumps (Control), the RF power supply (RF), and the feed gas bottle and regulator (Gas).

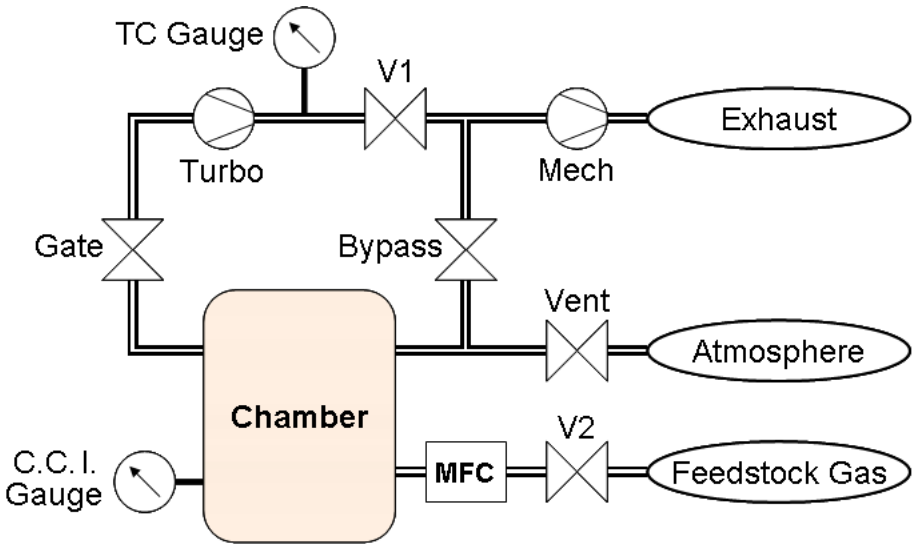

Figure 4.3: A schematic of the vacuum system shown in Figure 4.2. The pneumatic valve (V1) and manual gate valve (Gate) are the main evacuation channel for the two pumps (Turbo, Mech) during normal operation. A thermocouple (TC) gauge measures the pressure in the foreline, and a cold-cathode ionization (C.C.I.) gauge measures the pressure inside the chamber. The ion gauge assembly also incorporates a Pirani gauge and thermocouple gauge in order to measure a wider range of gas pressures. Feed gases (hydrogen, helium, deuterium) are delivered through a computer-controlled pneumatic valve (V2) and the gas flow is regulated by a mass flow controller (MFC). To recompress the chamber, all valves are closed and the vent valve (Vent) is opened to allow atmosphere back into the chamber. To change samples quickly, the turbomolecular pump may be kept running, isolated under vacuum by closing the Gate and V1 valves, while the chamber is opened. After the chamber is closed again, the mechanical pump evacuates the chamber through the bypass valve (Bypass) before the turbo is reconnected to the system.

with inert Fomblin oil (for safety) and equipped with a mist trap and anti-suckback valve to prevent rapid recompression in the event of power failure. In the standard pumpdown procedure, the two pumps continuously evacuate the chamber through the Gate and V1 (pneumatic) valves, and all other valves remain closed.

The flow of feedstock gases (H_2, D_2, or He) into the chamber is activated by a pneumatic valve (V2 from Figure 4.3) and the flow rate is regulated by a mass flow controller. A flow rate of 10 to 15 standard cubic centimetres per minute (sccm) is typically used. After the gas valve is opened, the gas pressure is controlled by partially closing the gate valve to reduce the rate at which gas can be pumped out of the chamber. A Micro-Ion Plus combination gauge (including Pirani, thermocouple, and cold-cathode ionization gauges) measures the pressure inside the chamber at all times.

4.3 Plasma Source

Inductively coupled plasma (ICP) sources consist of a conducting coil placed in close proximity to a gas-filled chamber, with a dielectric (glass or quartz) window separating the two. Radio-frequency (RF) power applied to the coil induces RF electric fields within the chamber; these fields accelerate free electrons, and the hot electrons partially ionize the gas and thereby sustain a plasma discharge [62]. A dynamic balance is established within the chamber as ions are generated by this process and lost to collisions with the chamber wall, but an ICP does not reach thermal equilibrium.

The system used in this work employs a Seren R601 RF power supply operating at 13.56 MHz that can deliver up to 600 W to the plasma. Its antenna is a flat spiral conductor positioned above a quartz window that serves as the ceiling of the vacuum chamber. To maximize the power transfer efficiency from the RF generator to the plasma, it is connected to a matching network of two variable capacitors whose values are varied (manually or automatically) until the impedance of the load (plasma plus capacitors) is as close as possible to the output impedance of the generator. Power

transfer efficiencies in excess of 90% can be achieved in this manner.

The plasma density and temperature of an ICP is determined by the combination of gas pressure within the chamber and RF power delivered to it. Figure 4.4 shows the relationship between these parameters as measured by the Langmuir probe in a hydrogen plasma. To save time during the implantation stage, one generally desires a high-density plasma, so higher values of RF power and gas pressure are preferred. The only factors limiting these parameters are practical ones: excessive RF power can overheat the generator if matching is poor or unstable, and given that the gas pressure is controlled via the manual gate valve, it is difficult to maintain a stable pressure above 15 mTorr.

Another important parameter in the ICP is the relative population of each ion species in the plasma. The fluence prediction model discussed in Section 3.4 assumes that polyatomic ions break apart into their constituent atoms upon impact with the target surface, and each atom receives an equal fraction of the total kinetic energy. Therefore, a plasma consisting mostly of H_2^+ ions will have a shallower depth profile than one consisting solely of H^+ ions. Unfortunately, applicable data regarding relative populations in hydrogen ICPs are scarce, and an ion-mass spectrometer (not available for this work) would be required to perform the measurement *in situ*. The numbers presented in Table 4.2 are estimates based on measurements of capacitively coupled [72] and glow discharge [73] plasmas with working pressures on the order of 10 mTorr. No data have been found regarding relative species populations in low temperature deuterium plasmas, so they were assumed to be identical to the values for hydrogen. Helium does not form molecules, so it is assumed that only singly charged monoatomic ions are present in helium plasmas.

4.4 Langmuir Probe

The Langmuir probe used in the present experiments is a simple, single-tip probe consisting of a tungsten wire sheathed in an alumina tube and surrounded by a grounded stainless steel shell. The part of the wire exposed to the plasma is a cylin-

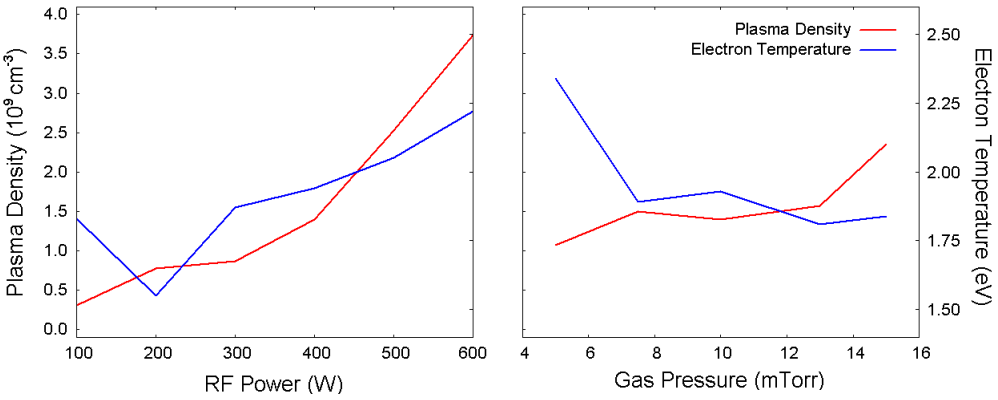

Figure 4.4: The density and temperature of an inductively coupled hydrogen plasma as a function of (a) applied RF power and (b) neutral gas pressure. Plasma parameters were measured using the Langmuir probe described in Section 4.4. The gas pressure used while varying RF power was 10 mTorr, and the RF power applied while varying gas pressure was 400 W.

Table 4.2: Relative ion species populations, after [72, 73]

Plasma	Species	% of Total Ions
Hydrogen	H^+	10
	H_2^+	60
	H_3^+	30
Deuterium	D^+	10
	D_2^+	60
	D_3^+	30
Helium	He^+	100

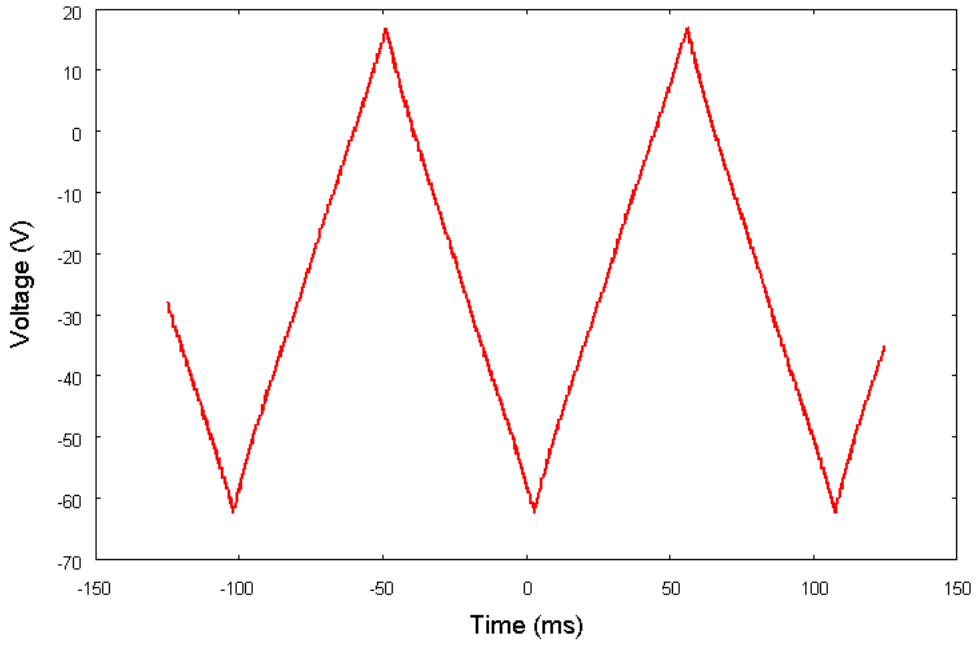

Figure 4.5: The sweeping voltage generated for the Langmuir probe by custom electronics described in Appendix B, as measured by a Tektronix TD2000B digital oscilloscope.

der 8.6 mm long with a radius of 0.75 mm. No provisions are currently in place to eliminate RF interference from the probe readings, though this does not appear to significantly degrade the probe's performance. Tuszewski and Tobin estimate that the error in calculated plasma parameters from this simple probe setup is approximately 10% [74].

To perform the analysis described in Section 3.3, electronics capable of generating a linear voltage sweep over the range of -60V to +30V, and sourcing enough current to probe the exponential electron region, were designed and built. The circuit was made manually adjustable to allow the user to compensate for varying plasma parameters, so the equipment can consistently probe the relevant portion of the current-to-voltage curve. The instrument can be seen in Figure 4.6, an example of its output is shown in Figure 4.5, and the electronics are described in more detail in Appendix B.

4.5 Solid State Marx Generator

To carry out medium-energy plasma ion implantation, one requires a voltage supply capable of delivering 5 to 20 kV negative-polarity pulses to the silicon target within the vacuum chamber. The present work employs a solid-state Marx generator developed by J.T. Steenkamp for this purpose [70, 75]. A schematic representation of a two-stage generator is shown in Figure 4.6, and a brief description of how it operates is presented below.

Each stage of the Marx generator can operate in two modes, called *charge* and *discharge*. In the *charge* mode, the charging transistors (TCx in Figure 4.6) are turned on - the collector-emitter paths are conducting - and the discharging transistors (TDx) are off. This causes current from the DC supply to flow in parallel into the capacitors (Cx) until each one is charged to the full DC potential V_{DC}. When the two transistors are switched, so TC is off and TD is on, the capacitors become linked in series to the output terminal V_{out}; their potentials combine additively to produce an output voltage equal to

$$V_{out} = n \cdot V_{DC}, \tag{4.1}$$

where n is the number of stages in the Marx generator. Provided that the capacitors are not allowed to discharge for too long, the output of the device is a nearly flat pulse with a very small linear droop. To reduce the number of required stages, the output of the Marx generator is fed into a Westinghouse 610J647H01 pulse transformer. The transformer steps up the pulse voltage by a factor of ten, though the transformer slows the pulses' rise time from 100 ns to approximately 1 μs. Examples of the pulses produced by this equipment are shown in Figure 4.7.

4.5.1 Digital Signal Pulse Generator

To deliver the correct number of signal pulses to the transistors TCx and TDx in Figure 4.6, a digital pulse generator was built around a programmable PIC18F4520 microcontroller. The unit includes six buttons and is connected to an LCD unit for

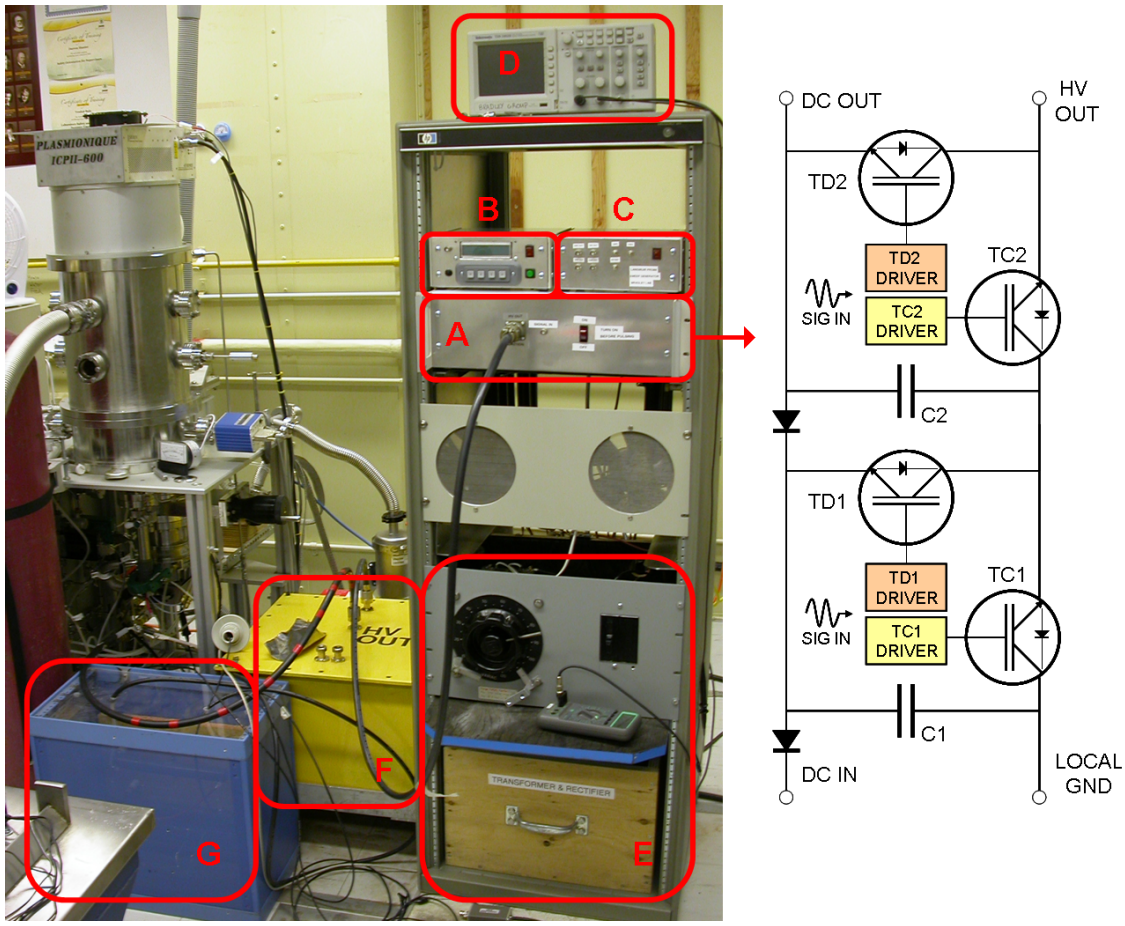

Figure 4.6: The custom electronics used to perform the present PII experiments. The digital pulse generator (B) drives the gates of the transistors within the Marx generator (A) with an optically isolated signal (SIG IN). The Marx generator takes power from the custom DC power supply (E to DC-IN) to produce high-voltage pulses that are sent to the primary coil of the Westinghouse 610J647H01 pulse transformer (HV-OUT to F). The secondary coil of the transformer is connected to the sample holder within the vacuum chamber. A shunt resistor (G) is placed between the transformer secondary and ground to allow charge on the sample holder to safely dissipate and to dampen parasitic oscillations in the HV pulses. The Langmuir probe electronics (C) are used to measure plasma properties prior to implantation. Both Langmuir probe and Marx generator have their output measured by the Tektronix TD2000B digital oscilloscope (D).

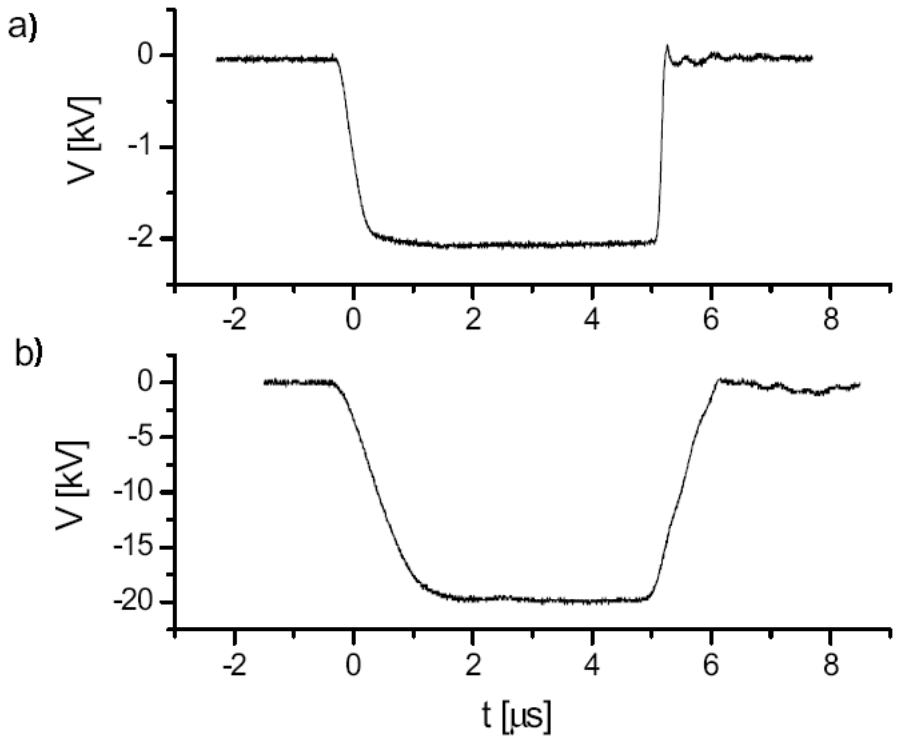

Figure 4.7: 20 kV pulses produced by a two-stage Marx generator with a plasma load, as recorded by the Tektronix TD2000B oscilloscope. Graph (a) is the voltage on the primary (input) coil of the Westinghouse pulse transformer (HV-OUT from Figure 4.6), whereas (b) shows the voltage on the secondary coil. Taken from [70].

the display of feedback and prompts. The pulse generator allows the user to precisely control the number, duration, and frequency of high voltage pulses delivered to the ion implantation target. A flowchart that illustrates the operation of this equipment is presented in Appendix B.1.

4.5.2 Sample Holder

The output of the Marx generator and pulse transformer is sent through a quartz-insulated feedthrough to a sample holder within the vacuum chamber. The sample holder is a circular stainless-steel plate equipped with mounting screws for securing silicon wafers to its surface. The assembly is equipped with water cooling tubes to minimize heating during implantation.

Sample Heating

During ion implantation, a large flux of energetic ions is bombarding both the silicon target and the sample holder it is mounted upon; this influx of energy must heat both target and holder to some degree. The analysis begins with a few assumptions:

1. The thermal conductivity within the target material is high,
2. No heat is lost from the material by radiation or conduction, and
3. Ion kinetic energy is completely converted to heat upon implantation.

These assumptions will give a worst-case estimate of the temperature rise in the implantation target. The energy Q gained by an object subject to ion bombardment should be

$$Q = A \cdot F \cdot U, \tag{4.2}$$

where A is the area of the target exposed to plasma, F is the total ion flux incident upon the exposed surface, and U is the average kinetic energy per incident ion. The specific heat capacity of the material is used to find the change in its temperature:

$$Q = c_m m \Delta T, \tag{4.3}$$

where c_m is the specific heat capacity per unit mass, m is the mass of material being implanted, and ΔT is the temperature change in degrees Kelvin. Equating 4.2 and 4.3 produces an expression for the increase in temperature,

$$\Delta T = \frac{A \cdot F \cdot U}{c_m m}. \tag{4.4}$$

For a 4 in. diameter silicon wafer being delivered a flux of 1×10^{16} ions/cm^2 with an average energy of 5 keV each, the temperature increase ΔT is 96.5 K. This is a worst-case heating estimate for the implanted silicon wafer; some thermal contact with the water-cooled sample holder should reduce ΔT. The highest fluence used in the present research was 2.5×10^{17} ions/cm^2, which would result in a worst-case

temperature rise of 2412 K. As the melting point for silicon is 1687 K, and the samples did not melt in the ICP chamber, one must conclude that the cooling apparatus succeeded in carrying much of the excess heat away from the silicon targets. Unfortunately, no equipment is presently in place to measure the actual temperature reached by the implantation target during the PII process. Regardless, the worst-case temperature increase for most PII processing was lower than any temperature used to anneal the finished devices, and so sample heating during implantation is not expected to be significant except in a small number of extreme cases.

Surface Charging

Marcel Risch investigated the effect of surface charging of the implantation target on the effective pulse voltage in his M.Sc. thesis, basing his analysis on the work of Emmert [76]. The main results are reproduced in Figure 4.8. The silicon wafers are no more than 0.500 mm thick, which means that the potential difference between the ideal approximation and the actual potential will be no more than 10%. This result suggests that surface charging effects should be negligible in the present ion implantation experiments.

4.6 QtPlasmaConsole Software

To facilitate reliable, repeatable ion implantation experiments using the Marx generator, a program called QtPlasmaConsole was made to incorporate the p2i fluence prediction code, the Langmuir probe analysis algorithm, and the results of several TRIM simulations into a single package. The software allows the user to modify experimental parameters, such as the dimensions of the Langmuir probe or the relative concentrations of ion species, without manually rewriting the text files used to store this information. It is coded in C++ and uses the Qt package (available at qt.nokia.com) to create a user-friendly interface and a plotting window for viewing results.

The main QtPlasmaConsole interface window is shown in Appendix B.3 as Figure

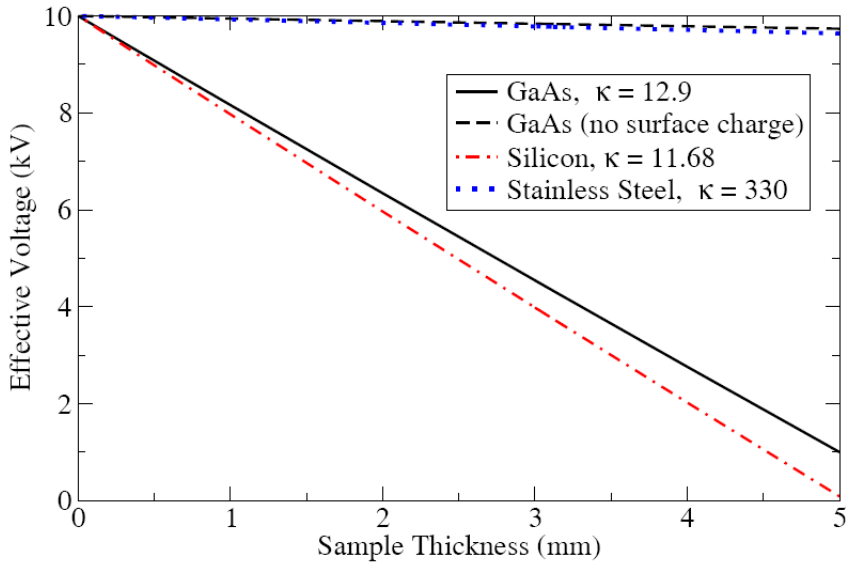

Figure 4.8: The effective electric potential on the surface of a dielectric as a function of dielectric thickness. The data shown is for a 10 kV implantation pulse and does not account for electrical contact between the dielectric and the conducting sample holder, which would allow excess charge on the dielectric to dissipate over time. Taken from [54].

B.4. The application requires two files as input for a calculation: one containing the voltage and current information retrieved from the Langmuir probe, and another containing the high-voltage pulse waveform recorded from the Marx generator. The program executes its analysis of the PII experiment in three stages, shown in Table 4.3.

More information on each of these steps is available in Chapter 3: Section 3.3 explains the analysis of probe data, Section 3.4 describes the fluence prediction model, and Section 3.5 discusses TRIM simulations.

4.7 Annealing Furnace

After implantation, the silicon samples are thermally annealed in a Barnstead Thermolyne 21100 tube furnace, shown in Figure 4.9. To avoid excessive oxide formation on the surface of the silicon, the tube is attached to a port on the vacuum chamber

Table 4.3: QtPlasmaConsole algorithm for PII analysis

Step	Inputs	Outputs
1. Langmuir probe analysis	Probe data	Plasma density
		Plasma temperature
		Plasma potential
2. Ion fluence prediction	HV pulse data	Implanted ion fluence
	Output from (1)	Ion energy distribution
3. Depth and damage profiles	Energy distribution	Depth profile
	Output from (1)	Vacancy concentration
	Saved TRIM results	

and the pumping system described in Section 4.2 is used to evacuate the furnace prior to annealing. The chamber is used for this purpose because the laboratory lacks a second set of pumps to dedicate to use with the furnace. The pressure inside the tube during annealing is typically around 200 μTorr; this is much higher than ordinary working pressures inside the vacuum chamber due to the length of the connecting hose and leakage from the tube-hose interface.

Samples are annealed in two stages. After implantation, and prior to metallization (described in Section 4.8) the samples are annealed at a temperature chosen by the researcher that varies from device to device as part of the experiment. The annealing temperature at this stage is typically between 400°C and 800°C, and the time spent at this temperature is about 60 minutes. After the metal contacts are attached to the silicon (see Section 4.8), a second heat treatment is applied: the sample is heated to 400°C for another 60 minutes to improve the quality of the electrical contact between the silicon and the metals. This second stage will henceforth be referred to as *contact firing*. Using higher temperatures during the contact firing stage ruins the electrical characteristics of the device, and no luminescence was observed in such cases.

A typical heating curve for the furnace is shown in Figure 4.10. Here, one observes the main drawback of using this type of furnace: the time required for the furnace

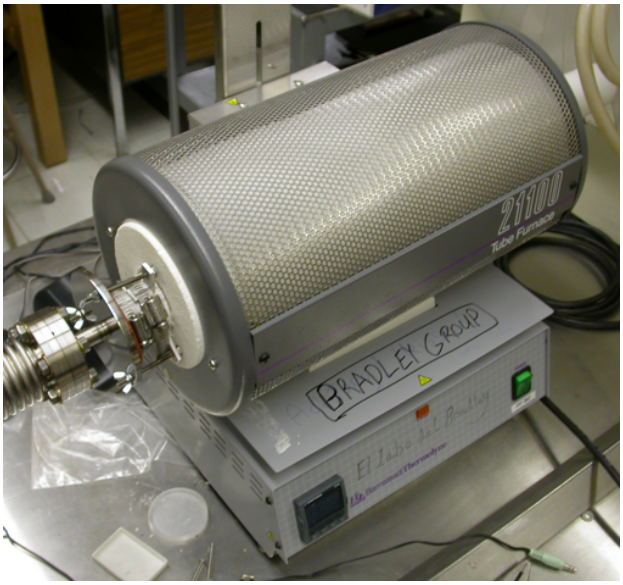

Figure 4.9: The Thermolyne 21100 tube furnace used in the present research. The metal hose attached to the left side of the tube connects to the front of the vacuum chamber to allow the tube to be evacuated during the annealing process.

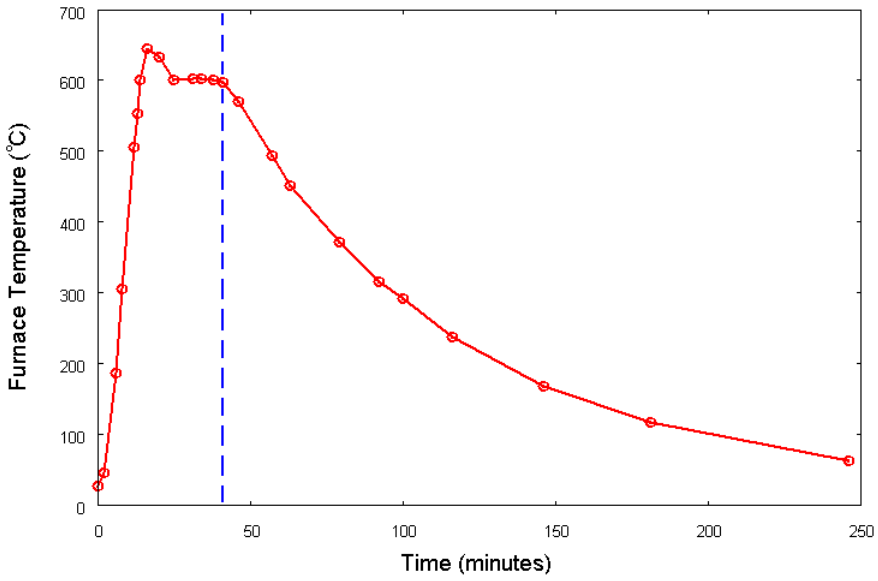

Figure 4.10: The temperature within the tube furnace as a function of time. The temperature was set to 600°C and the pressure within the furnace was pumped down to 1.5×10^{-4} Torr before the furnace was activated. The dashed blue line indicates the time when the furnace was turned off.

to cool down is very lengthy, which means that the annealing time is not well-controlled. Removing samples from the furnace during this process was not desirable, as it would require breaking vacuum and exposing the hot samples to oxygen. More precise annealing work with better-controlled heating and cooling rates must be left to future researchers on this project.

4.8 Metal Evaporator

To produce useable electroluminescent devices, metal contacts were attached to each side of the silicon sample: 150 to 200 nm of aluminum on the unpolished, unimplanted sides formed Ohmic contacts, and roughly 20 nm of gold was deposited on the polished, implanted sides to form Schottky junctions. Although the thinness of the gold layer made the devices very fragile, it was necessary in order to allow light generated within the implanted silicon to pass outside the device. The transparency of the gold layer will be addressed in Section 4.9.2.

The metal deposition was accomplished using an evaporator that was made available by Prof. Stephen Urquhart from the Dept. of Chemistry at the University of Saskatchewan. The evaporator heats the desired metal to its melting point by driving a large electric current through the tungsten boat in which the metal was placed; the vaporized metal deposits itself on the samples, which are suspended directly above it within an evacuated chamber. The deposition rate and thickness are monitored by a Sigma Instruments SQM-160 quartz microbalance system.

4.9 Apparatus for Spectrometry

Figure 4.11 shows the spectrometer, camera, and custom sample holder used to measure light emission from the silicon devices. Power was provided to the devices by a LAMBDA LG-251 20V regulated power supply, with the gold contact serving as the anode. Water cooling was necessary during operation because a large current (in excess of 1.0 A) was required to drive measurable EL in the devices.

The spectrometer in Figure 4.11 is a SpectraPro 300i from Acton Research that was provided by Prof. Chijin Xiao from the Dept. of Physics and Engineering Physics. The spectrometer is equipped with a 1200 lines/mm grating with a 500 nm blaze and is connected to a Princeton Instruments PI-MAX intensified CCD camera for light measurement. Other gratings are also available but were not used in the present research. Both spectrometer and camera are controlled by computer via the WinSpec software package. Typical operating parameters for the spectrometer are listed in Table 4.4.

Table 4.4: SpectraPro 300i and PI-MAX operating parameters

Parameter	Typical Value	Notes
Grating density	1200 grooves/mm	Grating no. 3
Grating blaze	500 nm	Grating no. 3
Exposure time	60 s	Photometry mode
(typical)	240 s	Spectroscopy mode
Camera gain	128 (no units)	Recommended by manual
Cosmic ray removal	Spatial, 50%	Recommended by manual
Dark signal removal	None	See Section 4.9.2

4.9.1 Calibration for Quantum Efficiency

In addition to performing spectrometry, the spectrometer can operate in a reflective mode where all light is focused on the camera rather than being dispersed by the grating. This mode was used to perform photometry on the finished devices. To calibrate the photometry measurements and obtain a reasonable estimate of the each device's external quantum efficiency η_x, the photometry mode was used to measure the light output of a commercial red LED whose total light output is given in its datasheet. The number of photons that could be expected to reach the detector was calculated, and the conversion factor between photons incident on the spectrometer and recorded CCD counts was extracted from that value. Following this, the

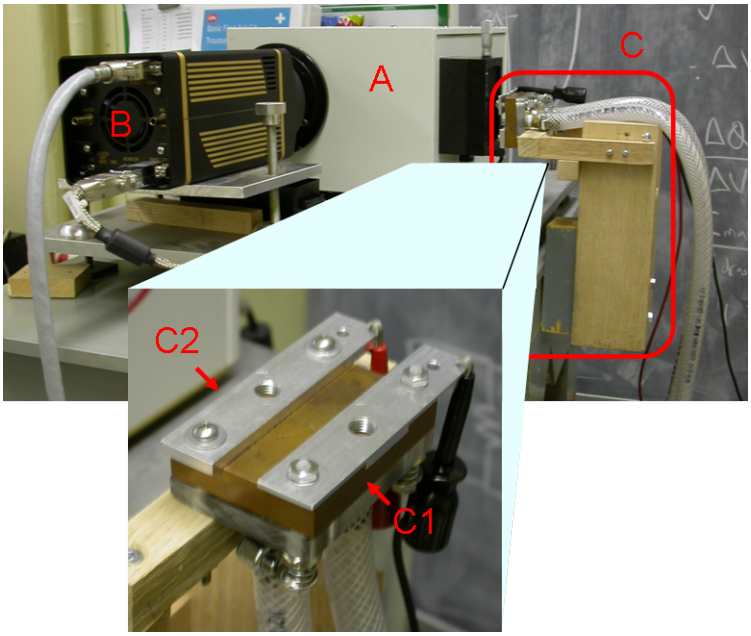

Figure 4.11: The apparatus used to perform spectrometry on finished electroluminescent silicon diodes. The Acton Research SpectraPro 300i spectrometer (A) is connected to a PI-MAX camera (B) for light detection. Silicon devices are loaded into the sample holder (C) and secured beneath a spring-loaded aluminum bar (C1) which serves as the device's anode. The other bar (C2) is secured to the copper platform and used as the cathode. The wooden frame can be locked in place during long measurements to ensure stable light transmission into the entrance slit of the spectrometer. The entire assembly is water-cooled via the attached tubes.

relationship between the measured intensity from a silicon LED and its external quantum efficiency was determined. The full calculation is shown in Appendix A; the final result is

$$\eta_x = \frac{N_{CT}}{\beta} \cdot \frac{2\pi L^2 A_D}{A_{slit}^2} \cdot \frac{e}{I_D}, \tag{4.5}$$

where N_{CT} is the total recorded CCD counts per second from the EL-silicon device, β is the detector efficiency in counts/photon, L is the distance between the device and the spectrometer entrance slit, A_D is the total surface area of the device, A_{slit} is the area of the spectrometer's entrance slit, and I_D is the electric current being driven through the device. For the present experiments, β is 0.0093 counts/photon, L is 25 mm, and A_{slit} is 4 mm^2. Inserting these values into Eq. 4.5 returns

$$\eta_x = 4.23 \times 10^{-9} \frac{N_{CT} A_D}{I_D}, \tag{4.6}$$

which gives the external quantum efficiency η_x in terms of the measured EL intensity, the device area, and the drive current.

4.9.2 SpectralAnalyzer Software

A program called SpectralAnalyzer was designed and implemented to aid in the plotting and analysis of photometric and spectroscopic data. Its main interface is shown and described in Appendix B.3. Like QtPlasmaConsole, SpectralAnalyzer is coded in C++ and uses the Qt utilities to create its graphical components. The program performs several important functions: it

1. Reads and plots data from WinSpec .SPE format files;
2. Automatically removes the dark current from measured data;
3. Corrects the measured data to account for light absorption in the gold contact;
4. Allows manual plotting and fitting of up to five Gaussian functions;
5. Computes and displays the integrated intensity of the plotted spectrum; and

6. Saves the data and the Gaussian fitting parameters in a GNUPLOT-compatible format.

Use of this program is significantly more efficient than manually manipulating data with standard software such as Microsoft Excel or MATLAB. The implementation of several functions is described in more detail below.

Dark Signal Removal

Although WinSpec provides its own background and dark-current removal tools, it requires that a separate dark spectrum be taken for each recorded image; given that a full spectrum requires up to 34 images to complete, this is highly time-consuming. SpectralAnalyzer provides a means of removing such signals post-measurement. Figure 4.12 shows the image seen by the camera when the spectrometer is illuminated by a broadband source. The bright zone in the lower two-thirds of the image is the portion of the camera illuminated by the entrance slit of the spectrometer; the remainder of the CCD array is cut off from the incident light. To remove the background signal, SpectralAnalyzer averages the data in this region and subtracts the result from each point in the illuminated region.

Gold and Silicon Overlayers

Any light emitted from within the silicon itself must pass through the gold conductor, and possibly through the uppermost layers of silicon, to escape from the device and be detected by the camera. Neither gold nor silicon has a flat absorption profile in the visible wavelengths, so the measured spectrum is distorted compared to the originally emitted light. SpectralAnalyzer compensates for this using the extinction coefficient for gold measured by Johnson and Christy [77] and an optical model for silicon developed by Geist [78]. Each model gives values for the extinction coefficient α of the material, defined as an exponential factor relating the transmitted optical power P_T through a barrier of thickness d to the power incident on the barrier P_I,

as in

$$P_T = P_I \exp\left(-\alpha d\right). \tag{4.7}$$

The extinction coefficients of gold and silicon are shown in Figure 4.13. Because the depth of the luminescent centres within the devices are not known, the silicon absorption profile is not directly applied to the measurements; instead, it is used to rule out certain possibilities, such as the detection of short-wavelength (blue or blue-green) emitters from deep within the silicon devices.

Gaussian Fitting

Some analysis of spectral data, notably that found in Section 2.3, was performed by fitting the spectrum to a multi-Gaussian function to investigate the correlation between spectral shape and ion implantation parameters. SpectralAnalyzer facilitates this analysis by plotting up to five Gaussians alongside the corrected spectroscopic data. It also computes the reduced χ^2 value for the fit, defined as

$$\chi^2 = \frac{1}{N-n} \sum_i \frac{\left(y_i - f(x_i)\right)^2}{\sigma_i^2}, \tag{4.8}$$

where N represents the number of observations (data points), n is the number of fitted parameters, (x_i, y_i) is set of recorded data with error bars of magnitude σ_i for each point, and $f(x_i)$ is the value of the fitted multi-Gaussian function at the point x_i. A χ^2 value close to 1.0 represents reasonable agreement with the data, whereas values greater or less than 1.0 suggest that the model fails to fit some features, or is fitting noise within the data, respectively. Presently, the SpectralAnalyzer program does not possess automated curve-fitting algorithms, so it is used to perform a coarse fitting by trial and error. SpectralAnalyzer saves the results in a format readable to GNUPLOT, which is used to automate the final fitting analysis using the *fit* function native to that software [79].

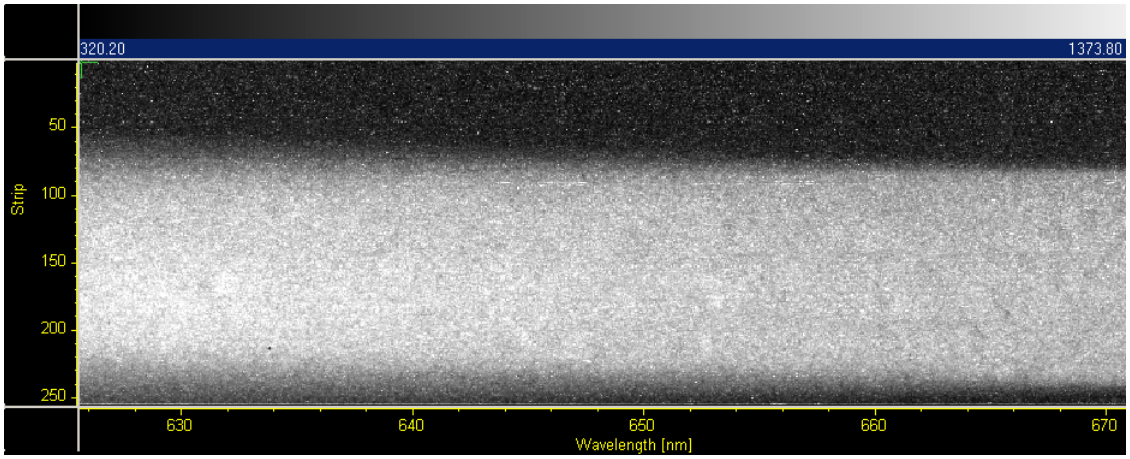

Figure 4.12: An image captured by the PI-MAX camera of a broadband light source incident on the spectrometer's entrance slit. Note that the slit only illuminates part of the camera's CCD array; the remainder of the image is be used for dark current removal.

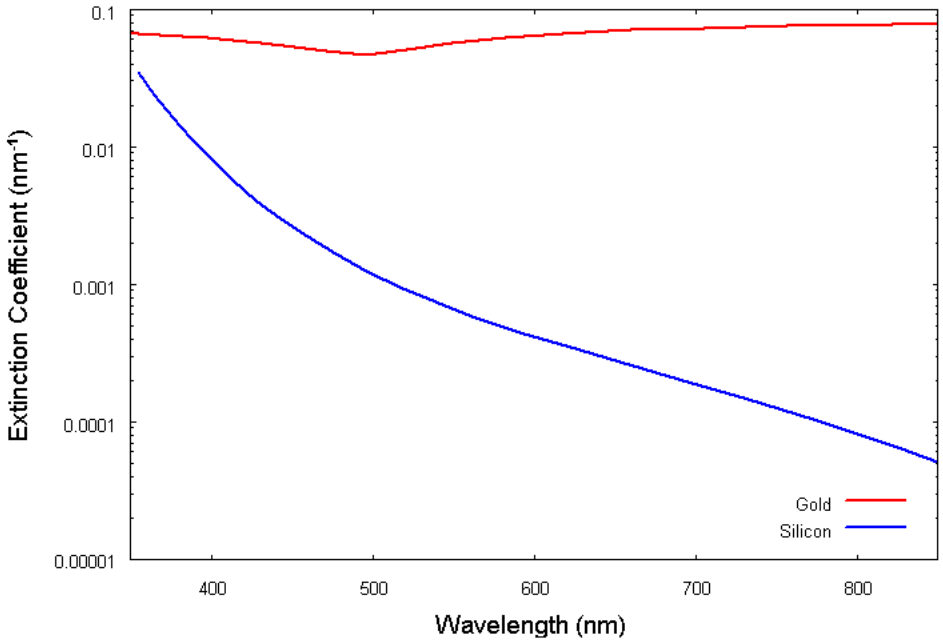

Figure 4.13: The extinction coefficients of gold and silicon in the visible range of wavelengths, in units of nm^{-1}. The thickness of the gold layer is about 20 nm for all devices. The thickness of silicon overlayers is not known.

Chapter 5

Results

Using the procedure outlined in Chapter 4, 51 ion-implanted silicon diodes were fabricated under a variety of processing conditions. Roughly half the fabricated devices were made with hydrogen-implanted silicon, with the remainder split between helium- and deuterium-implanted devices. The temperature used in the annealing phase varied from 400°C to 800°C, and several devices were not annealed at all prior to the final contact firing at 400°C. Implanted ion fluences ranged from 2×10^{15} to 2×10^{17} ions/cm^2, and the ion implantation energy was 5 keV in each experiment. A complete list of fabricated devices can be found in Tables 5.1, 5.3, and 5.2. Note that some devices have "N/A" listed as their annealing temperature, which indicates that no annealing was performed on those devices prior to contact firing. This notation will be used for the remainder of this Chapter.

The current-to-voltage relationship of each device was recorded, as well as the total electroluminescent intensity of the device as a function of forward current density. Many devices' EL spectra were also measured. These data were used to investigate a number of issues raised in Chapter 2 regarding the relationship between ion implantation and silicon electroluminescence. Specifically, this chapter will discuss the relationships between the observed luminescence and:

1. The number of ions implanted by PII,
2. Lattice damage caused by ion implantation,
3. Annealing conditions, and
4. The presence of hydrogen.

Table 5.1: List of hydrogen-implanted silicon devices. Shaded devices were electrically unreliable and are not included in the present discussion.

Device	Au Contact (nm)	Anneal Temp (°C)	Ion Fluence (cm^{-2})
HyA2	21	N/A	2.1×10^{15}
HyA3	24	600	2.1×10^{15}
HyA4	24	800	2.1×10^{15}
HyB2	21	N/A	8.6×10^{15}
HyB3	24	600	8.6×10^{15}
HyB4	24	800	8.6×10^{15}
HyC2	21	N/A	2.0×10^{16}
HyC3	24	600	2.0×10^{16}
HyC4	24	800	2.0×10^{16}
HyD2	21	N/A	4.0×10^{16}
HyD3	24	600	4.0×10^{16}
HyD4	24	800	4.0×10^{16}

Table 5.2: List of deuterium-implanted silicon devices.

Device	Au Contact (nm)	Anneal Temp (°C)	Ion Fluence (cm^{-2})
DtA1	20	600	1.0×10^{16}
DtA2	20	800	1.0×10^{16}
DtA3	20	N/A	1.0×10^{16}
DtB1	20	600	4.0×10^{16}
DtB2	20	800	4.0×10^{16}
DtB3	20	N/A	4.0×10^{16}

Table 5.3: List of helium-implanted silicon devices. Shaded devices were electrically unreliable and are not included in the present discussion.

Device	Au Contact (nm)	Anneal Temp (°C)	Ion Fluence (cm^{-2})	H Implant
HeA1	20	600	4.0×10^{16}	N
HeA2	20	800	4.0×10^{16}	N
HeA3	20	N/A	4.0×10^{16}	N
HeB1	20	600	4.0×10^{16}	Y
HeB2	20	800	4.0×10^{16}	Y
HeB3	20	N/A	4.0×10^{16}	Y
HeC1	20	600	2.5×10^{17}	N
HeC2	20	800	2.5×10^{17}	N
HeC3	20	N/A	2.5×10^{17}	N
HeD1	20	600	2.5×10^{17}	Y
HeD2	20	800	2.5×10^{17}	Y
HeD3	20	N/A	2.5×10^{17}	Y

5.1 Depth and Damage Profiles

Presented in Figure 5.1 are TRIM calculations of depth and damage profiles for devices implanted with 4×10^{16} ions/cm^2 from H_2, D_2, and He gases. A 5 kV pulse was used for each calculation. Device heating, during the annealing and contact firing stages or the implantation process itself, is expected to broaden the distributions and promote desorption of gas atoms from the material, but too little is presently known to make a reliable, quantitative estimate of the effect. There are models of heat-activated diffusion in semiconductors, such as the SUPREM model developed by the Integrated Circuits Laboratory at Stanford University [80], but that model applies only to traditional CMOS dopants such as boron and arsenic and does not include the light elements used here.

5.2 Electrical Properties

The relationship between the voltage applied to each device and the resulting current flowing through it (henceforth called the *I-V curve*) was measured, and the data was fit to a typical model of a non-ideal diode. The model represents a diode as a series combination of an ideal diode, a resistor R_d, and a voltage source V_d representing the diode's turn-on voltage. The model circuit, along with some sample I-V curves, are shown in Figure 5.2.

Not all devices exhibited typical diode behaviour. Some were not electrically stable: when more than 10 V was applied in the forward direction, the current would jump erratically across a range typically spanning 1 A or more. These devices could not be characterized using the model described above, and measured light emission was typically very low and was not repeatable from test to test. Other devices were highly resistive in nature, sometimes to the point of conducting current equally in both directions. Devices exhibiting either of these irregularities are marked in red in Table 5.1 and are excluded from the data presented in this chapter. Contamination of and/or mechanical damage to the gold contact may be responsible for these problems;

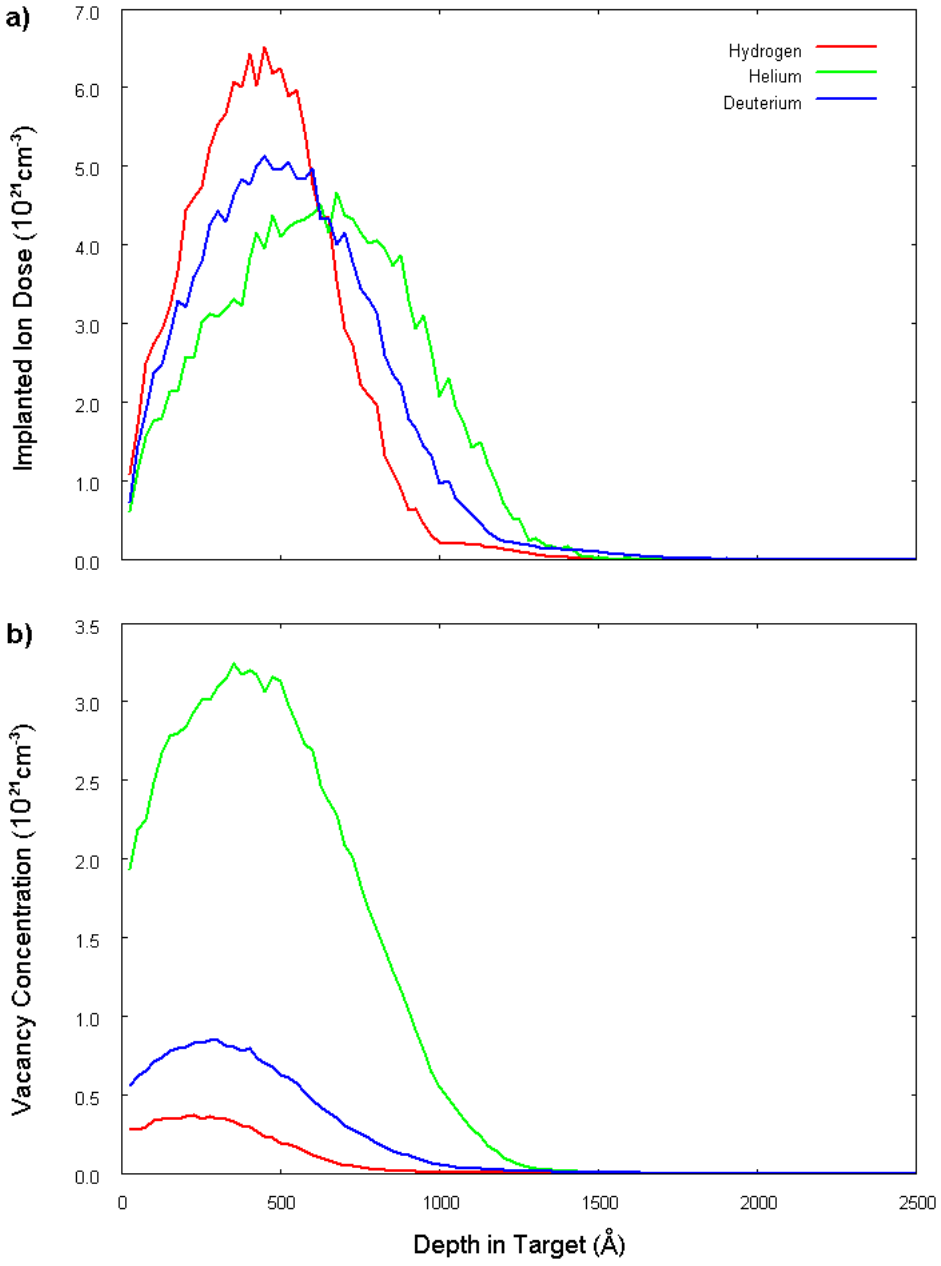

Figure 5.1: The (a) depth and (b) damage profiles of hydrogen-, helium-, and deuterium-implanted silicon as calculated by TRIM. All calculations were performed assuming an implant energy of 5 keV and ion fluence of 4×10^{16} cm^{-2}. The magnitudes of both dose and damage profiles scale linearly with implanted fluence.

blemishes and other imperfections in the gold layer were often visible after contact firing. In particular, the second batch of hydrogen-implanted devices (those labelled with the numbers 5 through 9 in Table 5.1) were accidentally overheated during contact firing and proved unreliable upon testing; none of these were used as sources of data for the present study.

The measured EL efficiency of each reliable device is plotted alongside the devices' diode characteristics in Figure 5.3. Most devices exhibited a series resistance R_d in the range of 2 to 8 Ω and a turn-on voltage V_d between 3 and 10 V. The data show no significant correlation between EL efficiency and either of these parameters.

5.3 Sources of Uncertainty

1. The light emitted from each device was not evenly distributed over the whole exposed surface area. This may have been caused by imperfections in the gold contact or by an uneven distribution of the light emitting centres themselves. Regardless of the cause, the result is that the EL intensity measured by the spectrometer may not have been equal to the mean intensity emitted by a given device.

2. The entrance slit of the SpectraPro 300i spectrometer was made 1 mm wide to increase the signal-to-noise ratio for photometric and spectroscopic measurements. A large slit width causes smearing in the measured EL spectrum, reducing its resolution. Any spectral features narrower than 5 nm in wavelength are not expected to be visible in the data.

3. The annealing temperatures listed in Tables 5.1, 5.3, and 5.2 do not include the contact firing stage, in which all devices were annealed at 400°C. There may also have been heating effects from the PII process (see Section 4.5.2) and from Ohmic heating during luminescence measurements; device temperatures at these times were not recorded, so the effect of these sources of heating on the measured EL cannot be known. However, since the devices did not show

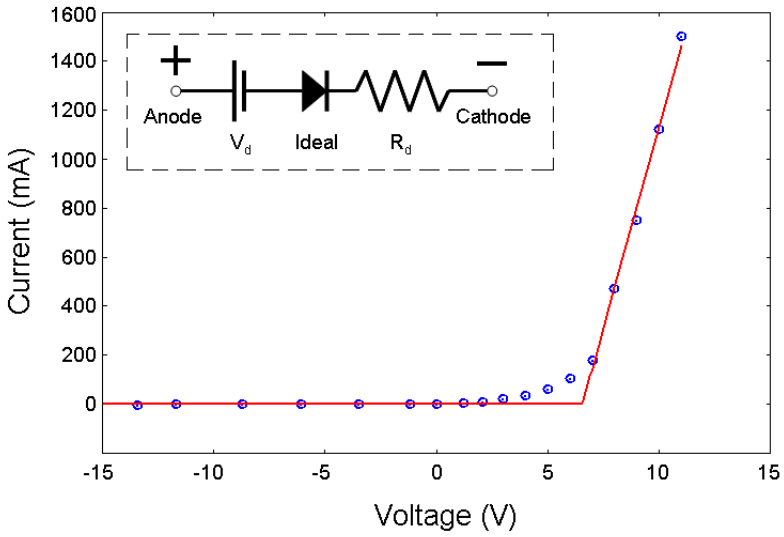

Figure 5.2: The I-V curve of the diode model used in the present research (solid line) and measured electrical data from an ion-implanted silicon device (points). The model circuit is shown in the inset. Component values for the plotted data are $R_d = 3.04\ \Omega$, $V_d = 6.56$ V.

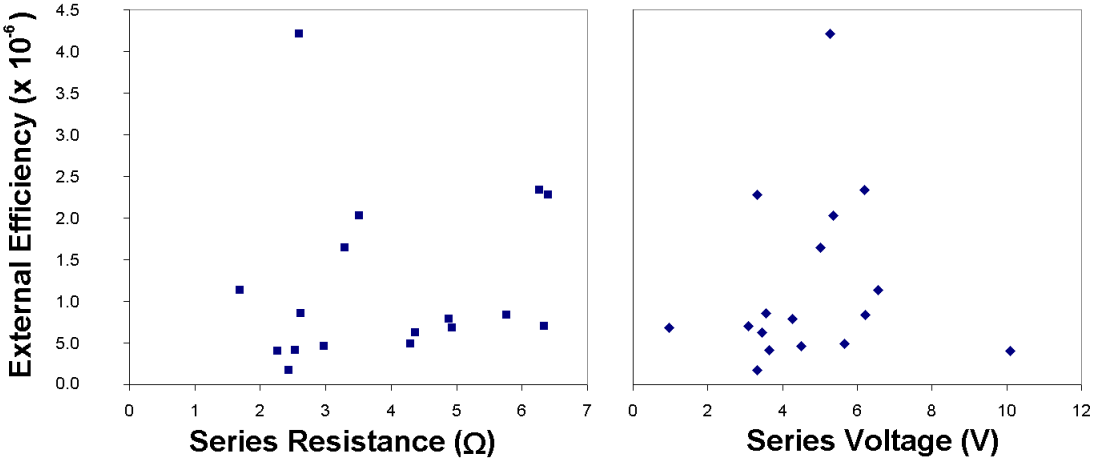

Figure 5.3: The measured EL efficiency η_x of each non-defective device versus the series resistance R_d and turn-on voltage V_d. The forward current in each device during EL measurements was approximately 2.0 A/cm^2.

visible signs of heat damage after prolonged operation in forward-conducting mode, it is safe to assume that device temperature did not rise beyond 400°C during EL measurements.

4. The EL efficiency from most devices changed over time while the diode was conducting current: the unimplanted device X1 became more efficient after several hours of operation, whereas most ion-implanted devices lost some fraction of their EL efficiency under the same conditions. As spectroscopic measurements with the SpectraPro 300i require more than one hour to complete, it is likely that some devices' overall efficiency changed over the course of the measurement, which would distort the measured spectra.

5.4 Luminescence from Unimplanted Silicon

To account for luminescence effects unrelated to implantation, such as the oxide-based luminescence described in Section 2.2.3, several devices were fabricated out of unimplanted pieces of the original silicon wafers; unfortunately, only one proved useable for the present experiments, and time constraints prohibited any additional fabrication. This device was originally found to be weakly luminescent when subjected to a current density comparable to those used on the ion-implanted devices. However, the measured EL efficiency was found to increase substantially over time, and the effect appears irreversible. Light emitted from the unimplanted device after 300 minutes' exposure to forward current was dimly visible with the naked eye in dark-adapted conditions. Figure 5.4 reports the measurements of EL efficiency as a function of forward current and elapsed time. In comparisons with ion-implanted EL devices, the quoted EL efficiency for the unimplanted device will be the final efficiency, which appeared to have stabilized after 600 minutes of continuous operation.

The device's EL spectrum was also measured and fitted to a multi-Gaussian function for comparison with spectra measured from ion-implanted devices; these results are shown in Figure 5.5. EL from the unimplanted device was predominantly red-orange, with a single broad peak centred near 650 nm and a smaller, narrower

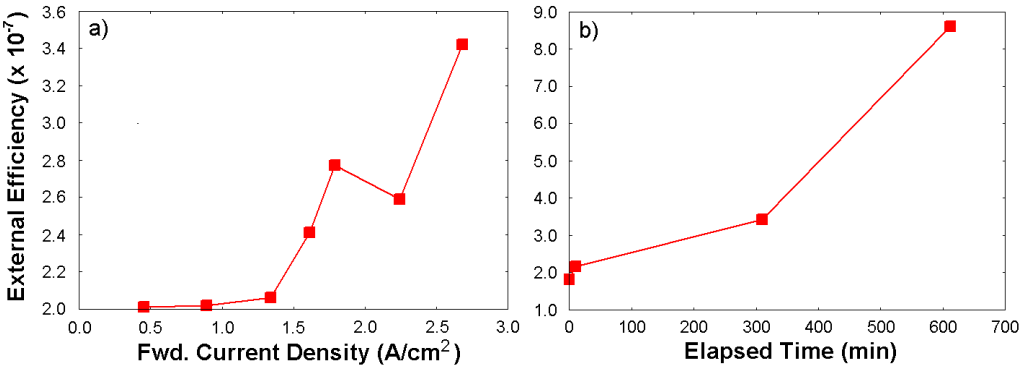

Figure 5.4: The measured EL efficiency of the unimplanted silicon device as a function of forward current density (a) and elapsed time (b). Measurements in (a) were taken at $t = 310$ minutes, and the data in (b) were collected while applying a current of 2.7 A/cm^2 to the device.

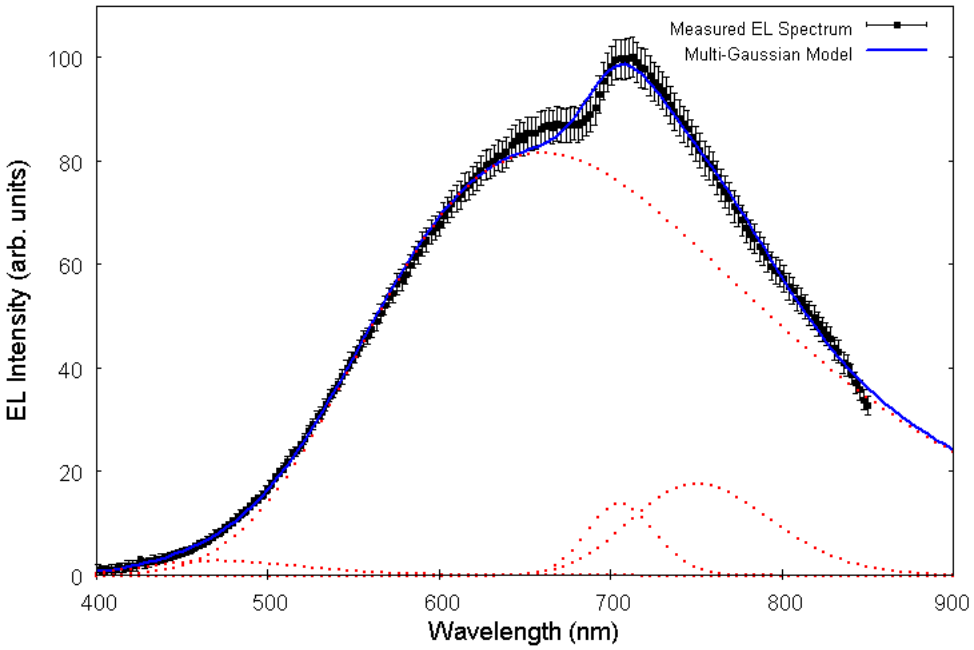

Figure 5.5: The EL spectrum measured from the unimplanted silicon device. Dotted lines represent individual Gaussian peaks, the solid line is the composite Gaussian function, and measured data are shown as individual points. Data were binned prior to Gaussian fitting with a bin size of 50; error boundaries on each point represent the standard deviation of data within each bin and the uncertainty in the thickness of the gold layer.

peak at 705 nm. The fact that the unimplanted device was visibly electroluminescent suggests that the oxide-related luminescence discussed in Section 2.2.3 is a significant or even dominant contributor to overall device EL. The remainder of this section will discuss the measurements of ion-implanted devices and identify what, if any, effect the PII process had on their luminescence properties.

5.5 Luminescence from Ion Implanted Devices

This section examines the photometric measurements of silicon devices implanted with hydrogen, helium, and deuterium to investigate changes in EL efficiency with varying ion fluence and annealing temperature. Results from the set of hydrogen-implanted devices (shown in Figure 5.6) suggest that both parameters influence the devices' light output. Peak EL efficiencies measured from devices implanted with hydrogen fluences of 2.0×10^{16} and 4.0×10^{16} cm^{-2} were considerably greater than the EL efficiencies measured from lower-fluence devices. Furthermore, the highest efficiency was found at a different annealing temperature in each case. This suggests that as the ion fluence is increased, the annealing temperature required to maximize luminescence also increases. Lastly, annealing at a temperature higher than the optimal temperature apparently quenches the enhanced luminescence very strongly. This may be part of the reason why low-fluence devices were inefficient light emitters: even the contact firing at 400°C was too hot to allow for efficient EL.

5.5.1 Hydrogenation of Helium-Implanted Devices

To study the effect of hydrogenation on the EL from ion-implanted silicon devices, a series of devices were implanted with high fluence of helium ions, and half of these were subsequently implanted with a low fluence (1×10^{14} cm^{-2}) of hydrogen ions. These devices are listed in Table 5.3. Photometric measurements from this series of devices are shown in Figure 5.7. The data clearly demonstrate that hydrogenation enhances EL efficiency in silicon diodes: the efficiency of each hydrogen-implanted device was higher than the corresponding helium-only device by a factor ranging

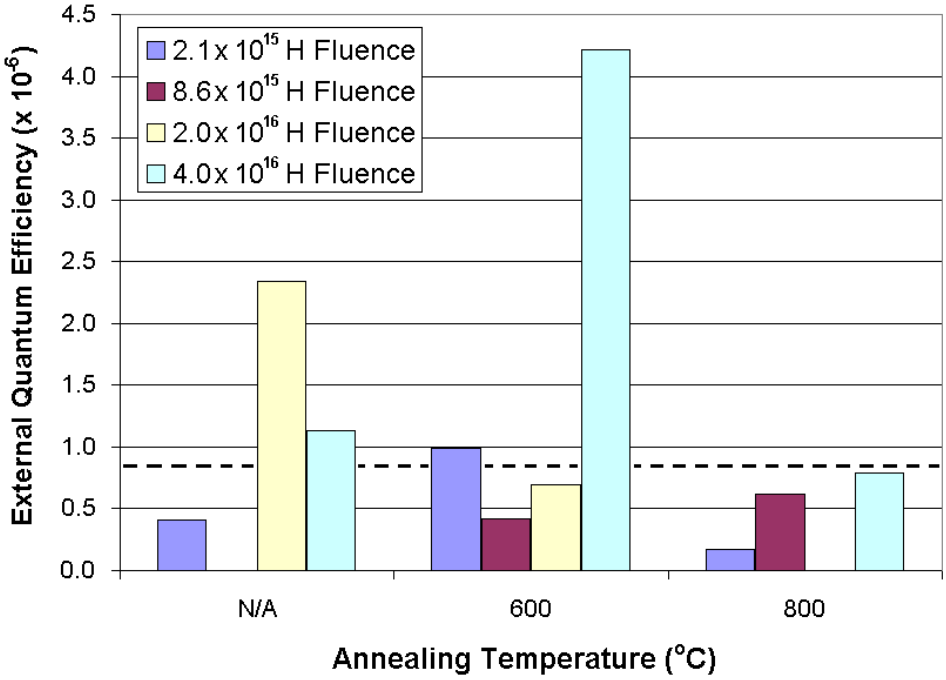

Figure 5.6: The EL quantum efficiencies of hydrogen-implanted silicon diodes as a function of implanted fluence and annealing temperature. "N/A" indicates samples that were not annealed prior to contact firing. The hydrogen fluence for each device is given in the legend in units of cm^{-2}. The dashed line shows the efficiency of the unimplanted silicon device under similar conditions. Missing bars represent defective devices whose EL characteristics were not recorded.

from 1.5 to 4. The results here also appear to agree with the measurements shown in Figure 5.6: as with the pure hydrogen-implanted devices, the maximum efficiency observed from a hydrogen-and-helium-implanted device was found at an annealing temperature of 600°C, although the maximum value (2.28×10^{-6}) was lower than the corresponding maximum from the pure-hydrogen series. This may be related to the lower hydrogen content in the helium-implanted devices, or to the higher vacancy concentration caused by helium implantation.

5.5.2 Deuterium Implantation and Lattice Damage

To determine whether the observed luminescence was dependent on ion fluence or on the lattice damage caused by the ion implantation process, several devices were

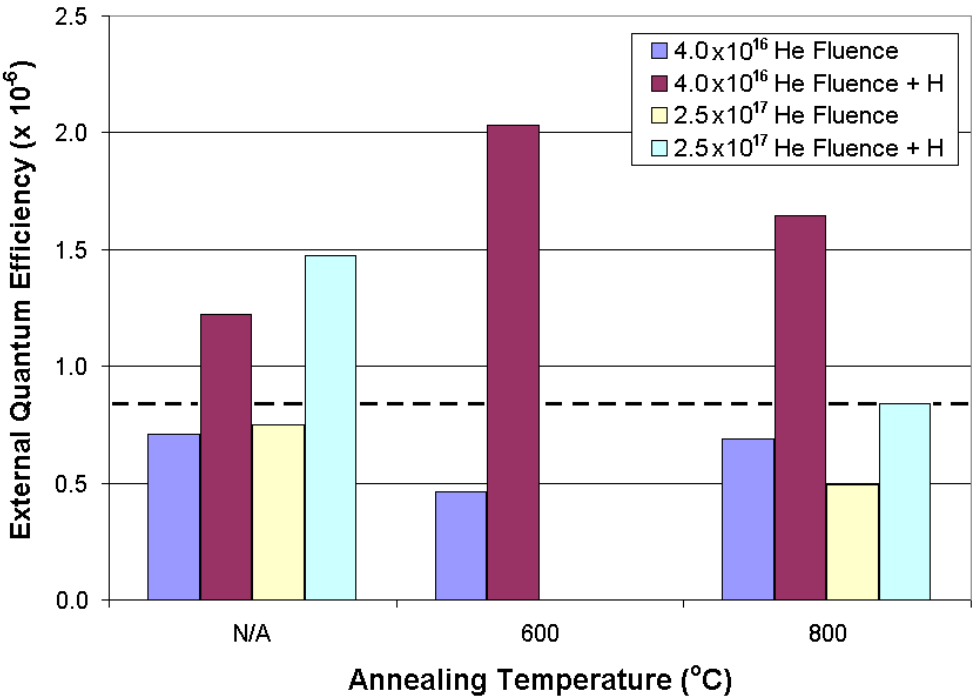

Figure 5.7: The EL quantum efficiencies of helium-implanted silicon diodes as a function of implanted fluence, annealing temperature, and hydrogen content. "N/A" indicates samples that were not annealed prior to contact firing. The helium fluence for each device is given in the legend in units of cm^{-2}. Devices marked as +H in the legend were also implanted with 1×10^{14} H ions/cm^2. The dashed line shows the efficiency of the unimplanted silicon device under similar conditions. Missing bars represent defective devices whose EL characteristics were not recorded.

implanted with deuterium (listed in Table 5.2), and the results were compared with the EL observed from hydrogen-implanted devices with similar fluence or damage characteristics. Figure 5.8a shows one such comparison: the devices represented there were all implanted with the same ion fluence (4×10^{16} cm^{-2}) but because of the higher mass of the deuterium ion, the deuterium-implanted samples suffered more lattice damage during implantation than the hydrogen-implanted devices. According to TRIM calculations, the peak vacancy concentration just after implantation was 3.7×10^{20} cm^{-3} in the hydrogen-implanted devices versus 8.5×10^{20} cm^{-3} in the deuterium-implanted devices. The data suggest that additional lattice damage, for

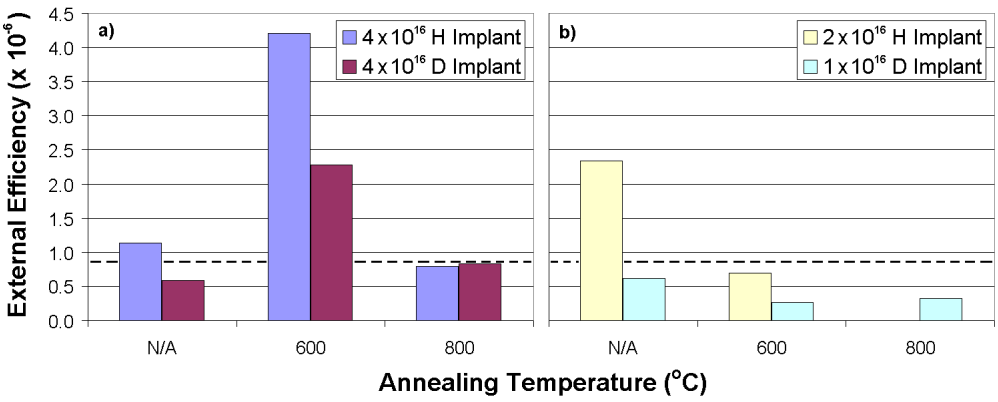

Figure 5.8: The measured EL quantum efficiencies of deuterium-implanted silicon diodes as a function of annealing temperature. "N/A" indicates samples that were not annealed prior to contact firing. Graph (a) compares the efficiency of these devices with hydrogen-implanted devices given the same ion dose; here, the peak vacancy concentration in the deuterium implants is higher by a factor of 2.3. Graph (b) compares efficiencies between devices subjected to roughly the same lattice damage; here, the peak vacancy concentration in the deuterium-implanted devices was only 20% higher than that in the hydrogen-implanted devices. Implanted ion fluences for each graph are given in the legends in units of cm^{-2}. The dashed line shows the efficiency of the unimplanted silicon device under similar conditions. The missing bar represents a defective device whose EL characteristics were not recorded.

the same ion dose, is detrimental to EL efficiency. The deuterium-implanted devices' EL also exhibits the same trend with respect to annealing temperature as the more efficient hydrogen-implanted devices; this suggests that the ion dose is the critical factor in determining the optimal annealing temperature for the devices.

Figure 5.8b shows a different comparison: here, the two sets of devices were subjected to similar lattice damage by the PII process (a peak vacancy concentration of 1.8×10^{20} cm^{-3} in the hydrogen-implanted devices versus 2.2×10^{20} cm^{-3} in the deuterium-implanted devices) but implanted with different doses of their respective ions. Again, the data suggest that a high ion dose produces enhanced EL and a large amount of lattice damage has the opposite effect.

5.5.3 Efficiency over Time

Unlike the unimplanted device, which was inefficient at first and gradually improved over time, the EL efficiencies from most ion-implanted devices were found to decay while the devices were conducting current in the forward direction. Figure 5.9 shows the EL decay in a device implanted with 2.5×10^{17} He ions/cm^2 and annealed at 800°C. The decay appears exponential at first, but becomes roughly linear after 10 minutes of operation. Different devices were found to decay at different rates; Table 5.4 shows the fraction of EL efficiency lost by several devices over 10 minutes of continuous operation at 1.3 A/cm^2 forward current density. As before, "N/A" indicates samples that were not annealed prior to contact firing. The early hydrogen- and helium-implanted devices had already been in use for some time before the decay was first noted, so no comparable data regarding their decay rates are available.

5.5.4 Efficiency and Current Density

The EL efficiency from each silicon device was found to vary with the applied forward current density, as shown in Figure 5.10. Several devices exhibited increasing EL efficiency with increasing current up to a maximum value, after which the efficiency would fall as the current density was increased further. The effect appears to be loosely correlated with both ion dose and lattice damage: low-fluence hydrogen-implanted devices had no local maximum in efficiency in the available range of current densities, while the high-fluence devices reached their maxima at current densities between 2.0 and 2.5 A/cm^2. The annealing temperature had no apparent effect on these trends.

5.5.5 Spectroscopic Measurements

In order to better understand the differences between implanted and unimplanted silicon devices, their EL emission spectra were measured with the SpectraPro 300i spectrometer. Figure 5.11 compares the EL spectra from hydrogen-implanted devices annealed at 600°C, and Figure 5.12 compares EL spectra from hydrogen-implanted

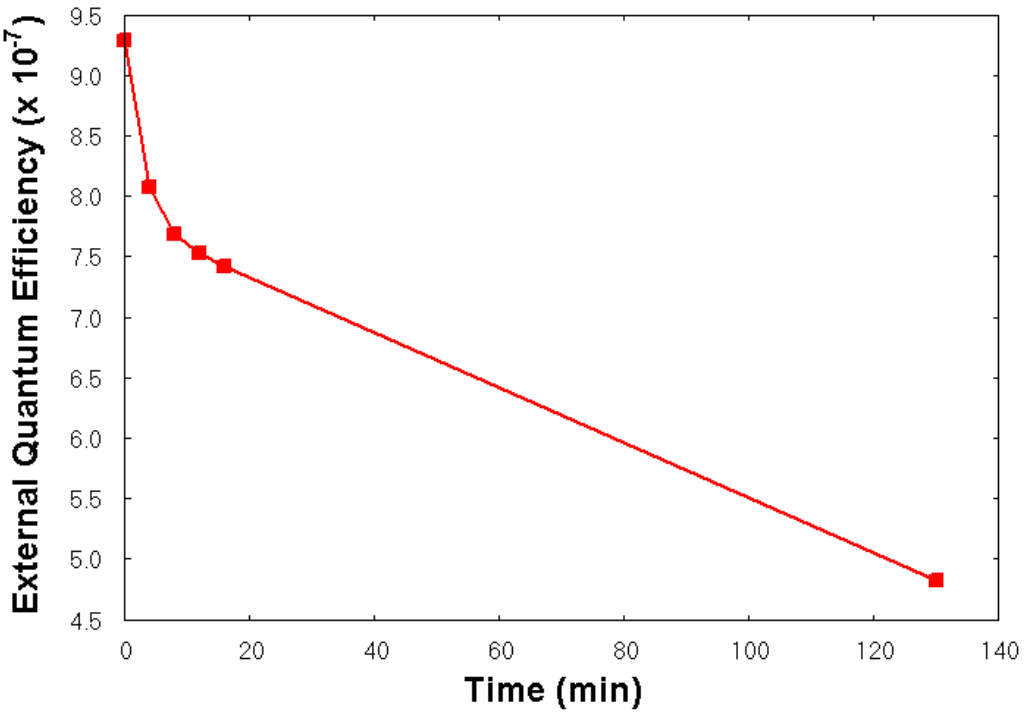

Figure 5.9: The EL efficiency of helium-implanted device HeD2 (see Table 5.3) as a function of time. The device was conducting 1.3 A/cm^2 of forward current for the entire period.

Table 5.4: Decay in EL efficiency over time

Device	Anneal Temp (°C)	Ion Fluence (cm^{-2})	Fraction of efficiency lost after 10 min
HeD2	800	2.5×10^{17}	18%
DtA1	600	1.0×10^{16}	24%
DtA3	N/A	1.0×10^{16}	37%
DtB1	600	4.0×10^{16}	4%
DtB3	N/A	4.0×10^{16}	46%

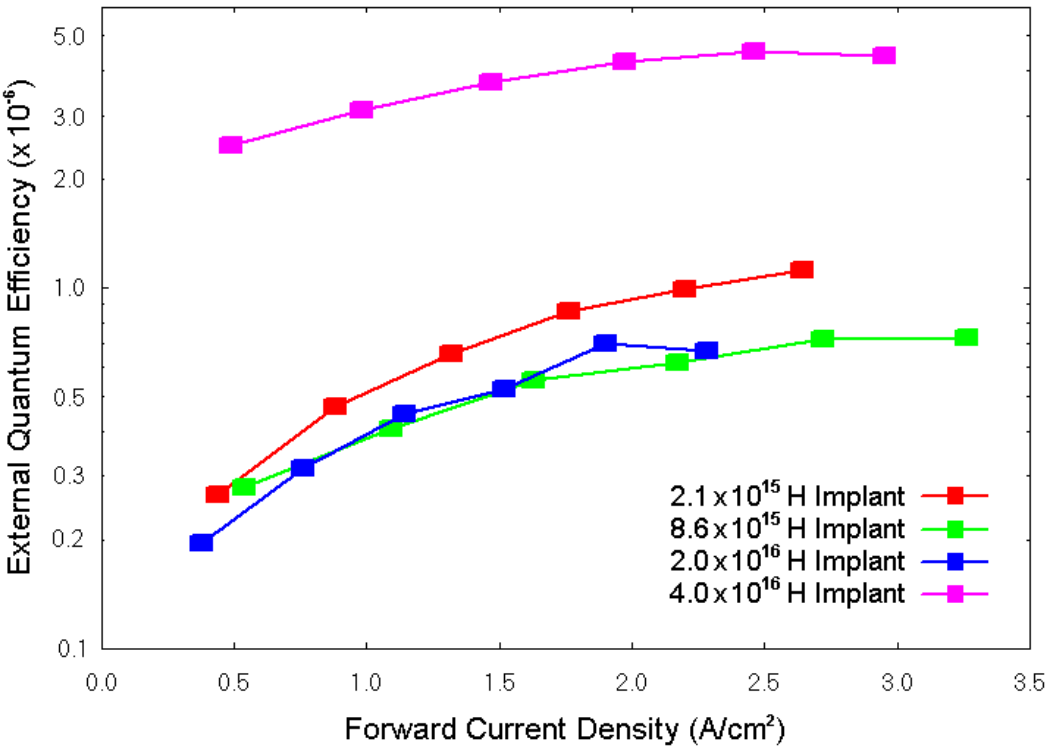

Figure 5.10: The measured EL efficiencies of hydrogen-implanted EL devices as a function of forward current density. The devices shown here were annealed at 600°C.

devices implanted with 4×10^{16} ions/cm^2. Clearly, each EL emission spectrum shares several key features: a sharp peak at 705 nm, a shoulder near 670 nm, and a long tail extending to short wavelengths. The mean wavelength of the shoulder was allowed to vary from device to device in order to better fit the small variances in shape. The EL spectrum from the unimplanted device is provided in each graph for comparison.

The data suggest that the dominant EL mechanism was essentially the same from device to device, possibly with small variations related to the PII process. The hydrogen-implanted device implanted with a high fluence and annealed at 400°C (labelled HyD2 in Table 5.1) appears to have been particularly affected by the plasma implantation process, as it is the only device whose spectral shape deviates noticeably from the others.

To quantify changes in spectral shape, the same Gaussian fitting algorithm de-

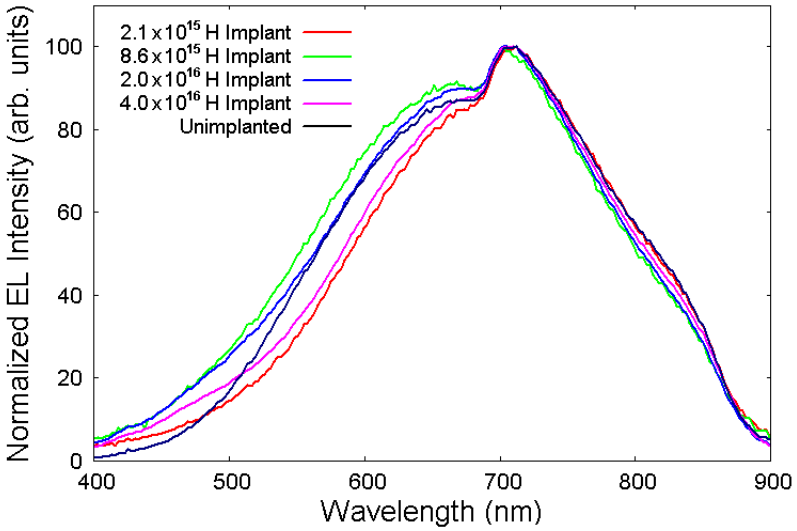

Figure 5.11: The measured EL spectra from several hydrogen-implanted devices, all annealed at 600°C. Different curves represent different implanted fluences. Spectra have been normalized to the same maximum to simplify the comparison. The normalized EL spectrum measured from the unimplanted device is provided for reference.

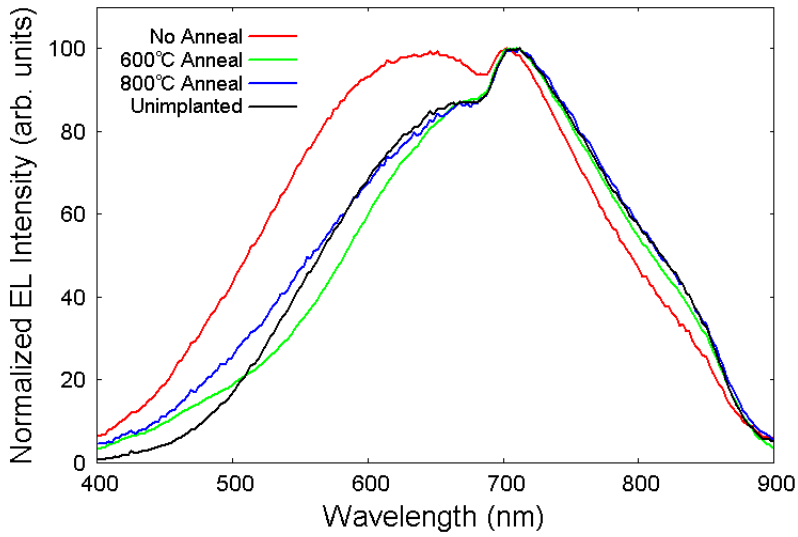

Figure 5.12: The measured EL spectra from several hydrogen-implanted devices, all implanted with a hydrogen fluence of 4×10^{16} cm^{-2}. Different curves represent devices annealed at different temperatures. Spectra have been normalized to the same maximum to simplify the comparison. The normalized EL spectrum measured from the unimplanted device is provided for reference.

scribed in Section 4.9.2 and applied to the unimplanted device's spectrum from Section 5.4 was used on the spectra from Figures 5.11 and 5.12, and the fitted magnitudes of the three dominant Gaussians (at 670 nm, 705 nm, and 750 nm) were compared with the magnitudes of the corresponding peaks from the unimplanted device. The results are shown in Figures 5.13 and 5.14. The data suggest that higher hydrogen fluence enhances EL in the narrow 705 nm peak relative to the other peaks, that hydrogen implantation with the proper annealing conditions can also enhance luminescence in the 670 nm shoulder, and that excessively high annealing temperatures tend to quench that same peak. However, the trends are relatively weak, the number of devices is small, and distortion of the spectra due to EL decay over time cannot be ruled out, so no firm conclusions can be made based on these observations.

5.6 Discussion of Results

Despite a few significant sources of uncertainty, the data presented here are sufficient to make some reasonably definitive statements regarding the origin of the observed electroluminescence. Because visible luminescence was observed from the unimplanted silicon device, it seems clear that the EL was largely or entirely emitted from the native oxide layer rather than from within the implanted silicon itself. The high degree of similarity between each measured EL spectrum supports this assertion. The QCLC model of luminescent centres presented in Section 2.2.3 appears to be a reasonable explanation for these observations. This conclusion is supported by past experiments with luminescent oxide-on-silicon devices; Figure 5.15 shows EL spectra recorded from one such experiment, which appear similar to the present results [41]. Comparable experiments conducted by other researchers in this field produced similar outcomes [46, 81, 82].

Although the spectra recorded from the ion-implanted devices were remarkably consistent, the differences in peak wavelengths and magnitudes from device to device, and deviations from the spectra shown in Figures 2.7 and 5.15, merit further discussion. These differences may be explained by the following arguments. First,

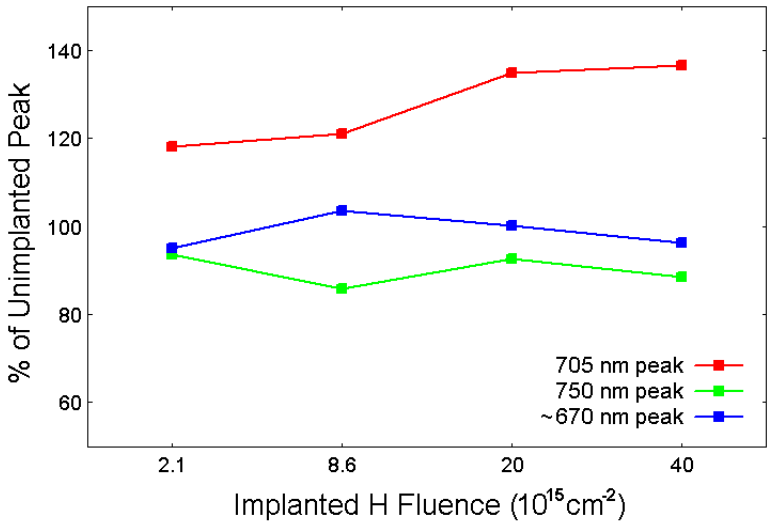

Figure 5.13: The amplitudes of the three main fitted Gaussians (centred around 670 nm, 705 nm, and 750 nm) for hydrogen-implanted devices as a function of implanted hydrogen fluence. All devices shown here were annealed at 600°C. Peak amplitudes are scaled by the amplitudes of the corresponding peaks from the unimplanted silicon device.

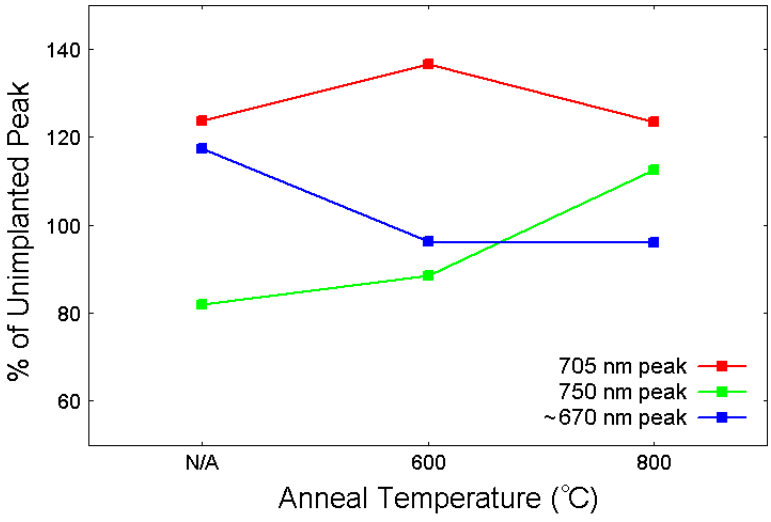

Figure 5.14: The amplitudes of the three main fitted Gaussians (centred around 670 nm, 705 nm, and 750 nm) for hydrogen-implanted devices as a function of annealing temperature. All devices shown here were implanted with a hydrogen fluence of 4×10^{16} cm^{-2}. Peak amplitudes are scaled by the amplitudes of the corresponding peaks from the unimplanted silicon device.

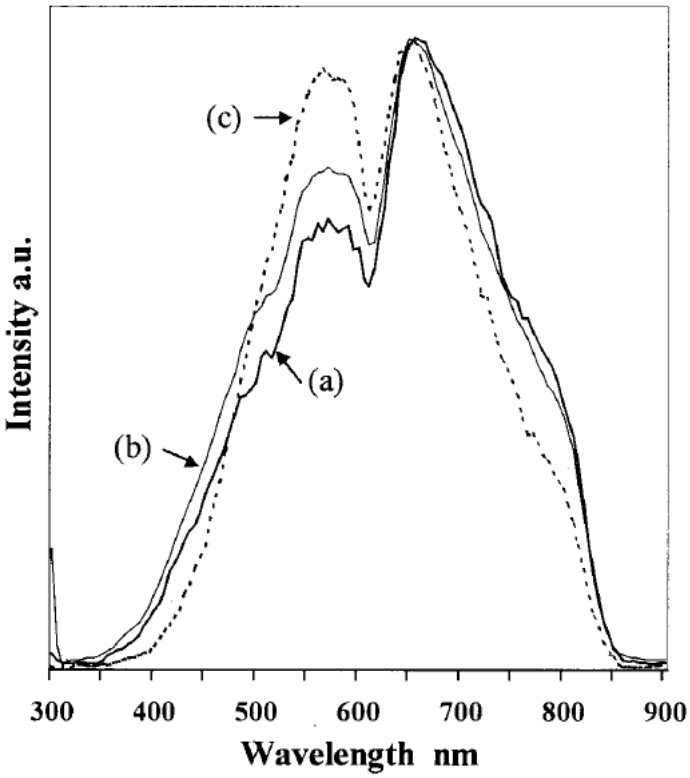

Figure 5.15: The EL emission spectra from gold-oxide-silicon devices whose oxides were (a) grown by chemical vapour deposition, (b) thermally grown, and (c) native to the silicon surface. The thickness of the oxide layer varied from 1 nm (native oxide) to 12 nm (thermally grown / CVD oxide). Taken from [41].

the ion implantation and annealing procedure causes blistering on the surface of the implanted silicon whose coarseness and magnitude depend on implanted dose and annealing conditions [38]. Figure 5.16 is an AFM image that demonstrates this effect. The blistering is sure to cause significant strain on the silicon-to-oxide interface, which in turn may change the densities and energy states of luminescent centres within the oxide layer [44]. The blistering effect could also explain the patchy, nonuniform appearance of some devices' luminescence; a thinner oxide layer in some areas would imply a larger electric field across the oxide, which would in turn lead to a different EL profile.

The second explanation for the spectral variation is that the relative magnitudes of the oxide EL bands are related to the energy used to stimulate them: for example,

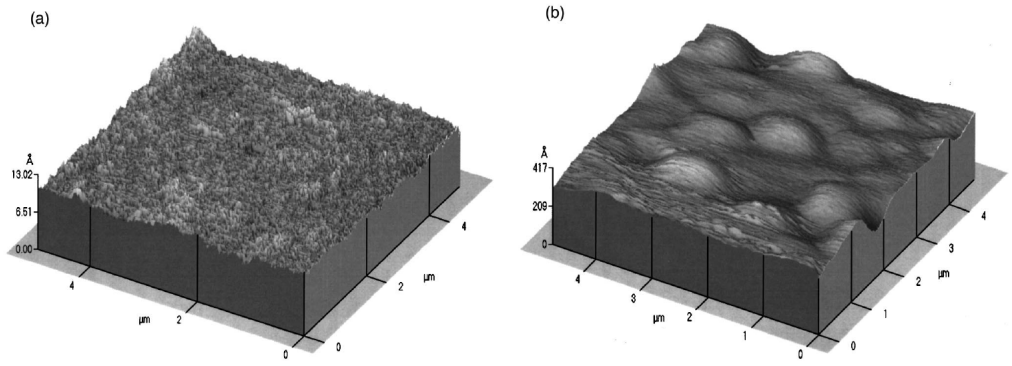

Figure 5.16: Topographic images of the surface of hydrogen-implanted silicon, as recorded by atomic force microscopy (AFM). The images show the surface (a) before and (b) after annealing at 400°C. The dimensions of the image are 5 μm by 5 μm horizontally, and 13 Å(a) or 417 Å(b) vertically. Taken from [38].

in a model of SiO_2 luminescence presented by Baraban et al., the 2.7 eV luminescent centres require a minimum electric field across the oxide layer to become active [43]. Therefore, it is likely that the shape of the EL spectrum depends on the voltage applied across the device. The devices discussed in Section 2.3 were driven with higher bias voltages than could be supplied in the present round of experiments; therefore, it is not unreasonable to expect that they would exhibit more EL in the blue-green region of the spectrum.

The surface blistering effect mentioned above may also account for the observed increase in EL efficiency with implanted dose in the hydrogen-implanted devices; since the blistering is caused by pressurized pockets of gas particles creating voids within the silicon lattice, a higher dose of gas particles would naturally lead to more structure formation on the silicon surface. These structures would increase the effective surface area of the device. If the oxide-silicon boundary is the source of the light emission, a larger surface area would allow for more luminescence. Conversely, lattice damage caused by ion implantation tends to diminish EL efficiency: among all devices implanted with a fluence of 4×10^{16} ions/cm^2, the hydrogen-implanted device (which had the lowest vacancy concentration) was roughly twice as efficient as the best helium- and deuterium-implanted devices. This relationship suggests that

the number of radiative recombinations in the oxide layer is inversely proportional to the defect concentration in the underlying silicon.

The inverse dependence of EL efficiency on defect concentration can be explained by considering the relationship between EL and the applied forward current density. In Figure 5.10, it is shown that the efficiency of most devices rose as the current density was increased, with a few reaching a peak under high-current conditions; according to the theory of carrier recombination presented in Section 2.1, this suggests that the devices were mainly operating in the Shockley-Read-Hall dominated regime, where recombination of free carriers at defect sites is significant. In principle, one could calculate the excess carrier concentration Δn within the active region of the device using the formula for the current density J,

$$J = e\Delta n \frac{\mu V}{d}, \tag{5.1}$$

and use this information to estimate the internal quantum efficiency η_i of the device. In practice, too little is known regarding the thickness d of the active layer(s), the change in the electric potential V as a function of depth, or the value of the mobility μ within the ion-implanted layer to make a reliable estimate of the value of Δn.

Even though the radiative recombination occurs in the oxide layer in the current model, the SRH recombination rate within the silicon layer remains relevant to the EL efficiency. Holes injected into the silicon through the aluminum contact must still travel through the ion-implanted silicon, possibly recombining with electrons at defect sites along the way. Therefore, a high concentration of implantation-induced defect sites should limit the number of carriers available for radiative recombination in the oxide layer by trapping and eliminating them within the implanted-silicon layer. This conclusion agrees with data reported by Kling et al., who conducted similar experiments with hydrogen-implanted silicon diodes and measured the defect concentration as a function of annealing temperature. However, their devices were annealed for only 30 minutes, a much shorter time than the extended anneals made necessary by the tube furnace used in this work. Their results are shown in Figure 5.17. It is noteworthy that the optimal annealing temperature reported in their work

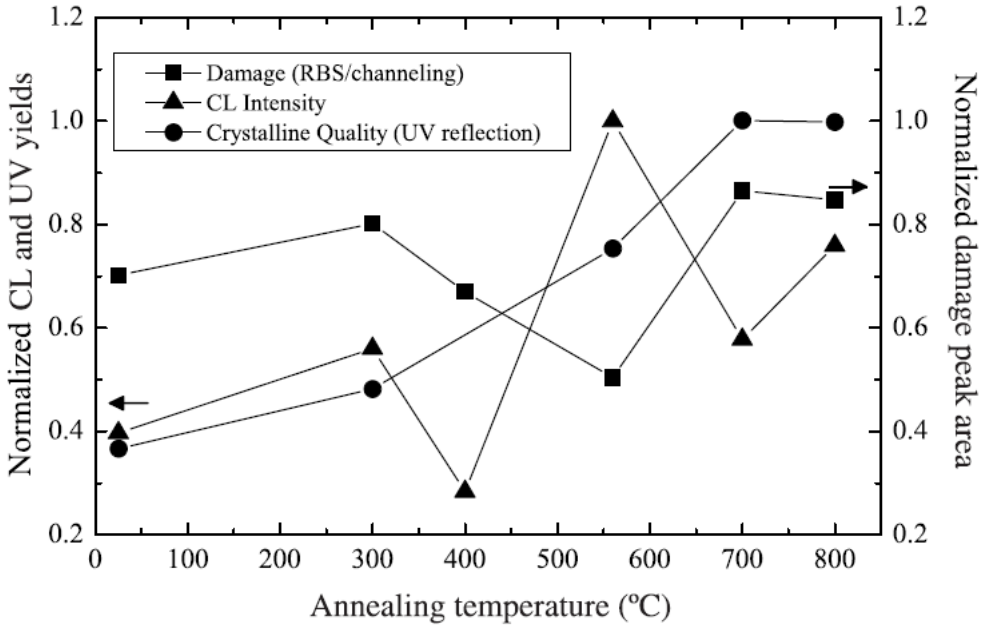

Figure 5.17: The electroluminescence (or cathodoluminescence, CL) of a set of hydrogen-implanted silicon diodes, as reported by Kling et al. [50] Measurements of lattice damage (via Rutherford back-scattering) and overall crystalline quality (via UV reflection) are also reported for each device.

for a device implanted with 1×10^{17} H ions/cm^2 was 600°C, the same temperature that produced the most efficient device in the present experiments.

The final piece of data lending support to the defect-limited model of luminescence in the oxide layer is the set of helium-implanted devices, which showed a marked increase in EL efficiency when a low dose of hydrogen was co-implanted into the silicon. Given that hydrogen is known to neutralize the potential of defect sites to act as recombination centres, one would expect a dose of hydrogen to improve the efficiency of an implanted-silicon device by reducing the rate of nonradiative SRH recombination. The annealing stages almost certainly removed most of the hydrogen from all hydrogen-implanted silicon samples, but data from the helium-implanted samples suggest that some hydrogen remained. Some of the devices (particularly the high-dose hydrogen-implanted devices) showed a sharp drop in EL efficiency as the annealing temperature was increased beyond the optimal point; this, too, may be

related to hydrogen loss. Such assertions are again supported by Kling et al., who measured the hydrogen content of their devices as a function of annealing temperature [50]. Their results are shown in Figure 5.18; they suggest that as much as 40% of the implanted hydrogen may remain in the silicon layer after annealing at 600°C. Cooke et al., who measured hydrogen content in their devices via a similar method, reported much lower hydrogen retention (on the order of 5 to 10%) for the same annealing temperatures; they, too, saw a correlation between hydrogen content and EL efficiency from their silicon devices [83]. The time-resolved decay in EL efficiency that was observed from many of the devices may also be attributed to hydrogen loss (from Ohmic heating, for example), but there is too little data regarding the EL decay to draw any firm conclusions on this point. The increase in the unimplanted device's efficiency over time also remains unexplained.

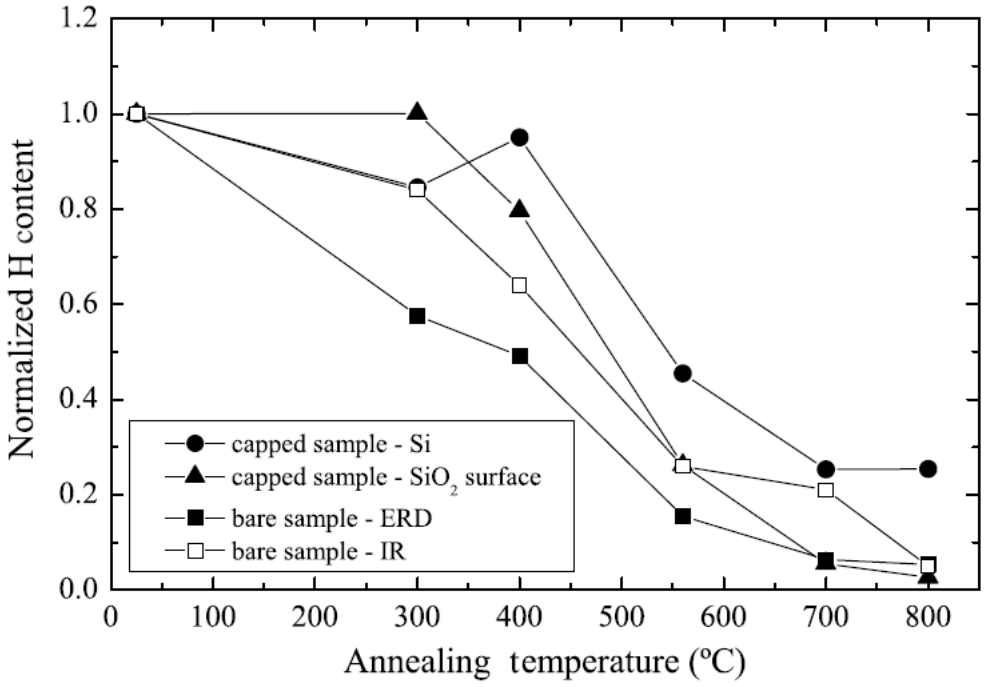

Figure 5.18: The hydrogen content of hydrogen-implanted devices prepared by Kling et al. as a function of annealing temperature [50]. The curves relevant to the present research are those for oxide-capped silicon (the top two in the legend), where the oxide was not removed prior to annealing and EL measurements. All capped-silicon measurements were performed via elastic recoil detection (ERD), using a 2.0 MeV He^+ beam.

Chapter 6

Conclusion

This thesis describes the fabrication of electroluminescent (EL) silicon diodes using plasma ion implantation (PII) with the light elements hydrogen, helium, and deuterium. The characterization and analysis of these devices were carried out chiefly through measurements of their light emission. The motivation for this work, as discussed in Chapter 1, is the development of CMOS-compatible light sources for use in integrated optoelectronics applications. Plasma ion implantation would be an excellent candidate process for fabricating such devices due to its high production volume, low cost, and proven compatibility with existing semiconductor processing techniques. Implantation with light ions was specifically chosen to build on promising preliminary results from hydrogen-implanted devices fabricated by J. T. Steenkamp (a former M. Sc. student) and James Mantyka (a former summer student). In support of the main research, a numerical algorithm was devised to analyze Langmuir probe data and estimate the plasma density using as few assumptions as possible. Custom software packages were developed to facilitate the speedy analysis of both probe data and spectroscopic measurements. Custom electronics, including a digital pulse generator and the sweeping power supply for the Langmuir probe, were built and tested. This equipment is described in Chapter 4 of the thesis. The remainder of this Chapter will discuss the silicon devices that were fabricated and tested with this equipment as well as the prospects for making more efficient silicon LEDs with this technique.

6.1 Fabricated Devices

Chapter 5 describes the electrical, photometric, and spectroscopic measurements performed on the ion-implanted silicon devices created over the course of the project. Most ion-implanted devices were found to be electroluminescent, as was a device made out of unimplanted silicon. Measurements were taken from a commercial LED in order to estimate the devices' external quantum efficiencies, which were typically on the order of 10^{-6}. Measurements of each device's EL spectrum suggested that their light emission mechanisms were similar, if not identical. It was concluded that the luminescence from both implanted and unimplanted devices was caused by radiative recombinations within the native oxide layer between the implanted silicon and the semitransparent gold contact.

The ion dose, ion species, and post-implantation annealing temperature were all found to affect the measured efficiency: a higher dose of ions, coupled with the appropriate annealing temperature, increased the EL efficiency of several ion-implanted devices well beyond the value measured from the unimplanted device. The external quantum efficiency of the best device was measured as 4.2×10^{-6}, which is nearly five times the unimplanted device's efficiency of 8.6×10^{-7}. Additional lattice damage during implantation, which was induced by implanting heavier deuterium ions in place of hydrogen, reduced the measured efficiency. The increase in efficiency with dose was attributed to structure formation on the silicon surface during the annealing stages, while the reduction in efficiency with damage was attributed to an increase in the nonradiative Shockley-Read-Hall recombination rate within the implanted silicon layer. Hydrogenation of helium-implanted devices was found to improve EL efficiency by up to a factor of 4 when compared with devices implanted with only helium; this effect was attributed to hydrogen passivation of dangling bonds within the damaged silicon layer. The loss of hydrogen due to device heating was cited as a possible cause of the decay observed in many devices' EL efficiencies over time.

6.2 Potential Applications

Based on the results reported in this thesis, several issues would have to be addressed before useful silicon LEDs could be fabricated for computing or communications applications. First, the efficiency of the devices was quite low: given a current density of 2.5 A/cm^2 and a device size of 1 mm^2 (for an integrated, monolithic LED), the best device produced in this research would induce a photocurrent between 10 and 50 nA (at best) in a high-grade silicon photodetector [5, 6]. Additional components, such as the wide-band amplifier described in [84], would be necessary to amplify this signal to useful levels.

Second, the bias voltages needed to induce detectable EL in the devices studied here were fairly high: greater than 10 volts in most cases. This is not an insurmountable problem; voltages this high or higher are often used in standard CMOS technologies with nominal voltages of 5 volts or less. However, the use of a higher voltage does introduce technical problems that require special design techniques to address [85]. Heating due to the flow of current may also be an issue: the devices studied here operated best at a current density between 1.5-2.5 A/cm^2, which for a device with an area of 1 mm^2 would mean a total current of 15-25 mA and power dissipation of roughly 240 mW. Finally, the frequency range of the LEDs produced in the present experiment remains unknown; if the relaxation time of the luminescent centres is too high, the LEDs produced here would not be able to effectively transmit digital signals at the high frequencies (GHz range) required by modern computing.

Although the issues listed above cast some doubt on the applicability of this research to the problems outlined in Chapter 1, the development of useful silicon LEDs remains a possibility. Additional research in silicon (or silicon-oxide) electroluminescence is expected to refine the fabrication process; judging by the variance between devices reported here, the EL efficiency of silicon devices might be improved by an order of magnitude or more in this way. Meanwhile, the technology of CMOS-compatible amplifiers and photodetectors continues to improve each year. However, the prospects for creating a true silicon laser, which would necessarily require pop-

ulation inversion in the luminescent centres and optical gain within the luminescent material, remain uncertain.

6.3 Future Work

The findings and conclusions in this thesis suggest a number of avenues of investigation for future researchers in this field. These include:

1. Varying the oxide thickness by thermal treatment of the silicon wafer;
2. Etching away the oxide completely before fabricating a silicon LED, to study any luminescence that might originate from beneath the oxide layer;
3. Studying the effect of impurities in the silicon wafer on device luminescence, possibly through the use of gettering techniques;
4. The use of different metal and dopant combinations, such as aluminum on n-type silicon, or transparent conductors such as indium tin oxide (ITO) or zinc oxide (ZO); and
5. The use of more characterization techniques to thoroughly probe the material and structural properties of the silicon LEDs; these could include
   (a) Atomic force microscopy (AFM), to study surface blistering;
   (b) Electron paramagnetic resonance (EPR) spectroscopy, to measure the damage distribution within the ion-implanted silicon;
   (c) Elastic recoil detection (ERD) and/or secondary ion mass spectroscopy (SIMS) to measure the oxygen and hydrogen content of the devices; and
   (d) Transmission electron microscopy (TEM), to obtain images of the internal structure of the implanted device, particularly the cavities and bubbles that form after implantation.

References

[1] R. Ho, K. W. Mai, and M. A. Horowitz, "The future of wires," *Proc. IEEE*, vol. 89, no. 4, pp. 490–504, 2001.

[2] M. Haurylau, G. Chen, H. Chen, J. Zhang, N. A. Nelson, D. H. Albonesi, E. G. Friedman, and P. M. Fauchet, "On-chip optical interconnect roadmap: Challenges and critical directions," *IEEE J. Sel. Top. Quantum Electron.*, vol. 12, no. 6, pp. 1699–1705, 2006.

[3] H. Rong, R. Jones, A. Liu, O. Cohen, D. Hak, A. Fang, and M. Paniccia, "A continuous-wave Raman silicon laser," *Nature*, vol. 433, no. 7027, pp. 725–728, 2005.

[4] Q. Xu, B. Schmidt, S. Pradhan, and M. Lipson, "Micrometre-scale silicon electro-optic modulator," *Nature*, vol. 435, no. 7040, pp. 325–327, 2005.

[5] M. K. Emsley, O. Dosunmu, and M. S. Unlu, "High-speed resonant-cavity-enhanced silicon photodetectors on reflecting silicon-on-insulator substrates," *IEEE Photonics Technol. Lett.*, vol. 14, no. 4, pp. 519–521, 2002.

[6] M. Ghioni, F. Zappa, V. P. Kesan, and J. Warnock, "A VLSI-compatible high-speed silicon photodetector for optical data link applications," *IEEE Trans. Electron Devices*, vol. 43, no. 7, pp. 1054–1060, 1996.

[7] N. Savage, "Linking with light," *IEEE Spectr.*, vol. 39, no. 8, pp. 32–36, 2002.

[8] P. M. Fauchet, "Photoluminescence and electroluminescence from porous silicon," *J. Lumin.*, vol. 70, no. 1-6, pp. 294–309, 1996.

[9] O. Jambois, H. Rinnert, X. Devaux, and M. Vergnat, "Photoluminescence and electroluminescence of size-controlled silicon nanocrystallites embedded in SiO_2 thin films," *J. Appl. Phys.*, vol. 98, no. 4, pp. 046 105–3, 2005.

[10] J. Palm, F. Gan, B. Zheng, J. Michel, and L. C. Kimerling, "Electroluminescence of erbium-doped silicon," *Phys. Rev. B*, vol. 54, no. 24, pp. 17 603–17 615, 1996.

[11] G. F. Cerofolini, L. Meda, R. Balboni, F. Corni, S. Frabboni, G. Ottaviani, R. Tonini, M. Anderle, and R. Canteri, "Hydrogen-related complexes as the stressing species in high-fluence, hydrogen-implanted, single-crystal silicon," *Phys. Rev. B*, vol. 46, no. 4, pp. 2061–2070, 1992.

[12] P. K. Chu and N. W. Cheung, "Microcavity engineering by plasma immersion ion implantation," *Mater. Chem. Phys.*, vol. 57, no. 1, pp. 1–16, 1998.

[13] W. Liu, S. C. H. Kwok, R. K. Y. Fu, P. K. Chu, T. F. Hung, Z. Xu, C. Lin, K. F. Li, H. L. Tam, and K. W. Cheah, "Room-temperature electroluminescence from H-plasma-implanted silicon," *Semicond. Sci. Technol.*, vol. 18, no. 12, pp. L55–L58, 2003.

[14] M. P. Bradley, P. R. Desautels, D. Hunter, and M. Risch, "Silicon electroluminescent device production via plasma ion implantation," *Phys. Status Solidi (c)*, vol. 6, no. S1, pp. S206–S209, 2009.

[15] P. R. Desautels, M. P. Bradley, J. T. Steenkamp, and J. Mantyka, "Electroluminescence in plasma ion implanted silicon," *Phys. Status Solidi (a)*, vol. 206, no. 5, pp. 985–988, 2009.

[16] J. R. Chelikowsky and M. L. Cohen, "Electronic structure of silicon," *Phys. Rev. B*, vol. 10, no. 12, pp. 5095–5107, 1974.

[17] Bilbao Crystallographic Server. Electronic database. [Online]. Available: http://www.cryst.ehu.es/

[18] W. Shockley and W. T. Read, "Statistics of the Recombinations of Holes and Electrons," *Phys. Rev.*, vol. 87, no. 5, pp. 835–842, 1952.

[19] C. Kittel, *Introduction to Solid State Physics*, 8th ed. New York: Wiley, 2005.

[20] D. Schroder, "Carrier lifetimes in silicon," *IEEE Trans. Electron Devices*, vol. 44, no. 1, pp. 160–170, 1997.

[21] H. Schlangenotto, H. Maeder, and W. Gerlach, "Temperature dependence of the radiative recombination coefficient in silicon," *Phys. Status Solidi (a)*, vol. 21, no. 1, pp. 357–367, 1974.

[22] R. J. Nelson and R. G. Sobers, "Minority-carrier lifetimes and internal quantum efficiency of surface-free GaAs," *J. Appl. Phys.*, vol. 49, no. 12, pp. 6103–6108, 1978.

[23] G. B. Lush, "B-coefficient in n-type GaAs," *Sol. Energy Mater. Sol. Cells*, vol. 93, no. 8, pp. 1225–1229, 2009.

[24] J. Dziewior and W. Schmid, "Auger coefficients for highly doped and highly excited silicon," *Appl. Phys. Lett.*, vol. 31, no. 5, pp. 346–348, 1977.

[25] P. P. Altermatt, J. Schmidt, G. Heiser, and A. G. Aberle, "Assessment and parameterisation of Coulomb-enhanced Auger recombination coefficients in lowly injected crystalline silicon," *J. Appl. Phys.*, vol. 82, no. 10, pp. 4938–4944, 1997.

[26] M. J. Kerr and A. Cuevas, "General parameterization of Auger recombination in crystalline silicon," *J. Appl. Phys.*, vol. 91, no. 4, pp. 2473–2480, 2002.

[27] A. Wilk, A. Kovsh, S. Mikhrin, C. Chaix, I. Novikov, M. Maximov, Y. Shernyakov, V. Ustinov, and N. Ledentsov, "High-power InAs/GaInAs/GaAs QD lasers grown in a multiwafer MBE production system," *J. Cryst. Growth*, vol. 278, no. 1-4, pp. 335–341, 2005.

[28] D. Bimberg, "Quantum dots for lasers, amplifiers and computing," *J. Phys. D*, vol. 38, no. 13, pp. 2055–2058, 2005.

[29] M. Kittler, T. Arguirov, A. Fischer, and W. Seifert, "Silicon-based light emission after ion implantation," *Opt. Mater.*, vol. 27, no. 5, pp. 967–972, 2005.

[30] H. Bleichner, P. Jonsson, N. Keskitalo, and E. Nordlander, "Temperature and injection dependence of the Shockley–Read–Hall lifetime in electron irradiated n-type silicon," *J. Appl. Phys.*, vol. 79, no. 12, pp. 9142–9148, 1996.

[31] L. T. Canham, "Silicon quantum wire array fabrication by electrochemical and chemical dissolution of wafers," *Appl. Phys. Lett.*, vol. 57, no. 10, pp. 1046–1048, 1990.

[32] V. Lehmann and U. Gösele, "Porous silicon formation: A quantum wire effect," *Appl. Phys. Lett.*, vol. 58, no. 8, pp. 856–858, 1991.

[33] A. G. Cullis, L. T. Canham, and P. D. J. Calcott, "The structural and luminescence properties of porous silicon," *J. Appl. Phys.*, vol. 82, no. 3, pp. 909–965, 1997.

[34] M. S. Hybertsen, "Absorption and emission of light in nanoscale silicon structures," *Phys. Rev. Lett.*, vol. 72, no. 10, pp. 1514–1517, 1994.

[35] B. Delley and E. F. Steigmeier, "Size dependence of band gaps in silicon nanostructures," *Appl. Phys. Lett.*, vol. 67, no. 16, pp. 2370–2372, 1995.

[36] M. V. Wolkin, J. Jorne, P. M. Fauchet, G. Allan, and C. Delerue, "Electronic States and Luminescence in Porous Silicon Quantum Dots: The Role of Oxygen," *Phys. Rev. Lett.*, vol. 82, no. 1, pp. 197–200, 1999.

[37] D. Bisero, F. Corni, C. Nobili, R. Tonini, G. Ottaviani, C. Mazzoleni, and L. Pavesi, "Visible photoluminescence from He-implanted silicon," *Appl. Phys. Lett.*, vol. 67, no. 23, pp. 3447–3449, 1995.

[38] L. Wang, R. K. Y. Fu, X. Zeng, P. K. Chu, W. Y. Cheung, and S. P. Wong, "Damage in hydrogen plasma implanted silicon," *J. Appl. Phys.*, vol. 90, no. 4, pp. 1735–1739, 2001.

[39] C. Delerue, G. Allan, and M. Lannoo, "Theoretical aspects of the luminescence of porous silicon," *Phys. Rev. B*, vol. 48, no. 15, pp. 11 024–11 036, 1993.

[40] M. Morita, T. Ohmi, E. Hasegawa, M. Kawakami, and M. Ohwada, "Growth of native oxide on a silicon surface," *J. Appl. Phys.*, vol. 68, no. 3, pp. 1272–1281, 1990.

[41] L. Heikkilä, T. Kuusela, and H. P. Hedman, "Electroluminescence in Si/SiO_2 layer structures," *J. Appl. Phys.*, vol. 89, no. 4, pp. 2179–2184, 2001.

[42] J. H. Stathis and M. A. Kastner, "Time-resolved photoluminescence in amorphous silicon dioxide," *Phys. Rev. B*, vol. 35, no. 6, pp. 2972–2979, 1987.

[43] A. P. Baraban, E. A. Semykina, and M. B. Vaniouchov, "Understanding electroluminescence from thin silicon dioxide films," *Semicond. Sci. Technol.*, vol. 15, pp. 546–550, 2000.

[44] G. Qin and Y. Jia, "Mechanism of the visible luminescence in porous silicon," *Solid State Commun.*, vol. 86, no. 9, pp. 559–563, 1993.

[45] G. Qin and G. G. Qin, "Theory on the quantum confinement-luminescence center model for nanocrystalline and porous Si," *J. Appl. Phys.*, vol. 82, no. 5, pp. 2572–2579, 1997.

[46] G. G. Qin, Y. M. Huang, J. Lin, L. Z. Zhang, B. Q. Zong, and B. R. Zhang, "Electroluminescence from Au/native oxide/p-Si and its correlation to that from Au/porous Si," *Solid State Commun.*, vol. 94, no. 8, pp. 607–612, 1995.

[47] G. Dearnaley, "Ion Implantation," *Annu. Rev. Mater. Sci.*, vol. 4, pp. 93–123, 1974.

[48] P. K. Chu, S. Qin, C. Chan, N. W. Cheung, and L. A. Larson, "Plasma immersion ion implantation–a fledgling technique for semiconductor processing," *Mat. Sci. Eng. R.*, vol. 17, no. 6-7, pp. 207–280, 1996.

[49] N. Cheung, "Plasma immersion ion implantation for semiconductor processing," *Mater. Chem. Phys.*, vol. 46, no. 2-3, pp. 132–139, 1996.

[50] A. Kling, J. C. Soares, A. Rodrguez, T. Rodrguez, M. Avella, and J. Jimnez, "Effect of thermal annealing on the optical and structural properties of silicon implanted with a high hydrogen fluence," *Nucl. Instrum. Methods Phys. Res. B*, vol. 242, no. 1-2, pp. 650–652, 2006.

[51] L. Pavesi, G. Giebel, R. Tonini, F. Corni, C. Nobili, and G. Ottaviani, "Visible luminescence from silicon by hydrogen implantation and annealing treatments," *Appl. Phys. Lett.*, vol. 65, no. 4, pp. 454–456, 1994.

[52] F. F. Chen, *Introduction to Plasma Physics and Controlled Fusion*, 2nd ed. New York: Springer, 2006.

[53] M. Risch and M. Bradley, "Predicted depth profiles for nitrogen-ion implantation into gallium arsenide," *Phys. Status Solidi (c)*, vol. 5, no. 4, pp. 939–942, 2008.

[54] M. Risch, "The Promise of Nitrogen Plasma Implanted Gallium Arsenide for Band Gap Engineering," Master's thesis, University of Saskatchewan, Dept. of Physics and Eng. Physics, 2008.

[55] M. A. Lieberman, "Model of plasma immersion ion implantation," *J. Appl. Phys.*, vol. 66, no. 7, pp. 2926–2929, 1989.

[56] M. A. Lieberman and A. J. Lichtenberg, *Principles of Plasma Discharges and Materials Processing*. New York: Wiley-Interscience, 2005.

[57] C. D. Child, "Discharge from hot CaO," *Phys. Rev. (Series I)*, vol. 32, pp. 492–511, 1911.

[58] K. S. Suraj and S. Mukherjee, "Effect of ion neutral collisions on the ion and neutral velocity distribution on negatively biased electrodes," *Surf. Coat. Technol.*, vol. 196, no. 1-3, pp. 267–270, 2005.

[59] G. W. McClure, "High-Voltage Glow Discharges in D2 Gas: Diagnostic Measurements," *Phys. Rev.*, vol. 124, no. 4, pp. 969–982, 1961.

[60] P. M. Stier and C. F. Barnett, "Charge exchange cross sections of hydrogen ions in gases," *Phys. Rev.*, vol. 103, no. 4, pp. 896–907, 1956.

[61] C. F. Barnett and P. M. Stier, "Charge exchange cross sections for helium ions in gases," *Phys. Rev.*, vol. 109, no. 2, pp. 385–390, 1958.

[62] A. Anders, *Handbook of Plasma Immersion Ion Implantation and Deposition*. New York: Wiley-Interscience, 2000.

[63] H. M. Mott-Smith and I. Langmuir, "The Theory of Collectors in Gaseous Discharges," *Phys. Rev.*, vol. 28, no. 4, pp. 727–763, 1926.

[64] I. H. Hutchinson, *Principles of Plasma Diagnostics*, 2nd ed. Cambridge University Press, 2002.

[65] L. Tonks and I. Langmuir, "A General Theory of the Plasma of an Arc," *Phys. Rev.*, vol. 34, no. 6, pp. 876–922, 1929.

[66] S. H. Lam, "Unified Theory for the Langmuir Probe in a Collisionless Plasma," *Phys. Fluids*, vol. 8, no. 1, pp. 73–87, 1965.

[67] K. U. Riemann, "Kinetic theory of the plasma sheath transition in a weakly ionized plasma," *Phys. Fluids*, vol. 24, no. 12, pp. 2163–2172, 1981.

[68] F. F. Chen, "Langmuir probe analysis for high density plasmas," *Phys. Plasmas*, vol. 8, no. 6, pp. 3029–3041, 2001.

[69] S. Qin, C. Chan, and Z. Jin, "Plasma immersion ion implantation model including multiple charge state," *J. Appl. Phys.*, vol. 79, no. 7, pp. 3432–3437, 1996.

[70] C. J. T. Steenkamp, "High Power Solid State Modulator for Plasma Ion Implantation," Master's thesis, University of Saskatchewan, Dept. of Physics and Eng. Physics, 2006.

[71] J. F. Ziegler, J. P. Biersack, and U. Littmark, *The Stopping and Range of Ions in Solids*. New York: Pergamon, 1985.

[72] S. Nunomura and M. Kondo, "Characterization of high-pressure capacitively coupled hydrogen plasmas," *J. Appl. Phys.*, vol. 102, no. 9, pp. 093 306–7, 2007.

[73] M. Fitzgerald, J. Khachan, and S. Bosi, "Relative densities of hydrogen ion species in a hollow cathode glow discharge," *Eur. Phys. J. D*, vol. 39, no. 1, pp. 35–39, 2006.

[74] M. Tuszewski and J. A. Tobin, "The accuracy of Langmuir probe ion density measurements in low-frequency (RF) discharges," *Plasma Sources Sci. Technol.*, vol. 5, no. 4, pp. 640–647, 1996.

[75] C. J. T. Steenkamp and M. P. Bradley, "Active Charge/Discharge IGBT Modulator for Marx Generator and Plasma Applications," *IEEE Trans. Plasma Sci.*, vol. 35, no. 2, pp. 473–478, 2007.

[76] G. A. Emmert, "Model for expanding sheaths and surface charging at dielectric surfaces during plasma source ion implantation," *J. Vac. Sci. Technol. B*, vol. 12, pp. 880–883, 1994.

[77] P. B. Johnson and R. W. Christy, "Optical Constants of the Noble Metals," *Phys. Rev. B*, vol. 6, no. 12, pp. 4370–4379, 1972.

[78] J. Geist, "Silicon (Si) revisited (1.1-3.1 eV)," in *Handbook of Optical Constants of Solids*, E. D. Palik, Ed. San Diego: Academic, 1998, vol. III, pp. 519–529.

[79] GNUPLOT. Open-source software. [Online]. Available: http://www.gnuplot.info

[80] C. P. Ho, J. D. Plummer, S. E. Hansen, and R. W. Dutton, "VLSI Process Modeling - SUPREM III," *IEEE Trans. Electron Devices*, vol. 30, no. 11, pp. 1438–1453, 1983.

[81] G. F. Bai, Y. Q. Wang, Z. C. Ma, W. H. Zong, and G. G. Qin, "Electroluminescence from Au/native silicon oxide layer/p+ Si and Au/native silicon oxide layer/n+ Si structures under reverse biases," *J. Phys. Condens. Matter*, vol. 10, no. 44, pp. L717–L721, 1998.

[82] J. Yuan and D. Haneman, "Visible electroluminescence from native SiO_2 on n-type Si substrates," *J. Appl. Phys.*, vol. 86, no. 4, pp. 2358–2360, 1999.

[83] D. W. Cooke, B. L. Bennett, E. H. Farnum, W. L. Hults, K. E. Sickafus, J. F. Smith, J. L. Smith, T. N. Taylor, P. Tiwari, and A. M. Portis, "SiO_x luminescence from light-emitting porous silicon," *Appl. Phys. Lett.*, vol. 68, no. 12, pp. 1663–1665, 1996.

[84] C.-W. Kim, M.-S. Kang, P. T. Anh, H.-T. Kim, and S.-G. Lee, "An Ultra-Wideband CMOS Low Noise Amplifier for 35-GHz UWB System," *IEEE J. Solid-State Circuits*, vol. 40, no. 2, pp. 544–547, 2005.

[85] H. Ballan and M. Declercq, *High voltage devices and circuits in standard CMOS technologies*. New York: Springer, 1999.

[86] International Commission on Illumination (CIE). CIE 1964 Supplementary Standard Colorimetric Observer data. Free document. [Online]. Available: http://www.cie.co.at/main/freepubs.html

Appendix A

Quantum Efficiency Calculation

The SpectraPro 300i spectrometer and attached PI-MAX camera described in Section 4.9 measure light in CCD counts, not actual photons. Although this is sufficient for comparisons between devices, a reasonable estimate of each device's external quantum efficiency is needed in order to evaluate the devices' potential applicability to real problems. The general formula for the efficiency η_x, in terms of known or measurable quantities, is

$$\eta_x = \frac{N_{CT}}{\beta} \cdot G \cdot \frac{e}{I_D}, \tag{A.1}$$

where N_{CT} is the total number of counts detected per second on the CCD array of the camera, β is the detector efficiency (counts per photon), I_D is the drive current through the electroluminescent device, and G is a geometric factor relating the detected light to the total emitted light. N_{CT} is a measured quantity, and I_D is a known parameter; therefore, only β and G need to be determined in order to calculate η_x.

A.1 Geometric Factor

Consider the setup presented in Figure A.1: a light source of area A_D is placed a distance L from the entrance slit of a spectrometer or photometer; the slit has area A_{slit}. The light source radiates photons through its viewing angle θ, delivering power to the surface of the spherical cap subtended by θ. It is assumed in this calculation that the irradiance (power per unit area) delivered to the spherical cap is uniform. It is also assumed that the detector behind the slit can only record light that is normally incident on the slit. The area of the entrance slit of the SpectraPro 300i is 4 mm^2.

Under this arrangement, the slit can only receive light from an area on the emitter equal to its own area A_{slit}. Furthermore, the slit area receives only a fraction of the total light emitted from this small area, equal to the ratio of the slit area to the area of the spherical cap at radius L. The area of a spherical cap of radius L, subtended by the angle θ, is

$$A_{cap} = 4\pi L^2 \sin^2\left(\frac{\theta}{4}\right), \tag{A.2}$$

so the ratio of detected light to the sum of all light emitted by the device (the geometric factor G) must be

$$G = 4\pi L^2 \sin^2\left(\frac{\theta}{4}\right) \frac{A_D}{A_{slit}^2}. \tag{A.3}$$

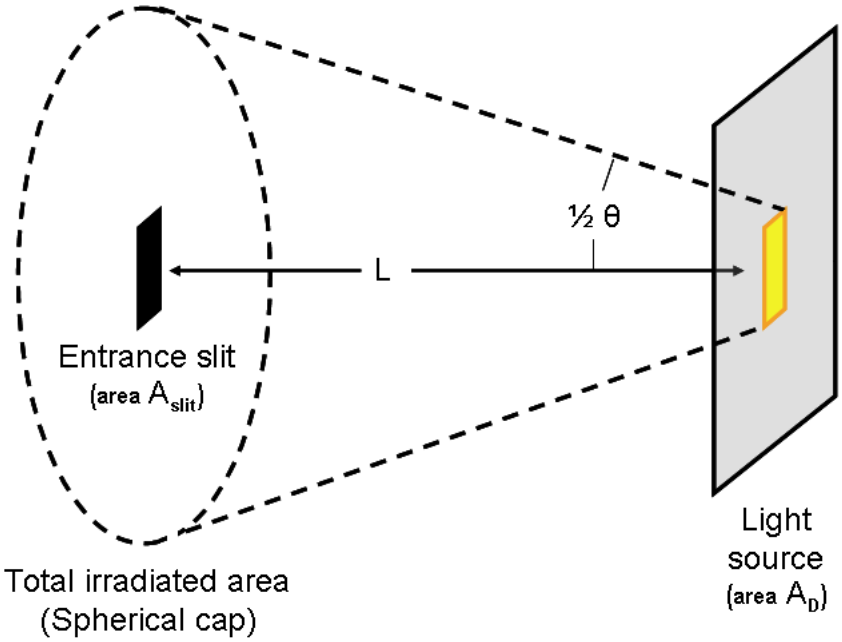

Figure A.1: The geometry of the present photometry and spectrometry measurements. In general, only a small portion of the total area A_D of the light source is visible to the entrance slit of the spectrometer, positioned at a distance L from the emitter's surface. It is assumed that this portion of the light source radiates photons uniformly across the viewing angle θ, distributing its power evenly over the area of the subtended spherical cap of radius L.

For spectrometry and photometry measurements with implanted-silicon devices, the value of L is 25 mm, the value of θ is assumed to be 180°, and the emitter area A_D varies from device to device. The setup used to determine the detector efficiency was slightly different and will be described in the next section.

A.2 Detector Efficiency

To determine the efficiency of the spectrometer - the number of counts detected per photon received - the entrance slit was illuminated with a commercial red LED (a LUMEX SD-LX5093HD) and measured its output. The LED was positioned as shown in Figure A.1 with the distance L equal to 12.5 mm. The datasheet for the SD-LX5093HD gives the viewing angle θ as 60°, and it is assumed that the light-emitting die within the diode is the same size or smaller than the slit width, so $A_D = A_{slit}$ in Eq. A.3 for this measurement.

The luminous intensity of the SD-LX5093HD is given as 0.005 candelas. The candela is a base SI unit defined as the luminous intensity of a source that emits

monochromatic radiation of frequency 540×10^{12} Hz, in a given direction, with a radiant intensity of 1.464×10^{-3} W/sr. For a given intensity I_C in candelas, there is a relationship

$$I_C(\lambda) = 683.002 \cdot \overline{y}(\lambda) \cdot I_R(\lambda), \tag{A.4}$$

where $\overline{y}(\lambda)$ is the standard CIE luminosity function shown in Figure A.2 and $I_R(\lambda)$ is the radiant intensity of the LED in W/sr.

To calculate the total number of photons, the spectral output of the LED was measured (Figure A.3) and the data were normalized such that

$$I_R(\lambda) = I f_n(\lambda),$$
$$\int f_n(\lambda) d\lambda = 1,$$

where I is a scalar constant that represents the total radiant intensity. To find the number of emitted photons, given the radiant intensity I_R, the units of the constant I are changed such that

$$I_R(\lambda) = P\left(\frac{hc}{\lambda}\right) f_n(\lambda),$$

where P is the radiant intensity in photons/sr·s.

One can integrate over all wavelengths to find P:

$$P = \frac{1}{hc \cdot 683.002}\left[\int I_C(\lambda) d\lambda\right]\left[\int \frac{\overline{y}(\lambda) f_n(\lambda)}{\lambda} d\lambda\right]^{-1},$$

where $\int I_C(\lambda) d\lambda$ is the total luminous intensity (0.005 cd). Completing the calculation, the emitted photon density from the LED is

$$P = 6.873 \times 10^{14} \ \frac{\text{photons}}{\text{sr} \cdot \text{s}}. \tag{A.5}$$

To find the total number of photons emitted by the LED, P is multiplied with the solid angle Ω subtended by the viewing angle θ,

$$\Omega = 2\pi\left(1 - \cos\frac{\theta}{2}\right) \text{ sr},$$

where θ is 60° according to the SD-LX5093HD datasheet. The total number of photons emitted by the LED is therefore

$$P\Omega = 5.786 \times 10^{14} \text{ photons/s}.$$

The number of photons incident on the entrance slit is a fraction of the value of $P\Omega$ equal to the inverse of the geometric factor G, whose value is 32.88 for this measurement. This means that the PI-MAX camera detected 1.759×10^{13} photons/s. The WinSpec software recorded 1.6364×10^{11} counts/s when the camera was illuminated by the LED. Therefore, the detector efficiency must be

$$\beta = 9.3 \times 10^{-3} \text{ counts/photon}. \tag{A.6}$$

If this value of β is inserted into Eq. A.1 along with the equation for G (Eq. A.3), the result is a complete formula for calculating the quantum efficiency of any electroluminescent silicon device. The formula is given in Section 4.9.1 as Eq. 4.6.

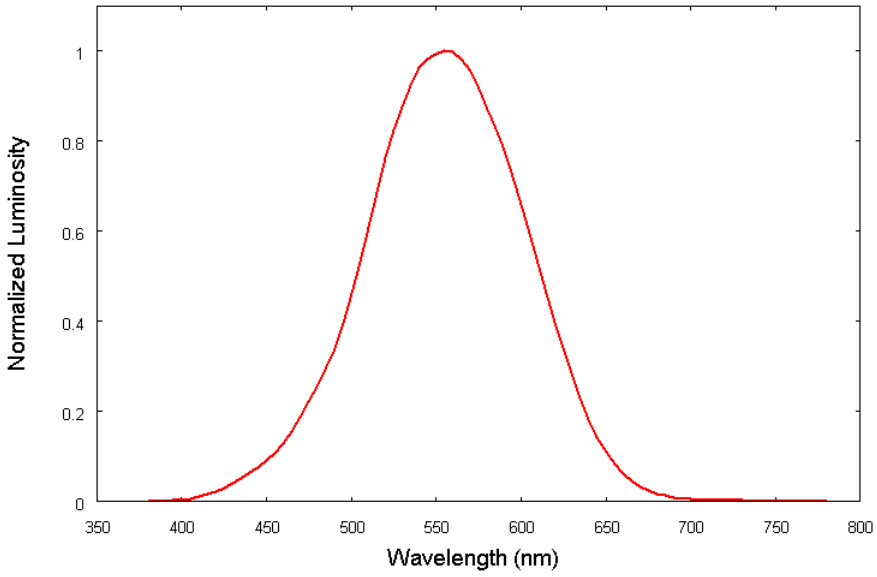

Figure A.2: The standard CIE photopic luminosity function, representing the sensitivity of the average human eye to light in the visible spectrum in a well-lit environment. The y-axis is unitless and the function is normalized such that the maximum at 555 nm is exactly 1. After [86].

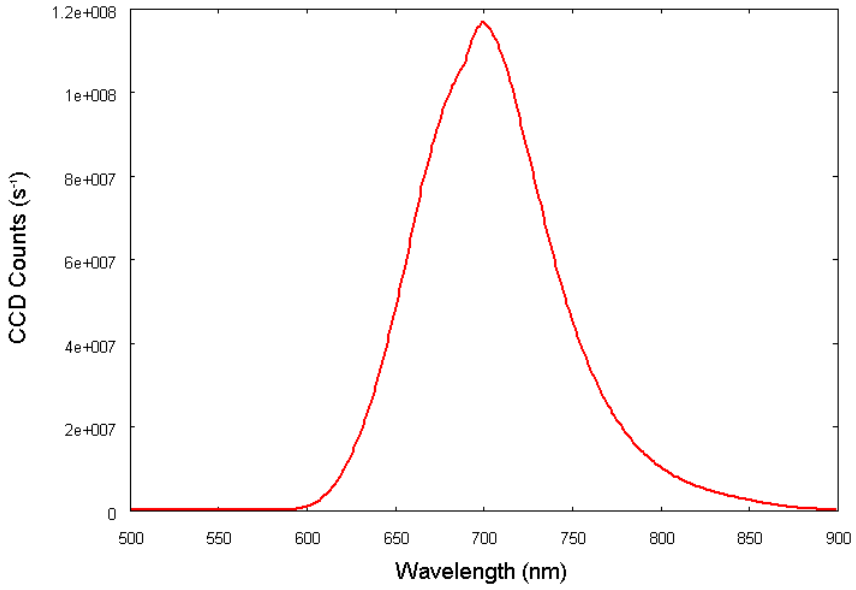

Figure A.3: The spectrum of a LUMEX SD-LX5093HD red LED, as measured by the SpectraPro 300i spectrometer and PI-MAX camera. The data shown here are not yet normalized.

Appendix B

Custom Devices and Tools

B.1 Digital Pulse Generator

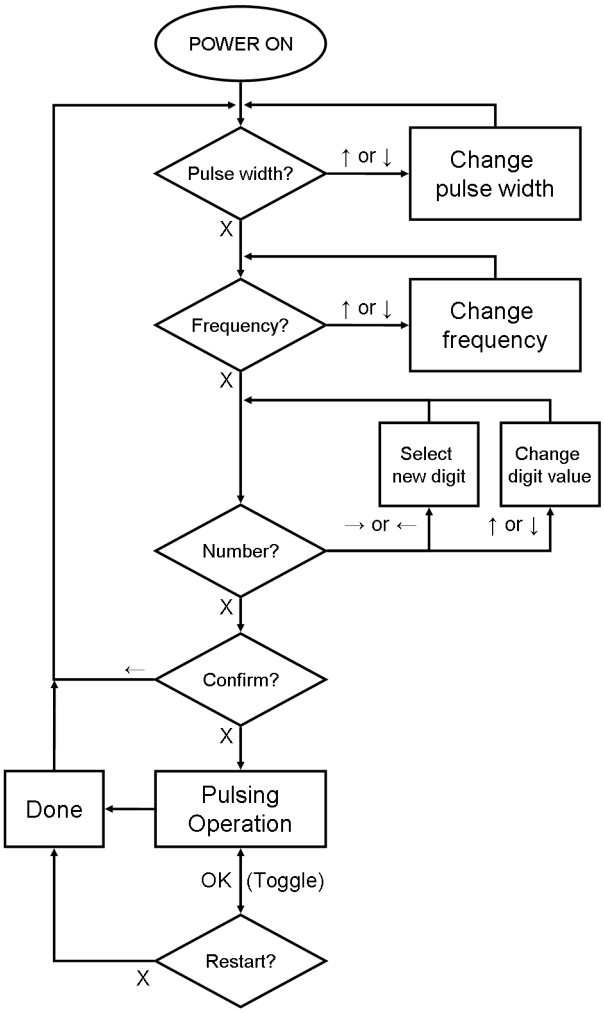

Figure B.1: The operational flowchart for the custom digital pulse generator used to trigger high-voltages pulses from the Marx stages. Prompting and feedback to the user is provided through an LCD unit mounted on the front panel of the pulse generator. The operation of the circuit is controlled by a PIC18F4520 microcontroller.

B.2 Langmuir Probe Power Supply

The Langmuir probe power supply is designed to produce a stable triangle-wave (sawtooth) voltage signal with user-controlled amplitude, frequency, and DC offset voltage. The circuit used to generate this signal is composed of two stages: the *ramp generator* (Figure B.2), which produces a small-signal triangle wave; and the *amplifier* (Figure B.3), which amplifies the signal to useful levels. The output is controlled by three variable resistors, R_{FREQ}, R_{AMP}, and R_{DCO}, whose values can be set in the range $0 \rightarrow 100\mathrm{k}\Omega$. Their relations to the frequency (f), peak-to-peak voltage ($V_{peak-peak}$), and DC offset voltage (V_{DC}) are given by the following equations:

$$f \propto \frac{1}{4CR_2}\left(\frac{R_{FSET}+R_{FREQ}}{R_1}\right),$$

$$V_{peak-peak} \propto \left(\frac{22k\Omega}{22k\Omega+R_{AMP}}\right),$$

$$V_{DC} \propto \left(1-\frac{47k\Omega+R_{DCO}}{97k\Omega}\right).$$

The constants of proportionality for each quantity are on the order of 1.0 (generally between 0.5 and 2.0); they should be exactly 1.0 in theory, but non-idealities in the real circuit cause deviations from the predicted behaviour. I do not consider this a significant flaw, since the output is stable over time (corrections due to non-idealities are constant) and the controlling resistors may be adjusted until one obtains the desired waveform.

B.3 Software Screenshots

Figures B.4 and B.5 are screenshots taken of the custom software described in Sections 4.6 and 4.9.2 of the thesis. Both pieces of software were programmed in C++ and employ the Qt package to implement the graphical interface.

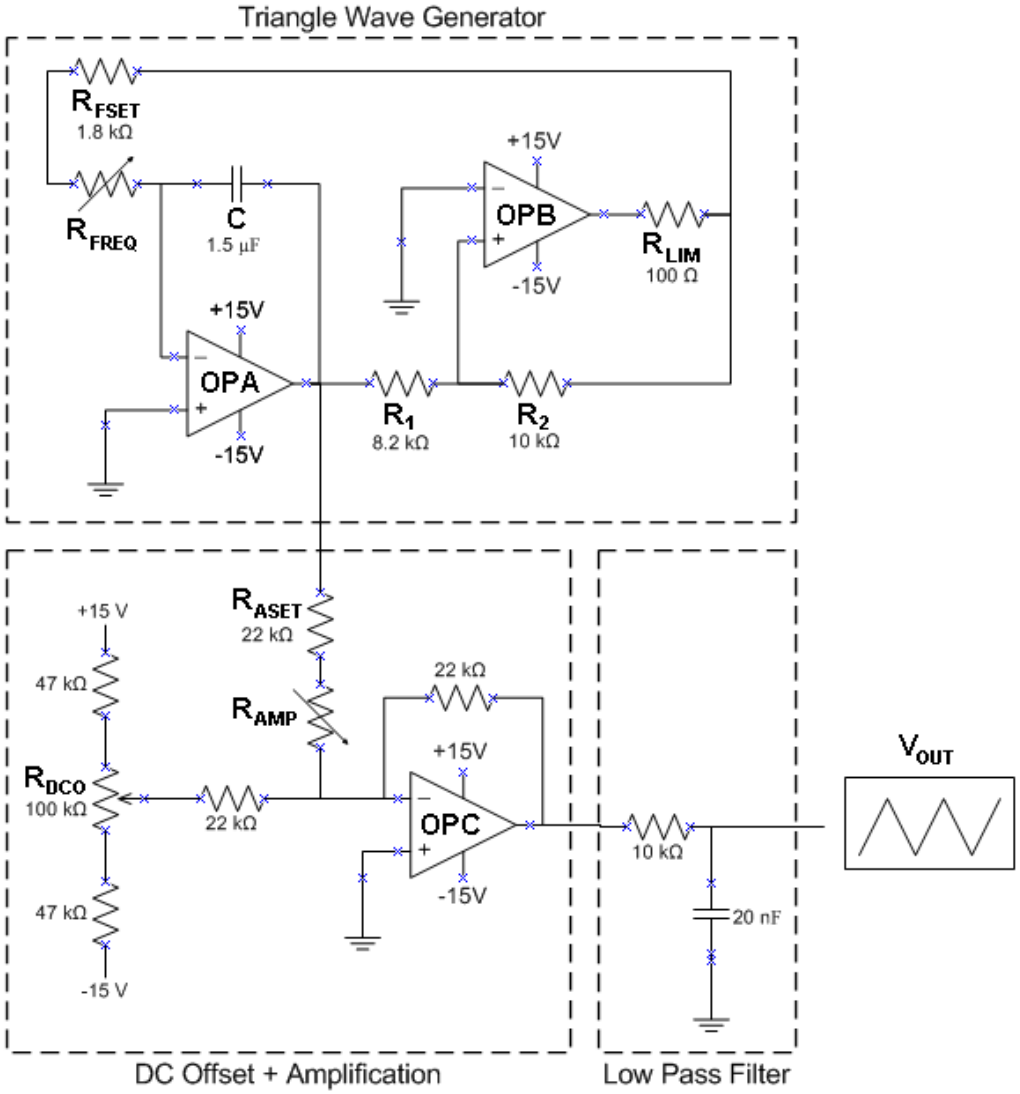

Figure B.2: The circuit used to generate a linear voltage sweep for the Langmuir probe. The charging and discharging of capacitor C, linked to an op-amp integrator (OPA), produces a series of linear voltage ramps. The polarity of the capacitor is periodically reversed by a comparator (OPB). The frequency of this oscillation can be controlled via resistor R_{FREQ}. The summing amplifier (OPC) allows the user to change the amplitude of the sweep and add a DC offset by manipulating resistors R_{AMP} and R_{DCO}, respectively.

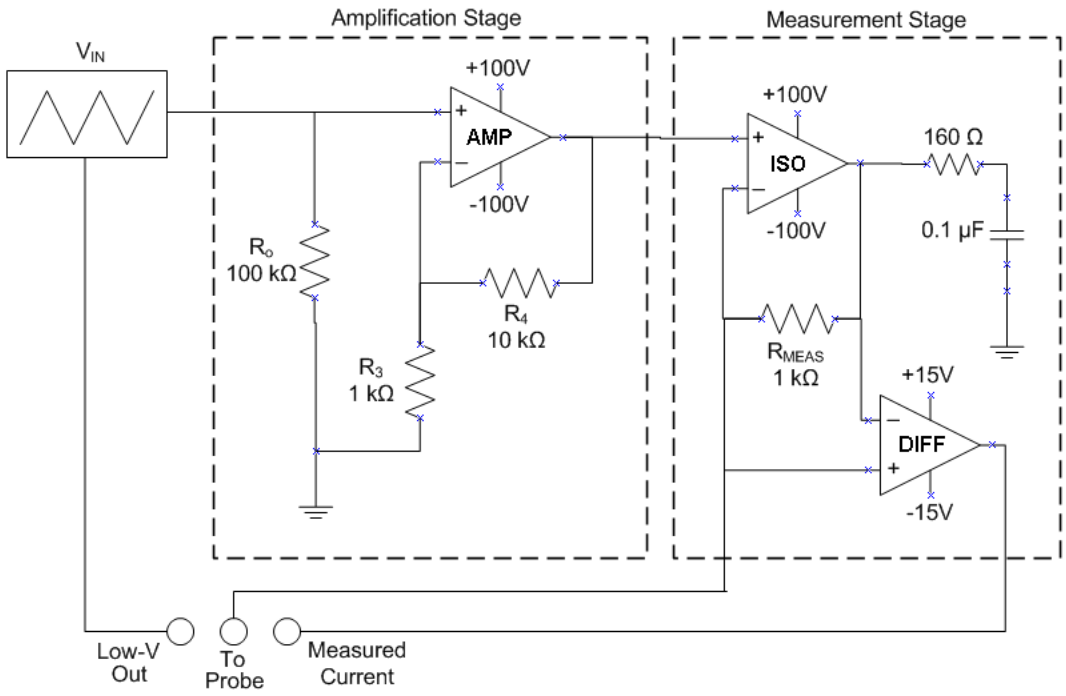

Figure B.3: The circuit used to amplify the Langmuir probe sweep to a useful voltage and to measure the plasma current. The output of the low-voltage stage is 10x amplified by the first op-amp (AMP). The second op-amp (ISO) serves to isolate the voltage sweep from the Langmuir probe by establishing a virtual connection between the (+) and (-) terminals of the amplifier; this means that the potential drop across R_{meas} does not affect the voltage applied to the probe. The current through R_{meas} is measured by a unity-gain differential amplifier (DIFF).

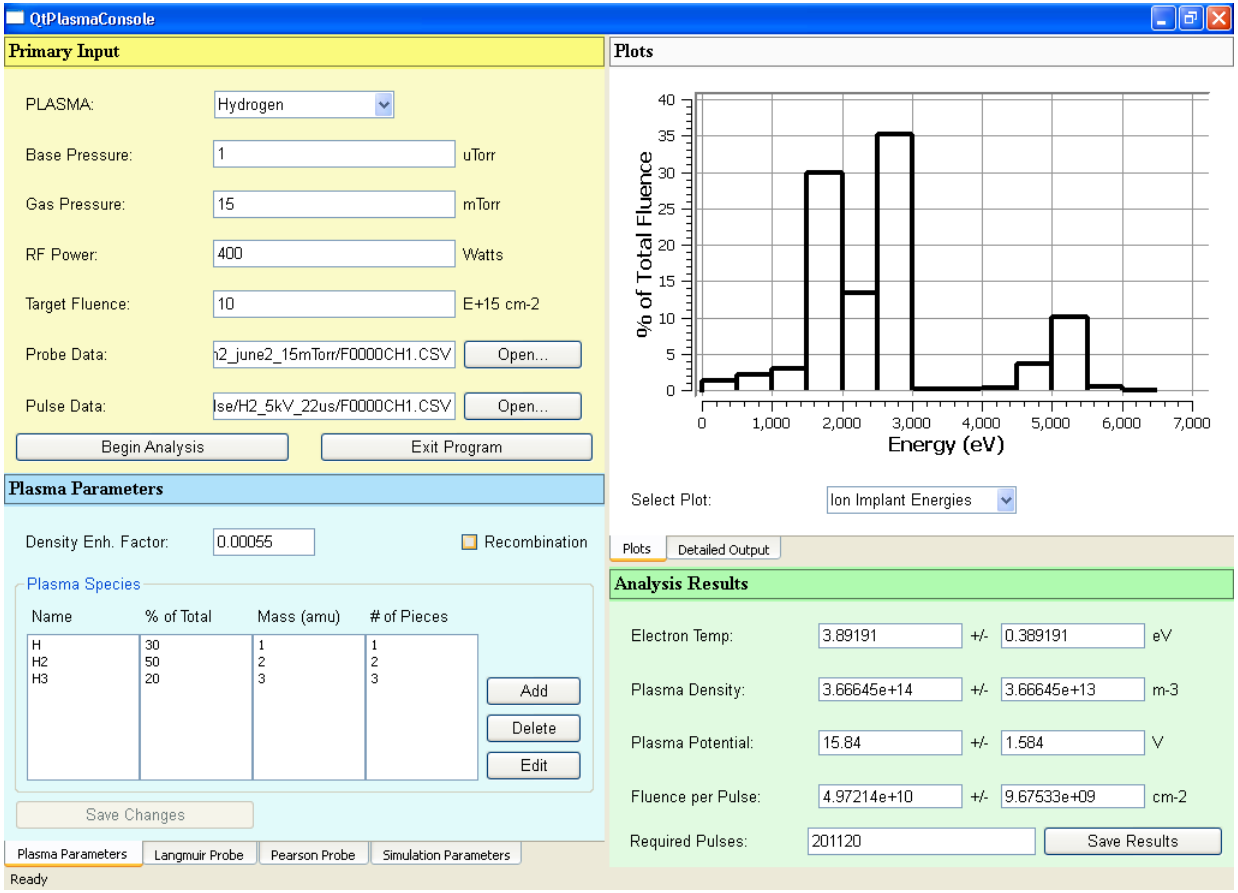

Figure B.4: The QtPlasmaConsole main window. The four sub-windows, clockwise from the upper left, are: INPUT, where the user provides the software with required data and input files; OUTPUT, where calculation steps, error messages, and data plots may be reviewed; RESULTS, where final results are shown and can be saved to disk; and PARAMETERS, where various secondary inputs to the code may be reviewed and modified.

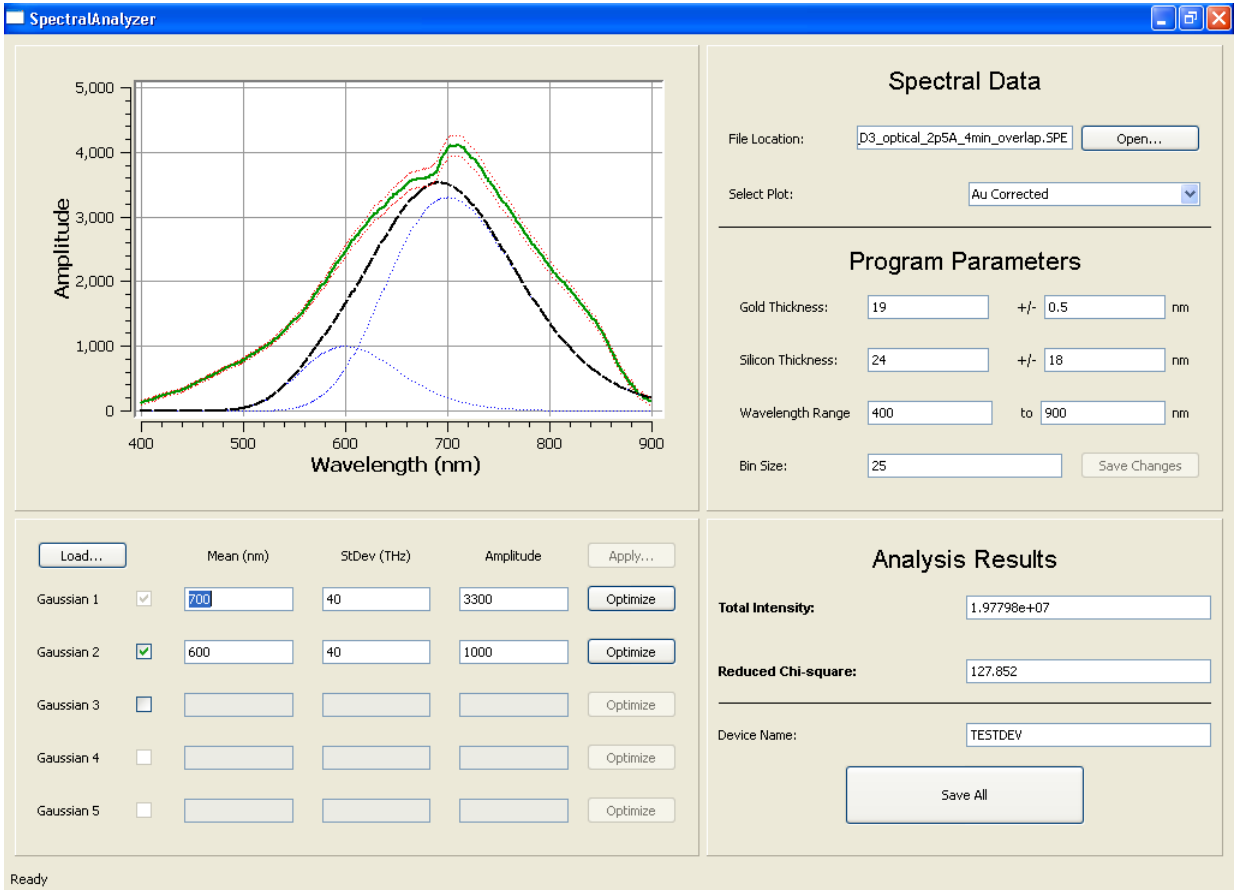

Figure B.5: The SpectralAnalyzer main window. The data to be plotted and a few minor parameters are input to the upper-right panel. The plot itself is shown on the upper-left. Below the plotting panel is the Gaussian fit manager, from which the user defines Gaussian functions to be plotted alongside the spectral data. The panel on the bottom-right displays the reduced chi-square value for the fit and allows the user to save the results to disk.